TECHNISCHE
UNIVERSITÄT
DRESDEN

Dyson-Schwinger equation for the quark propagator at finite temperatures

Diplomarbeit
zur Erlangung des wissenschaftlichen Grades
Diplom-Physiker

vorgelegt von

Marco Viebach
geboren am 10.10.1985 in Potsdam

Institut für Theoretische Physik
Fachrichtung Physik
Fakultät Mathematik und Naturwissenschaften
der Technischen Universität Dresden
2013

Eingereicht am 25.04.2013

1. Gutachter: Prof. Dr. Burkhard Kämpfer
2. Gutachter: Prof. Dr. Dominik Stöckinger

Kurzdarstellung

Im Zusammenhang mit der kombinierten Untersuchung durch die Dyson-Schwinger-Gleichungen und die Bethe-Salpeter-Gleichung bietet diese Arbeit eine systematische Untersuchung der Lösung der Quark-Dyson-Schwinger-Gleichung bei endlichen Temperaturen. Die Gleichung wird mittels direkter Iteration im euklidischen Impulsraum gelöst.

Die chirale Symmetrie-Restauration wird für verschwindende Stromquarkmasse anhand des chiralen Kondensates untersucht. Für leichte Stromquarkmassen dient das subtrahierte Kondensat, um die Restaurierung der näherungsweisen chiralen Symmetrie zu charakterisieren. Für die Untersuchung im Bezug auf Deconfinement wird das Duale Kondensat betrachtet. Die Dispersionsrelation von Quarks wird aus dem berechneten Quark-Propagator gewonnen, wobei ein Zwei-Pol-Ansatz der Transformation in den Minkowski-Raum dient. Im Hinblick darauf, den Quark-Propagator als Eingangsgröße für die Bethe-Salpeter-Gleichung zu verwenden, wird die Polstruktur des Quark-Propagators für komplexe Impulse dargestellt. Die Untersuchung beinhalted die Abhängigkeit von der Stromquarkmasse bei verschwindender Temperatur und die Abhängigkeit von der Temperatur bei verschwindender Stromquarkmasse.

Abstract

Within the context of the combined Dyson-Schwinger-equations and Bethe-Salpeter-equation studies, this thesis presents a systematic investigation of solutions of the quark Dyson-Schwinger equation at finite temperatures. The equation is solved by direct iteration in Euclidean momentum space.

The chiral symmetry restoration is investigated by the chiral condensate for the limit of zero current-quark mass. For light current-quark masses, the subtracted condensate serves for characterizing the restoration of the approximate chiral symmetry. In order to investigate deconfinement, the dual condensate is considered. Having the quark propagator at disposal the dispersion relation is extracted using a two-pole trial function for the spectral density to transform into Minkowski space. In view of using the quark propagator as input for the Bethe-Salpeter equation, the pole structure of the quark propagator is presented for complex momenta. The investigation covers the dependency on the current quark mass at zero temperature and the dependency on the temperature at zero current-quark mass.

Contents

List of Figures

List of Tables

1 Introduction

Quantum chromodynamics (QCD) is the theory of quarks and gluons. It serves to describe the strong interaction within the Standard model of particles and their interactions. Quarks form bound states which are referred to as hadrons. Gluons mediate the interaction between quarks. The specific charges of QCD, the so-called color charges, are carried by both the quarks and the gluons. As a characteristic feature QCD exhibits a negative β-function. This corresponds to a running coupling that is low at large momenta and large at low momenta. Related phenomena are known as asymptotic freedom and confinement of color. In the low momentum regime, a further crucial feature is dynamical chiral symmetry breaking (DCSB). This is an important mechanism for explaining the hadronic mass spectrum. A comparison of the hadronic masses and the current-quark masses reveals the importance of DCSB.

For this reason, the low momentum regime is the region of interest. Because of the large coupling there, this sector cannot be treated by perturbation theory. However, a number of approaches for investigating this non-perturbative regime is available. Those methods are e.g. lattice QCD, QCD sum rules, AdS/CFT correspondence, chiral perturbation theory as well as the Dyson-Schwinger and Bethe-Salpeter equations.

Coupling such approaches to thermodynamic parameters as the temperature and the chemical potential provides access to the QCD phase diagram. Prominent phases are the hadronic phase with quarks and gluons occurring as bound states and the quark gluon plasma (QGP) with unbound quarks and gluons. The former exists at low temperature and chemical potential. Therefore, it is the phase naturally appearing on earth. The regions of phase transitions and the prediction of new phases are matter of current research. Experimentally, heavy ion collisions (HICs) allow to enter regions of the phase diagram other than the hadronic phase. Those HICs are available at the Relativistic heavy ion collider (RHIC) at BNL, USA and the Large Hadron Collider (LHC) at CERN, Switzerland/France and will be available at the Facility for Antiproton and Ion Research (FAIR) at GSI, Germany and the Nuclotron-based Ion Collider fAcility (NICA) at JINR, Russia. Theoretical considerations serve for setting up those facilities and help interpreting the measured data.

This thesis uses the coupled system of Dyson-Schwinger equations (DSEs). In the given

context, it relates the n-point functions of QCD to one another. The Dyson-Schwinger equation for the quark propagator (also referred to as quark DSE) constitutes the central object of this thesis. Its solution, the quark propagator, is an important entity of QCD and offers possibilities to discuss DCSB and confinement. Within the framework of combined Dyson-Schwinger and Bethe-Salpeter equations (DSE/BSE) it represents one module for the investigation of heavy-light mesons, i.e. mesons consisting of one heavy and one light quark or antiquark. The D mesons range among those containing one charm quark or antiquark. They mark one key issue of the large scale collaborations CBM and PANDA at FAIR, which gives the physical motivation for this thesis.

The main focus of this thesis lies on the consideration of non-zero temperatures, which enables to study the QCD phase diagram along the axis of zero chemical potential. This involves the phase transitions of chiral symmetry restoration and deconfinement. The consideration of a non-zero chemical potential to access other regions of the QCD phase diagram than the temperature axis is beyond the scope of this thesis. But the formalism of DSE/BSE qualifies to include this dependency in future work, for example to investigate on the high density states achievable at CBM.

This thesis is organized as follows. Chapter 2 introduces the formalism of the quark DSE and establishes a treatable form of the equation. This covers the derivation of the equation from the QCD generating functional, the introduction of necessary approximations (truncation scheme) and the generalization from zero temperature (synonymously referred to as vacuum) to non-zero temperatures. Natural units $\hbar = c = 1$ and the convention $k_B = 1$ are globally used. For the obligatory background on QCD, field theory at finite temperatures, and QCD phases this thesis refers to [Ynd07, Kap06, Yag05]. Chapter 3 presents solutions of the quark DSE. Since the vacuum case is most compact it serves for discussing the numerical approach and different classes of solutions of the quark DSE. This discussion sets a benchmark for the consideration of a temperature dependence. After extending the numerical approach to non-zero temperatures the respective solutions and the dependence on the temperature are investigated in detail. Chapter 4 discusses characteristic features available through the quark propagator. The investigations cover chiral symmetry restoration by means of the di-quark condensate and an approach to deconfinement via the dual condensate. Furthermore, the dispersion relation of quarks in the chiral symmetric phase is provided via the propagator's spectral representation. The last part of this chapter elaborates on the pole structure of the quark propagator in the complex momentum plane. Finally, Ch. 5 summarizes the results, and gives an outlook on further studies. Algebraic manipulations and certain lengthy details, which are omitted in the main parts, are presented within the appendices.

2 The quark Dyson-Schwinger equation

The Dyson-Schwinger equations (DSEs) constitute a set of equations with interrelations of the Green's functions (n-point functions) of a quantum field theory. Thus, the DSEs form an infinite set of coupled integral equations. This thesis deals with one particular equation from this set within quantum chromodynamics (QCD) - the Dyson-Schwinger equation for the quark propagator. The DSE for the quark propagator directly relates the 2-point function of the quark and the anti-quark field to the 2-point function of two gluon fields and the 3-point function of the gluon, the quark and the anti-quark field. That is, it relates the quark propagator S to the gluon propagator $D^{ab}_{\mu\nu}$ and the quark-gluon vertex Γ^a_ν.

2.1 Derivation and gauge fixing

The derivation of the DSEs of quantum electrodynamics (QED) and QCD for the lowest n-point functions can be found in [Itz05, Rob94, Alk01, Wil07] (for a recent treatment in QCD cf. [Mül11]). To underline the DSEs' character as functional method this section briefly outlines the derivation of the quark DSE. The section at hand describes the main steps to obtain the integral equation for the quark propagator. A detailed discussion including omitted definitions is laid out in Appendix A. Since the calculations of this thesis refer to Euclidean space, a Euclidean-space variant of the derivation is presented.

The quark propagator in position space is given as the mean value of the time-ordered product formed by the quark and anti-quark fields,

$$S(x,y) = \langle 0|Tq(x)\bar{q}(y)|0\rangle. \tag{2.1.1}$$

Within the functional-methods formulation of QCD, it also can be expressed as

$$\langle 0|Tq(x)\bar{q}(y)|0\rangle = \frac{\int \mathcal{D}\mu\, e^{-S_{QCD}} q(x)\bar{q}(y)}{\int \mathcal{D}\mu\, e^{-S_{QCD}}} \tag{2.1.2}$$

with $\mathcal{D}\mu = \{\mathcal{D}q\,\mathcal{D}\bar{q}\,\mathcal{D}\omega\,\mathcal{D}\bar{\omega}\,\mathcal{D}B\}$ as the functional measure with respect to all fields included (quark q, anti-quark $\bar{q}$, ghost ω, anti-ghost $\bar{\omega}$, gluon B) and $S_{QCD} = S_{QCD}[q,\bar{q},\omega,\bar{\omega},B]$ being the action functional of QCD. The notation of the fields corresponds to [Ynd07].

Color and flavour indices as well as Dirac indices are omitted. The introduction of the partition function

$$\mathcal{Z}\left[\bar{\xi},\xi,\bar{\eta},\eta,\lambda\right] := \int \mathcal{D}\mu\, e^{-S_{QCD}+\int \mathrm{d}^4x' \mathcal{L}_{source}} \tag{2.1.3}$$

with

$$\mathcal{L}_{source} := \left\{\bar{\xi}q + \bar{q}\xi + \bar{\eta}^a\omega^a + \bar{\omega}^a\eta^a + \lambda^a_\mu B^a_\mu\right\} \tag{2.1.4}$$

and the sources $\bar{\xi}$ and ξ for the quarks, $\bar{\eta}^a$ and η^a for the ghosts and λ^a_μ for the gluons, respectively, with a being a Gell-Mann index, and μ being a Lorentz index leads to the propagator expressed in terms of functional derivatives acting on the partition function:

$$S(x,y) = \left.\frac{\frac{\delta}{\delta\bar{\xi}}\frac{\delta}{\delta\xi}\mathcal{Z}\left[\bar{\xi},\xi,\bar{\eta},\eta,\lambda\right]}{\mathcal{Z}\left[\bar{\xi},\xi,\bar{\eta},\eta,\lambda\right]}\right|_{\bar{\xi}=0,\,\xi=0,\,\bar{\eta}=0,\,\eta=0,\,\lambda=0}. \tag{2.1.5}$$

Because it generates the n-point functions of the respective QFT (QCD) the partition function is also referred to as generating functional synonymously. The derivation of the quark DSE involves elaborating on the generating functional of QCD $\mathcal{Z}\left[\bar{\xi},\xi,\bar{\eta},\eta,\lambda\right]$. This task consists of three steps: (i) using the fact that the integral of a derivative is a constant, (ii) applying a derivative w.r.t. the source ξ, and (iii) rearranging and identifying the expressions.

The generating functional $\mathcal{Z}[\ldots]$ is independent of the QCD fields. It follows:

$$0 = \int \mathcal{D}\mu\, \frac{\delta}{\delta\bar{q}(x)} e^{-S_{QCD}+\int \mathrm{d}^4x' \mathcal{L}_{source}}. \tag{2.1.6}$$

After carrying out the derivative, casting the expressions into a form using the generating functional yields

$$0 = \left(\frac{\delta S_{QCD}}{\delta\bar{q}(x)}\left[\frac{\delta}{\delta\bar{\xi}},\frac{\delta}{\delta\xi},\frac{\delta}{\delta\bar{\eta}},\frac{\delta}{\delta\eta},\frac{\delta}{\delta\lambda}\right] + \xi(x)\right)\mathcal{Z}\left[\bar{\xi},\xi,\bar{\eta},\eta,\lambda\right] \tag{2.1.7}$$

with $\delta S_{QCD}/\delta\bar{q}(x)[\ldots]$ being the respective functional differential operator acting on the generating functional. Equation (2.1.7) is subject to the differential operator $\delta/\delta\xi$, which acts from the right. Hence,

$$0 = \left(\frac{\delta S_{QCD}}{\delta\bar{q}(x)}\frac{\delta}{\delta\xi(y)}\left[\frac{\delta}{\delta\bar{\xi}},\frac{\delta}{\delta\xi},\frac{\delta}{\delta\bar{\eta}},\frac{\delta}{\delta\eta},\frac{\delta}{\delta\lambda}\right] + \delta^4(x-y)\right)\mathcal{Z}\left[\bar{\xi},\xi,\bar{\eta},\eta,\lambda\right], \tag{2.1.8}$$

where the summand $\delta\mathcal{Z}(\ldots)/\delta\xi$ is omitted, since it does not contribute at the end. The evaluation of this expression can be carried out using the Legendre transformation Γ of the

generating functional's logarithm

$$\Gamma[q,\bar{q},\omega,\bar{\omega},B] := \int \mathrm{d}^4x \left\{\bar{\xi}q + \bar{q}\xi + \bar{\eta}^a\omega^a + \bar{\omega}^a\eta^a + \lambda^a_\mu B^a_\mu\right\} - \log\mathcal{Z} \tag{2.1.9}$$

also referred to as the effective action. Thus, in terms of functional derivatives of the effective action, the one particle irreducible (1PI) vertex Γ^a_ν [Alk01, Ch. 3.1]

$$\Gamma^a_\nu(x,y,z) = \frac{\delta^3\Gamma[q,\bar{q},\omega,\bar{\omega},B]}{\delta B^a_\nu(x)\delta\bar{q}(y)\delta q(z)}. \tag{2.1.10}$$

According to Eq. (2.1.5) the quark propagator and the gluon propagator read

$$S(x-y) = \left.\frac{\delta^2\log\mathcal{Z}\left[\bar{\xi},\xi,\bar{\eta},\eta,\lambda\right]}{\delta\bar{\xi}\delta\xi}\right|_{\bar{\xi}=0,\,\xi=0,\,\bar{\eta}=0,\,\eta=0,\,\lambda=0} \tag{2.1.11}$$

and

$$D^{ab}_{\mu\nu}(x-y) = \left.\frac{\delta^2\log\mathcal{Z}\left[\bar{\xi},\xi,\bar{\eta},\eta,\lambda\right]}{\delta\bar{\lambda}^\mu_a\delta\lambda^\nu_b}\right|_{\bar{\xi}=0,\,\xi=0,\,\bar{\eta}=0,\,\eta=0,\,\lambda=0}. \tag{2.1.12}$$

These identities allow to rewrite Eq. (2.1.8) as

$$\begin{aligned} 0 \;=\; & -(i\not{\partial} + m)S(x-y) + \\ & + i\,g\int \mathrm{d}^4s \int \mathrm{d}^4t \int \mathrm{d}^4u \gamma^\mu t^a D^{ab}_{\mu\nu}(x-s)S(t-y)\Gamma^b_\nu(s,t,u)S(x-u) + \\ & + \delta(x-y). \end{aligned} \tag{2.1.13}$$

A subsequent Fourier transformation, rewriting the vertex, and the multiplication with the inverse propagator yields

$$S^{-1}(p) = (i\not{p} + m) + \int \frac{\mathrm{d}^4l}{(2\pi)^4} g^2 D^{ab}_{\mu\nu}(p-l)t^a\gamma_\mu S(l)\Gamma^b_\nu(l,p). \tag{2.1.14}$$

This is the Dyson-Schwinger equation for the unrenormalized quark propagator in momentum space. A diagrammatic representation of the quark DSE is exhibited in Fig. 2.1.1. The first summand on the right-hand side is the bare quark propagator $S_0(p)$. The second summand on the right-hand side can be interpreted as quark self-energy. In general, Eq. (2.2.5) is a non-linear, inhomogeneous integral equation of the Fredholm type (second kind).

Figure 2.1.1: The Dyson-Schwinger equation for the quark propagator. Double drawn lines represent the full quark propagator S (straight) and the full gluon propagator D (curly). The single straight line is the bare quark propagator S_0. The hatched blob stands for the 1PI quark-gluon vertex Γ^b_ν.

After the application of the renormalization procedure the quark DSE reads [Rob00] [1,2]

$$S^{-1}(p) = Z_2(i\not{p} + \tilde{m}) + Z_1 \int^\Lambda \frac{\mathrm{d}^4 l}{(2\pi)^4} g^2 D_{\mu\nu}(p-l) t^a \gamma_\mu S(l) \Gamma^a_\nu(l,p). \tag{2.1.15}$$

This form already includes the factorization of the color dependency

$$D^{ab}_{\mu\nu}(q) \equiv \delta^{ab} D_{\mu\nu}(q). \tag{2.1.16}$$

Due to the restriction to covariant gauges (cf. [Rob94, p. 491]) the quark-gluon vertex can be decomposed as

$$\Gamma^a_\nu(l,p) \equiv t^a \Gamma_\nu(l,p). \tag{2.1.17}$$

$\Gamma_\nu(l,p)$ is referred to as the proper quark-gluon vertex. Due to this most simple color dependency the Gell-Mann structure's contribution to the self-energy is reduced to a factor C_F which is also referred to as Casimir factor. For $N_C = 3$ colors the contraction of the SU(3) generators yields [3,4]

$$C_F = \delta^{ab} t^a t^b = \sum_{a=1}^{8} \frac{\lambda^a}{2}\frac{\lambda^a}{2} = \frac{1}{2}\sum_{a=1}^{8} [\lambda^a, \lambda^a]_+ = \frac{1}{2}\sum_{a=1}^{8}\left(\frac{4}{3}\delta^{aa} + 2d^{aac}\lambda^c\right) = \frac{4}{3}. \tag{2.1.18}$$

In covariant gauges, the renormalized gluon propagator's most general form is [Rob94]

$$D^{ab}_{\mu\nu}(q) \equiv \delta^{ab}\left[\left(\delta^{\mu\nu} - \frac{q^\mu q^\nu}{q^2}\right)\frac{1}{q^2(1+\Pi(q^2))} + \xi\frac{q^\mu q^\nu}{q^4}\right], \tag{2.1.19}$$

where ξ denotes the gauge fixing parameter and Π is the vacuum polarization of the gluon.

[1] Note that [Alk01] uses the other sign in front of the partial derivative in the quark part of the QCD Lagrangian: $\mathcal{L}_q = \bar{q}(-\not{\partial} + m)q$.
[2] Summation over color and Lorentz indices appearing twice is supposed.
[3] Cf. [Itz05, p. 516].
[4] In general, $C_F = ({N_C}^2 - 1)/(2N_C)$ for N_C colors (cf. [Rob94, p. 489]).

The gauge fixing has two prominent realizations:

$$\begin{aligned} \xi &= 0 : && \text{Landau gauge,} \\ \xi &= 1 : && \text{Feynman gauge,} \end{aligned} \tag{2.1.20}$$

the latter also known as Feynman-t'Hooft gauge [Pes95] or Fermi-Feynman gauge [Ynd07] [5]. This thesis uses the Landau gauge with the reasoning of [Alk01, p. 70]. For this gauge, most approximations are supposed to do reasonably well, even the rainbow approximation.

2.2 Truncation scheme

The Dyson-Schwinger equation for the quark propagator, Eq. (2.2.5), includes the gluon propagator $D^{ab}_{\mu\nu}$ and the quark-gluon vertex Γ^a_ν. These 2-point and 3-point functions satisfy their own Dyson-Schwinger equations. The equations follow in the same manner as the DSE for the quark propagator as described in Sec. 2.1 (cf. [Rob94, Alk01, Wil07]). Analogously, the DSEs for the gluon propagator and the quark-gluon vertex involve higher n-point functions. Finally, the analytical solution of the quark DSE involves the solutions of all DSEs for higher n-point functions. This circumstance prohibits the analytical solution of any DSE. The credibility of an approximation to the quark DSE depends on the content of the truncation scheme, which is applied to the coupled set of equations.

Truncation schemes have been established with different approaches. In relation to obtain the quark propagator, an obvious way is to truncate the infinite tower of Dyson-Schwinger equations [6] right at the bottom, i.e. to make certain ansatzes for the functions $D^{ab}_{\mu\nu}$ and Γ^a_ν [7]. The plenty of appropriate ansatzes is generally restricted by the properties of the theory. With respect to the quark gluon vertex one needs to include the non-Abelian Slavnov-Taylor identity and multiplicative renormalizability of the quark propagator [Alk04]; the gluon propagator may respect the perturbative limit and has to account for the phenomenon of dynamical chiral-symmetry breaking (DCSB) [8].

After specifying the functions, $D^{ab}_{\mu\nu}$ and Γ^a_ν, the remainder is to be attacked by the theory of integral equations. The following considerations base on the findings and choices of Sec. 2.1. That is, the remaining functions to be determined are the proper quark-gluon

[5] Landau gauge means the limit $\xi \longrightarrow 0$, rather than $\xi = 0$. Note the form of the gauge fixing term in the QCD Lagrangian $\mathcal{L}_f = 1/(2\xi)\ (\partial_\mu B^a_\mu)(\partial_\nu B^a_\nu)$.

[6] Because DSEs for n-point functions couple to (n+1)-point functions the set of DSEs is also referred to as the infinite tower of DSEs, e.g. [Rob94].

[7] Recent approaches to the vertex DSE and gluon DSE can be found e.g. in [Hop13] and [Fis13].

[8] In [Rob90], the appearance of a critical coupling strength for DCSB is discussed. References therein elaborate on the phenomenon of DCSB in general.

vertex $\Gamma_\nu(l,p)$ and the transverse part of $D_{\mu\nu}(q)$, namely $1/(q^2(1+\Pi(q^2)))$, since $\xi = 0$.

A well tested and approved example for the quark-gluon-vertex truncation is the so-called rainbow approximation [9], which replaces the proper vertex by the bare vertex, i.e.

$$\Gamma_\nu(p,q) \equiv \gamma_\nu, \tag{2.2.1}$$

where γ_ν denotes Dirac gamma matrices. Other approaches elaborating on the quark-gluon vertex are used in [Fis09b] and [Alk04] considering phenomenological ansatzes, which include the quark dressing functions and thus implement the back coupling to the quark propagator [10].

The truncation of the gluon part can be developed in several manners. According to Eqs. (2.2.5) and (2.1.19), the color independent part of the gluon propagator can be rewritten as

$$g^2 D_{\mu\nu}(q) = g^2 \left(\delta^{\mu\nu} - \frac{q^\mu q^\nu}{q^2}\right) \frac{1}{q^2(1+\Pi(q^2))} = \left(\delta_{\mu\nu} - \frac{q_\mu q_\nu}{q^2}\right) \frac{\Delta(q)}{q^2} \tag{2.2.2}$$

by applying the ansatz of incorporating the running coupling of QCD g^2 into the effective gluon dressing $\Delta(q)$ [11]. The dressing is attached to the bare gluon propagator

$$D_{0\,\mu\nu}^{ab}(q) := \delta^{ab} \left(\delta_{\mu\nu} - \frac{q_\mu q_\nu}{q^2}\right) \frac{1}{q^2} \tag{2.2.3}$$

explicitly noting the color dependency (which is omitted in Eq. (2.2.2)). Thus, the factorization of both the color dependency and the Lorentz structure reduces the problem to the gluon dressing $\Delta(q)$. The function $\Delta(q)/q^2$ is referred to as reduced gluon dressing, from now on. To fill this last vacancy [Bla07], e.g., uses a separable ansatz for the gluon dressing, which provides a great simplification of the calculations at finite temperatures. Another approach to fix the dressing uses lattice data as input for the gluon propagator. In [Fis09b], results for the gluon propagator obtained by lattice QCD simulations serve as basis for fit functions (that of the longitudinal and that of the transverse part of the propagator at finite temperatures). These fit functions directly enter the quark DSE. According to the latter possibility, an a priori ansatz may also be appropriate to define the gluon contribution. A collection of those considerations can be found in [Bla10]. One of them consists of a

[9] For further details see e.g. the introductory section of [Rob00].
[10] Those ansatzes are referred to as "beyond rainbow" (cf. [Alk01, Ch. 7.1.1]).
[11] Cf.[Rob00, p. 12].

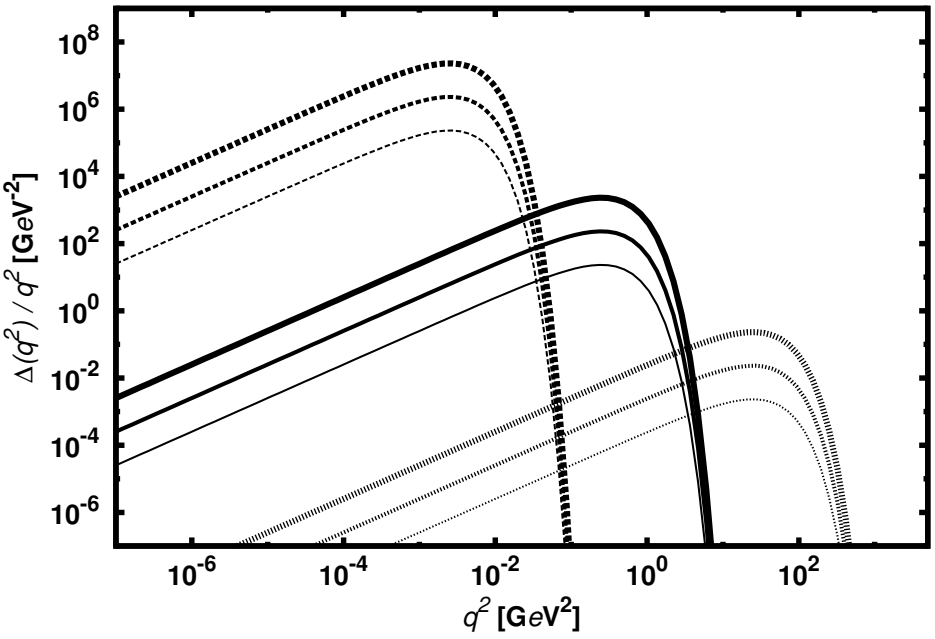

Figure 2.2.1: Reduced gluon dressing $\Delta(q^2)/q^2$ given in Eq. (2.2.4) for several values of the parameters D and ω.
The linewidth denotes the interaction strength D:
thin: $D = 0.1\,\mathrm{GeV}^2$; medium: $D = 1.0\,\mathrm{GeV}^2$; thick: $D = 10.0\,\mathrm{GeV}^2$.
The linetype denotes the interaction width ω:
dashed: $\omega = 0.05\,\mathrm{GeV}$; solid: $\omega = 0.5\,\mathrm{GeV}$; short-dashed: $\omega = 5.0\,\mathrm{GeV}$.

finite-width approximation to the delta function [Alk02]:

$$\frac{\Delta(q^2)}{q^2} \;:=\; 4\pi^2 D \frac{q^2}{\omega^6} e^{-q^2/\omega^2}, \tag{2.2.4}$$

where the parameters D and ω denote the interaction strength and the interaction range, respectively [12]. A comparison w.r.t. the parameters of this dressing is given in Fig. 2.2.1. Its mathematical form adopts that of [Mar99] but omits a logarithmic tail and hence, neglects results from perturbation theory [13]. In [Alk02], this omission was shown to be legal by comparing results of both the interactions for physical observables (cf. Ch. 3). Figure 2.2.2 shows the gluon dressing of Eq. (2.2.4), solid line, in comparison to that of [Mar99], dashed line, as a log-log plot. Around the maximum, the perturbation-corrected dependency almost equals the simpler form of Eq. (2.2.4). However, for smaller as well as for larger momentum values they qualitatively differ from each other. Especially, the

[12] This interpretation can also be found in [Alk02].
[13] Actually, this form originates from [Mar97] as a modulated form derived in [Fra96], which in turn used the parametrization found in [Bro89].

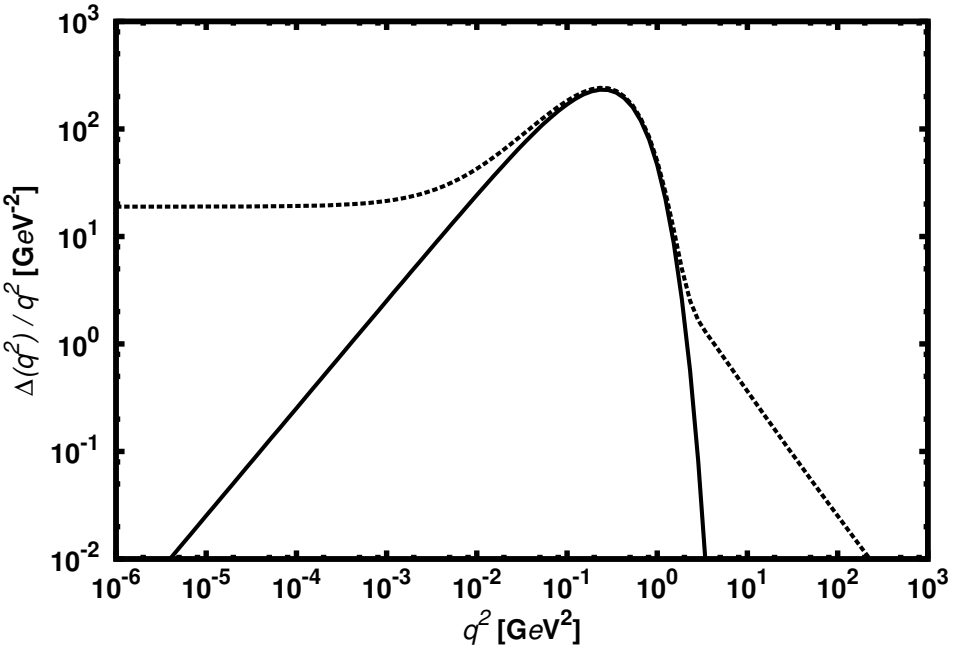

Figure 2.2.2: Reduced gluon dressing $\Delta(q^2)/q^2$ given in Eq. (2.2.4) for $D = 1.0\,\mathrm{GeV}^2$, $\omega = 0.5\,\mathrm{GeV}$ (solid curve). For comparison, the form given in [Mar99] is displayed as dashed curve.

difference for large momenta is to mention because here, it classifies the dressings to be UV convergent or UV divergent. Section 2.3 picks up this question.

The gluon dressing in Eq. (2.2.4) acts as an approximation to $\delta^4(q)$ having a finite width [14]. Thus, the phenomenological fact of a finite, i.e. (compared to the other fundamental forces) small, interaction range enters the model. Note that D and ω are dimensionful parameters ($d_D = 2$, $d_\omega = 1$) [15]. Thus, the scale of a model using this gluon dressing is governed by the order of magnitude of this very parameters (cf. Sec. 2.3).

Another characteristic of a possible gluon dressing Δ is the classification as quenched or unquenched approximation. These terms refer to quark loops which do not enter (quenched) or enter (unquenched) the gluon propagator explicitly [16]. Thus, a phenomenological ansatz like Eq. (2.2.4) belongs to the quenched approximations, since it just models the gluon interaction range and omits further details, cf. Fig. 2.2.3 [17].

After getting acquainted with the procedure of truncating the quark Dyson-Schwinger

[14] Pure $\delta^4(q)$ is used in [Mun83].

[15] $d_D = 2$, $d_\omega = 1$ since $\Delta(q^2)$ has mass dimension $d_\Delta = 0$.

[16] In perturation theory, the quenched approximation refers to neglecting quark loops [Ynd07].

[17] An approach for generalizing the model defined by Fig. 2.2.3 to an unquenched model can be found in [Fis05]. Here, the gluon propagator is considered as sum of the dressed propagator as given by Eq. (2.2.4) and a recursive term including the quark loop contribution. This form corresponds to the truncation of the gluon DSE by rainbow approximation and neglect of the gluon and ghost loops.

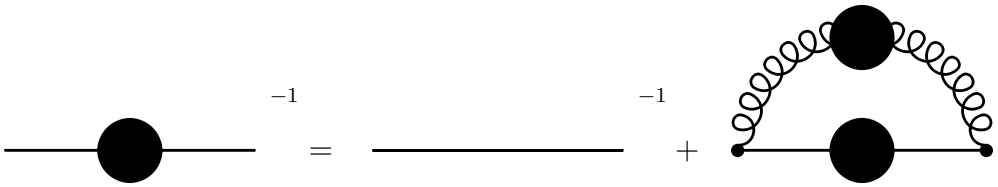

Figure 2.2.3: Truncated quark DSE. The full gluon propagator is approximated by the bare gluon propagator (curly line) equipped with appropriate dressing. The full quark-gluon vertex is replaced by the bare vertex (small filled circle). The straight line represents the bare quark propagator. Large filled blobs both represent respective dressing and symbolize the approximative nature of the truncated DSE (especially in case of the quark propagator).

equation, one model (= truncation scheme) has to be fixed to enable numerical and analytical considerations. The start into the field of DSEs on an elementary level calls for a truncation scheme, which is transparent and contains a clear amount of details. For this purpose the rainbow approximation in combination with the Maris-Tandy like (MT) gluon kernel, Eq. (2.2.4), seems to be an appropriate choice. This truncation scheme is constrained up to the interaction strength D and the interaction range ω. Furthermore, it has no explicit coupling of 2-point and 3-point functions to the quark propagator except that induced by the momentum conservation [18]. On the contrary, the chosen model might also be understood as being constructed by means of a scalar vertex dressing in combination with a scalar gluon dressing. The resulting scalar function (i.e. $\Delta(q^2)/q^2$ in Eq. (2.2.4)) can be interpreted as an effective coupling. Eventually, the quark DSE to be solved reads

$$\begin{aligned} S^{-1}(p) &= Z_2(i\not{p} + \tilde{m}) + \\ &\quad + Z_1 \frac{4}{3} \int^{\Lambda} \frac{\mathrm{d}^4 l}{(2\pi)^4} \left[4\pi^2 D \frac{(p-l)^2}{\omega^6} e^{-(p-l)^2/\omega^2} \left(\delta_{\mu\nu} - \frac{q_\mu q_\nu}{q^2} \right) \right] \gamma_\mu S(l) \gamma_\nu . \end{aligned} \tag{2.2.5}$$

Its diagrammatic form is illustrated in Fig. 2.2.3.

2.3 Renormalization and scales

The truncation scheme defined by the rainbow approximation and the MT gluon kernel has to be characterized as a qualitative model. This fact follows from the functional dependency of the self-energy's integrand. Due to the exponential the integral is UV convergent. Since the effective coupling does not involve an IR divergence, the integral of Eq. (2.2.5) is finite. Hence, the applied truncation scheme supersedes renormalization, which is why the

[18] In Eq. (2.2.5), momentum conservation is given by $q^\mu = p^\mu - l^\mu$, which enters the model when Fourier transforming (cf. [Alk01, Ch. 3.3]).

renormalization constants become

$$Z_1 \equiv 1, \qquad (2.3.1)$$
$$Z_2 \equiv 1$$

and the renormalized mass is a scale invariant parameter

$$\tilde{m} \equiv m. \qquad (2.3.2)$$

Strictly speaking, the model has no intrinsic scale. Only the choice of the scale of one of the model's parameters D, ω and m adheres a scale to the model. In Ch. 3 of this thesis, the choice of particular values for these parameters will be discussed. But to underline the model's property to have no intrinsic scale consider the following: Let the parameters all be of the value $D/\mathrm{GeV}^2 = \omega/\mathrm{GeV} = m/\mathrm{GeV} = 1$. According to this the momentum scale would be fixed to the GeV scale, i.e. the solution to the quark DSE in momentum space would show its characteristic behaviour with GeV values at the abscissa.

The definition of the scale gives a physical meaning to the model. To fix the scale, on the one hand, the interaction range ω might be subject to this procedure. Deep inelastic scattering shows excitations of subnucleon degrees of freedom at the 1 GeV scale [Blo69]. Therefore, ω might be given in terms of GeV. On the other hand, also the mass parameter m may serve for the fixing by physical reasons. In [Ber12], estimates for the masses of the first two quark generations are given by

$$m_u = 2.3^{+0.7}_{-0.5}\ \mathrm{M}e\mathrm{V}, \quad m_d = 4.8^{+0.7}_{-0.3}\ \mathrm{M}e\mathrm{V}, \quad m_s = 95^{+5}_{-5}\ \mathrm{M}e\mathrm{V}, \quad m_c = 1.27^{+0.07}_{-0.09}\ \mathrm{G}e\mathrm{V}.$$

Using these values for the parameter m fixes the scale almost in the same region supporting the truncation scheme of choice. Finally, also the interaction strength D might indirectly fix the scale by the same reasons as the interaction range ω did.

After elaborating on the truncation scheme, the next two sections prepare the equation to be solved. Zero temperature and finite temperatures have to be treated separately, since non-zero temperatures means to couple the physical system to a heat bath and, consequently, to break the O(4)-symmetry of the 4-momentum coordinate.

2.4 Vacuum

In this section, the vacuum quark DSE is prepared for solving. This procedure involves the decomposition of the quark propagator and the subsequent decoupling of the integral

equation for the quark propagator to a set of integral equations for the components of the quark propagator. Subsequently, the integrals will be transformed applying symmetry considerations.

With the findings of the last section in mind, the quark DSE (2.2.5) now reads

$$S^{-1}(p) = (i\not{p} + m) + \frac{4}{3}\int \frac{\mathrm{d}^4 l}{(2\pi)^4} \Delta_D\left((p-l)^2\right)\left(\delta_{\mu\nu} - \frac{q_\mu q_\nu}{q^2}\right)\gamma_\mu S(l)\gamma_\nu \tag{2.4.1}$$

with the reduced dressing

$$\Delta_D\left((p-l)^2\right) := \frac{\Delta\left((p-l)^2\right)}{(p-l)^2} = 4\pi^2 D \frac{(p-l)^2}{\omega^6} e^{-\frac{(p-l)^2}{\omega^2}} \tag{2.4.2}$$

and $q_\mu = p_\mu - l_\nu$. Like the quark propagator $S(p)$ the inverse quark propagator $S^{-1}(p)$ is a matrix object. Inevitably, it is a linear combination of products of γ matrices and the identity matrix. The full quark propagator as well as its inverse are invariant under O(4) transformations of Euclidean space [19]. Following [Rob00] this leads to a decomposition of the inverse quark propagator into two parts

$$S^{-1}(p) \;=\; i\not{p}A(p^2) + \mathbb{I}_4 B(p^2) \tag{2.4.3}$$

The functions $A(p^2)$ and $B(p^2)$ are referred to as quark dressing functions. The imaginary unit is attached to the function A for convenience [20]. The identity matrix $\mathbb{I}_4$ is suppressed from now on. A non-trivial dressing ($A \not\equiv 1$,$B \not\equiv m$) expresses the response of the gluon field to the quark field. By comparison with the inverse free propagator

$$S_0^{-1}(p) = i\not{p} + m \tag{2.4.4}$$

the quotient $B(p^2)/A(p^2)$ can be interpreted as quark mass function $M(p^2)$ (cf. [Rob00]),

$$S^{-1}(p) \;=\; A(p^2)\left(i\not{p} + \frac{B(p^2)}{A(p^2)}\right) =: A(p^2)\left(i\not{p} + M(p^2)\right). \tag{2.4.5}$$

The function $M(p^2)$ invokes the term "dynamical chiral symmetry breaking" (DCSB). Elaborating on the QCD Lagrangian, for zero quark mass m, the system is chirally symmetric. In general, the quark DSE gives $M \not\equiv 0$, i.e. the quark DSE implies chiral symmetry breaking. Because M is momentum dependent the magnitude of breaking is a dynamical phenomenon. For an introduction to chiral symmetry and its breaking this

[19] Appendix B provides details of the Euclidean space formalism.

[20] Actually, the coefficient functions, $A(p^2)$ and $B(p^2)$ map to the complex plane, but by the decomposition of Eq. (2.4.3) and considering real momentum squares their range is within the real numbers.

thesis refers to [Rob94, Hil12].

After decomposing the inverse quark propagator, Eqs. (2.4.1) and (2.4.2) provide integral equations for the dressing functions (see Appendix C.1):

$$\begin{aligned} A(p^2) &= 1 + \frac{4}{3}\int \frac{\mathrm{d}^4 l}{(2\pi)^4} \frac{\Delta_D\left((p-l)^2\right)}{l^2 A^2(l^2) + B^2(l^2)} \left(\frac{pl}{p^2} + \frac{2ql}{q^2}\left(1 - \frac{pl}{p^2}\right)\right) A(l^2), \\ B(p^2) &= m + 4\int \frac{\mathrm{d}^4 l}{(2\pi)^4} \frac{\Delta_D\left((p-l)^2\right)}{l^2 A^2(l^2) + B^2(l^2)} B(l^2). \end{aligned} \tag{2.4.6}$$

The 4-dimensional momentum integral consists of only two proper integrals, i.e. one over the absolute value of l_μ denoted by λ and one over the angle $\theta(p_\mu, l_\mu) = \arccos(p_\mu l_\mu / \sqrt{p^2 l^2})$ (using hyperspherical coordinates with $e_4 = (0,0,0,1) \equiv p_\mu/\sqrt{p^2}$). Defining $t := \cos\theta(p_\mu, l_\mu)$ the integral measure of Eq. (2.4.6) can be written as [21]

$$\int \frac{\mathrm{d}^4 l}{(2\pi)^4} = \frac{1}{4\pi^3}\int_0^\infty \mathrm{d}\lambda \lambda^3 \int_{-1}^1 \mathrm{d}t \sqrt{1-t^2} \tag{2.4.7}$$

with $\lambda := \sqrt{l^2}$. Defining $\kappa := \sqrt{p^2}$ and omitting the squares Eq. (2.4.6) becomes

$$\begin{aligned} A(\kappa) &= 1 + \frac{1}{3}\int \frac{\mathrm{d}\lambda\lambda^3}{\pi^3} \int \mathrm{d}t \sqrt{1-t^2}\, \frac{\Delta_D(\kappa,\lambda,t) A(\lambda)}{\lambda^2 A^2(\lambda) + B^2(\lambda)} \frac{\lambda}{\kappa} \left(t + 2\frac{(\kappa - \lambda t)(\kappa t - \lambda)}{\kappa^2 + \lambda^2 - 2\kappa\lambda t}\right), \\ B(\kappa) &= m + \int \frac{\mathrm{d}\lambda\lambda^3}{\pi^3} \int \mathrm{d}t \sqrt{1-t^2}\, \frac{\Delta_D(\kappa,\lambda,t) B(\lambda)}{\lambda^2 A^2(\lambda) + B^2(\lambda)}. \end{aligned} \tag{2.4.8}$$

This is the set of equations to be solved to obtain the quark propagator in vacuum. Despite renormalization, Eq. (2.4.8) represents the general form of the respective equations using a model consisting of the rainbow approximation and effective quark-gluon interaction in Landau gauge.

2.5 Finite temperatures

After dealing with the quark DSE in vacuum, the system will be coupled to a heat bath. This step changes the structure of the equations above. Due to the head-bath vector,

[21] Explictly,

$$\begin{aligned} \int \frac{\mathrm{d}^4 l}{(2\pi)^4} &= \frac{1}{(2\pi)^4}\int_0^\infty \mathrm{d}\lambda\lambda^3 \int \mathrm{d}\Omega_4 \\ &= \frac{1}{(2\pi)^4}\int_0^\infty \mathrm{d}\lambda\lambda^3 \int_0^\pi \mathrm{d}\theta \sin^{(4-2)}\theta \int_0^\pi \mathrm{d}\chi \sin^{(4-3)}\chi \int_0^{2\pi} \mathrm{d}\phi \\ &= \frac{1}{4\pi^3}\int_0^\infty \mathrm{d}\lambda\lambda^3 \int_{-1}^1 \mathrm{d}t\sqrt{1-t^2}. \end{aligned}$$

the O(4) symmetry of the quark momentum is destroyed. According to the vacuum case, the resulting equation will be decomposed into integral equations for the quark dressing functions. Differently here, the breaking of the O(4) symmetry of the momentum calls for a more complex structure of the inverse propagator, i.e. not two but three dressing functions.

For discussing temperature effects this thesis uses the canonical ensemble of statistical mechanics

$$\mathcal{Z}_{stat,\beta} := \mathrm{tr}\left(e^{-\beta H}\right) \tag{2.5.1}$$

with H denoting the ensemble Hamiltonian. The temperature T enters by $\beta := 1/T$. This ensemble rewritten for QCD reads

$$\mathcal{Z}_{QCD,\beta}[\bar{\xi},\xi,\bar{\eta},\eta,\lambda] := \int \mathcal{D}\mu_{\{\mathrm{per}\}}\, e^{\int_0^\beta \mathrm{d}\tau \int \mathrm{d}^3x\{-\mathcal{L}_{QCD}+\mathcal{L}_{source}\}}. \tag{2.5.2}$$

The integral measure $\mathcal{D}\mu_{\{\mathrm{per}\}}$ corresponds to that of Eq. (2.1.2) but with the index {per} denoting the restriction to periodic boundary conditions as follows below. Within this approach, the time coordinate of Minkowski space is changed to purely imaginary values, $t \to \tau := i\,t$, $\tau \in \mathbb{R}$ [22]. By restricting the time integration involved in the generating functional of the field theory (cf. Eq. (2.1.3) [23]) to $\tau \in [0,\beta]$ and introducing periodic boundary conditions w.r.t. τ the partition function meets the canonical partition function, which contains all information about the respective canonical ensemble. The need for boundary conditions arises from the trace operation tr(...) in Eq. (2.5.1). The (anti-) periodic boundary conditions read

$$\psi(0,\boldsymbol{x}) = -\psi(\tau,\boldsymbol{x}), \quad \text{for } \psi \text{ a fermion field,} \tag{2.5.3}$$

$$\phi(0,\boldsymbol{x}) = +\phi(\tau,\boldsymbol{x}), \quad \text{for } \phi \text{ a boson field.} \tag{2.5.4}$$

The vacuum expectation values obtained by virtue of the QCD partition function are transformed to ensemble expectation values obtained from the canonical partition function. Moreover, the vacuum DSE for the quark propagator, Eq. (2.1.13), is transformed to its ensemble counterpart, i.e. the quark DSE in position space at finite temperatures. The Fourier transformation of this DSE calls for another feature of the finite temperature formalism, namely the Matsubara formalism.

Due to the (anti-) periodic boundary conditions of the fields the Fourier transform w.r.t.

[22] This feature is globally adopted in this thesis because all considerations use Euclidean space, i.e. the previous sections already contain imaginary-time formalism. Therefore, the migration from vacuum expectation values to the thermodynamic ones needs less effort.

[23] Note that Eq. (2.1.3) displays the Euclidean space partition function, i.e. it adheres imaginary-time formalism.

the time coordinate reduces to a Fourier series. Hence, the time-like momentum coordinate takes only discrete values, which are referred to as Matsubara frequencies. Because of the antiperiodic boundary conditions of fermion fields, fermion-Matsubara frequencies have a phase shift compared to the boson ones. The Matsubara frequencies result in

$$\begin{aligned} \Omega_n(T) &= \pi T(2n) \qquad \text{for boson fields,} \\ \omega_n(T) &= \pi T(2n+1) \quad \text{for fermion fields} \end{aligned} \tag{2.5.5}$$

with n integer valued. Since the boson Matsubara frequencies will be also used as difference of two fermion Matsubara frequencies, it is convenient to introduce a notation which enables the identification of the two fermion Matsubara frequencies:

$$\Omega_{nm}(T) := \omega_n(T) - \omega_m(T) = \pi T(2n - 2m). \tag{2.5.6}$$

Which notation is used, Eq. (2.5.5) or Eq. (2.5.6), depends on the context.

According to this discrete momentum coordinate, Eq. (2.5.5), ordinary integration over the 4-dimensional Euclidean space is altered to the combination of integrating over 3-dimensional Euclidean space of the spatial coordinates and summing over the Matsubara indices of the time-like coordinate

$$\int \frac{\mathrm{d}^4 p}{(2\pi)^4} \quad \to \quad T \sum_{n=-\infty}^{\infty} \int \frac{\mathrm{d}^3 p}{(2\pi)^3} \tag{2.5.7}$$

with $\mathrm{d}^3 p/(2\pi)^3$ being the spatial momentum-space measure. The square of the momentum reads

$$\begin{aligned} q^2 &= \boldsymbol{q}^2 + {\Omega_n}^2 \quad \text{with } q = (\boldsymbol{q}, \Omega_n), \quad \text{for boson fields,} \\ p^2 &= \boldsymbol{p}^2 + {\omega_n}^2 \quad \text{with } p = (\boldsymbol{p}, \omega_n), \quad \text{for fermion fields.} \end{aligned} \tag{2.5.8}$$

A detailed discussion on the fundamentals of thermo-field theory can be found e.g. in [Kap06, Bel00], which the elaboration of the first part of this subsection bases on.

With the prescriptions of the finite temperature formalism, Eqs. (2.5.5 - 2.5.8), the DSE for the quark propagator in vacuum, Eq. (2.4.1), can be reformulated. Since the truncation scheme of this thesis involves a convergent quark-gluon coupling, a renormalization procedure is not necessary also for the calculation of the quark propagator at finite temperatures [24].

Thus, in the context of this thesis, applying Eqs. (2.5.5 - 2.5.8) to Eq. (2.4.1) yields the

[24] If needed, the renormalization for the finite temperatures system would resemble that of the vacuum system, since the migration from the vacuum to the medium does not introduce qualitatively new divergences [Rob00, Ch. 3.1].

quark DSE in momentum space at finite temperatures

$$S^{-1}(\boldsymbol{p},\omega_n) = (i(\boldsymbol{\gamma p} + \gamma_4\omega_n) + m) + \frac{4}{3}T\sum_{m=-\infty}^{\infty}\int\frac{\mathrm{d}^3 l}{(2\pi)^3} g^2\, D(q)_{\mu\nu}\gamma_\mu S(\boldsymbol{l},\omega_m)\gamma_\nu \quad (2.5.9)$$

with $\boldsymbol{\gamma p} := \sum_{i=1}^{3}\gamma_i p_i$ and $g^2\, D_{\mu\nu}(q)$ as the quark-gluon coupling. The latter one corresponds to the coupling given in Eq. (2.4.2), but does not equal it. Here, after implementing the temperature dependence of the canonical ensemble in the theory and likewise to the DSEs, at least one consequence of this extension [25] needs to be discussed.

Considering the theory by means of the canonical ensemble especially means to have the system coupled to a head bath. Hence, the system is described w.r.t. the reference frame of the heat bath, i.e. the theory contains a preferred direction. This direction is the direction of the 4-velocity of the heat bath u_μ, which is without loss of generality $u_\mu = (0,0,0,1)$ (i.e. the medium is at rest in the respective reference frame). Consequently, the O(4) symmetry of the vacuum system is destroyed at finite temperatures. The symmetry of the coordinates perpendicular to u_μ remains, i.e. the O(3) symmetry of the spatial coordinates.

Since the rainbow approximation uses the bare quark-gluon vertex (which contains no momentum dependence), only the gluon propagator and the quark propagator have to be adapted to the new symmetry. The gluon propagator in Landau gauge is decomposed into a part transversal to u_μ and into a part longitudinal to u_μ, respectively (cf. [Ben96])

$$g^2 D_{\mu\nu}(\boldsymbol{q},\Omega_n) = P^L{}_{\mu\nu}(\boldsymbol{q},\Omega_n)\Delta_F(\boldsymbol{q},\Omega_n) + P^T{}_{\mu\nu}(\boldsymbol{q},\Omega_n)\Delta_G(\boldsymbol{q},\Omega_n)\ ^{26} \quad (2.5.10)$$

with

$$\begin{aligned} P^T{}_{\mu\nu}(\boldsymbol{q},\Omega_n) &:= \begin{cases} 0; & \mu = 4 \quad \text{and/or} \quad \nu = 4, \\ \delta_{ij} - \frac{q_i q_j}{\boldsymbol{q}^2}; & i,j = \mu,\nu = 1,2,3 \quad , \end{cases} \\ P^L{}_{\mu\nu}(\boldsymbol{q},\Omega_n) &:= \delta_{\mu\nu} - \frac{q_\mu q_\nu}{q^2} - P^T{}_{\mu\nu}(\boldsymbol{q},\Omega_n). \end{aligned} \quad (2.5.11)$$

The scalar functions Δ_F and Δ_G denote the longitudinal and the transversal gluon dressing function, respectively [27,28]. Furthermore, concerning the structure of the quark propagator the considerations of the last chapter have to be repeated here. The objects under consideration are $\mathbb{I}_4$, p_μ and γ_μ, as well as P_μ. Following [Rob00] these lead to three

[25] The consideration of finite temperatures as described in this section is an extension of the vacuum case, indeed, because the temperature dependent solution of the quark DSE includes the vacuum solution as the limit $\lim_{T\to 0}$ (cf. Sec. 3.3).

[26] Note that in Eq. (2.5.9), the notation $g^2 D_{\mu\nu} = \Delta_D(q)(\delta_{\mu\nu} - q_\mu q_\nu/q^2)$ corresponding to Eq. (2.4.1) is invalid because of destroyed O(4) symmetry.

[27] These are also referred to as Δ^T magnetic and Δ^L electric dressing functions.

[28] With respect to Sec. 2.2 note that Δ_F and Δ_G correspond to the reduced dressing $\Delta(q)/q^2$.

structures entering the inverse propagator [29]

$$S^{-1}(\boldsymbol{p},\omega_n) = i\,\boldsymbol{\gamma p} A(\boldsymbol{p}^2,\omega_n) + i\,\gamma_4\omega_n C(\boldsymbol{p}^2,\omega_n) + B(\boldsymbol{p}^2,\omega_n). \tag{2.5.12}$$

The scalar functions A, C and B denote the quark dressing at finite temperatures.

Plugging Eqs. (2.5.10 - 2.5.12) into Eq. (2.5.9) and reducing the Dirac algebra yields three coupled equations for the quark dressing functions. This procedure is presented in App. C.2. The resulting set of integral equations reads

$$\begin{aligned}
A(\boldsymbol{p}^2,\omega_n) &= 1 + \frac{4}{3}T\sum_{m=-\infty}^{\infty}\int\frac{\mathrm{d}^3 l}{(2\pi)^3} \\
&\quad\times\Bigg\{\left[\frac{\boldsymbol{pl}}{\boldsymbol{p}^2}\sigma_A + \frac{\Omega_{nm}}{q^2}2\left(1-\frac{\boldsymbol{pl}}{\boldsymbol{p}^2}\right)\omega_m\sigma_C - \frac{\Omega_{nm}^2}{q^2}2\,\frac{(\boldsymbol{ql})}{\boldsymbol{q}^2}\left(1-\frac{\boldsymbol{pl}}{\boldsymbol{p}^2}\right)\sigma_A\right]\Delta_F(\boldsymbol{q},\Omega_{nm}) \\
&\qquad + 2\frac{(\boldsymbol{ql})}{\boldsymbol{q}^2}\left(1-\frac{\boldsymbol{pl}}{\boldsymbol{p}^2}\right)\sigma_A\Delta_G(\boldsymbol{q},\Omega_{nm})\Bigg\}, \\
C(\boldsymbol{p}^2,\omega_n) &= 1 + \frac{1}{\omega_n}\frac{4}{3}T\sum_{m=-\infty}^{\infty}\int\frac{\mathrm{d}^3 l}{(2\pi)^3} \\
&\quad\times\Bigg\{\left[-\left(1-2\frac{\Omega_{nm}^2}{q^2}\right)\omega_m\sigma_C + \frac{\Omega_{nm}}{q^2}2\,(\boldsymbol{ql})\sigma_A\right]\Delta_F(\boldsymbol{q},\Omega_{nm}) \\
&\qquad + 2\omega_m\sigma_C\Delta_G(\boldsymbol{q},\Omega_{nm})\Bigg\}, \\
B(\boldsymbol{p}^2,\omega_n) &= m + \frac{4}{3}T\sum_{m=-\infty}^{\infty}\int\frac{\mathrm{d}^3 l}{(2\pi)^3}\,\sigma_B\{2\,\Delta_G(\boldsymbol{q},\Omega_{nm}) + \Delta_F(\boldsymbol{q},\Omega_{nm})\}
\end{aligned} \tag{2.5.13}$$

with $\boldsymbol{q} = \boldsymbol{p} - \boldsymbol{l}$, $\Omega_{nm} = \omega_n - \omega_m$, and

$$\sigma_F = \sigma_F(\boldsymbol{l}^2,\omega_m) := \frac{F(\boldsymbol{l}^2,\omega_m)}{\boldsymbol{p}^2A^2(\boldsymbol{l}^2,\omega_m) + {\omega_m}^2C^2(\boldsymbol{l}^2,\omega_m) + B^2(\boldsymbol{l}^2,\omega_m)}. \tag{2.5.14}$$

The index F is dummy for A, B, and C, respectively. Using spherical coordinates with $t := \cos\theta(\boldsymbol{p},\boldsymbol{l}) = \boldsymbol{pl}/\sqrt{\boldsymbol{p}^2\boldsymbol{l}^2}$ and $\boldsymbol{e}_3 = (0,0,1) \equiv \boldsymbol{p}/\sqrt{\boldsymbol{p}^2}$ the integral measure in Eq. (2.5.13) is reduced to

$$\int\frac{\mathrm{d}^3 l}{(2\pi)^3} = \frac{1}{(2\pi)^2}\int_0^\infty \mathrm{d}l\,l^2\int_{-1}^1 \mathrm{d}t. \tag{2.5.15}$$

This leads Eq. (2.5.13) to the system of equations to be solved for the quark propagator

[29] The decomposition in Eq. (2.5.12) neglects one summand corresponding to $\sigma_{\mu\nu} = i/2[\gamma_\mu,\gamma_\nu]$ which has minor influence.

at finite temperatures. Like in Sec. 2.4 the resulting equations [30] constitute the set of equations for the quark dressing using the rainbow approximation and the gluon propagator Landau gauge.

Although the longitudinal dressing Δ_L and the transverse dressing Δ_T have to be considered as to exhibit different momentum and temperature dependencies in general [31], this thesis considers both the dressing functions to be equal and temperature independent [32]. This enables to concentrate on the changes of the quark propagators' structure and omits introducing additional parameters. According to Sec. 2.2 the gluon dressing at finite temperatures is considered as

$$\Delta_G(\boldsymbol{q},\Omega_{nm}) \equiv \Delta_F(\boldsymbol{q},\Omega_{nm}) = \Delta_H\left(\boldsymbol{q}^2+\Omega_{nm}^2\right) = 4\pi^2 D\frac{\boldsymbol{q}^2+\Omega_{nm}^2}{\omega^6}e^{-\frac{\boldsymbol{q}^2+\Omega_{nm}^2}{\omega^2}}. \tag{2.5.16}$$

Implementing the gluon-dressing functions to be equal, Eq. (2.5.13) is reduced to

$$\begin{aligned}
A(\boldsymbol{p}^2,\omega_n) &= 1+\frac{4}{3}T\sum_{m=-\infty}^{\infty}\int\frac{\mathrm{d}^3l}{(2\pi)^3} \\
&\quad\times\left[\frac{\boldsymbol{pl}}{\boldsymbol{p}^2}\sigma_A+\frac{\Omega_{nm}}{q^2}2\left(1-\frac{\boldsymbol{pl}}{\boldsymbol{p}^2}\right)\omega_m\sigma_C+2\,\frac{(\boldsymbol{ql})}{q^2}\left(1-\frac{\boldsymbol{pl}}{\boldsymbol{p}^2}\right)\sigma_A\right]\Delta_H(\boldsymbol{q},\Omega_{nm}), \\
C(\boldsymbol{p}^2,\omega_n) &= 1+\frac{1}{\omega_n}\frac{4}{3}T\sum_{m=-\infty}^{\infty}\int\frac{\mathrm{d}^3l}{(2\pi)^3} \\
&\quad\times\left[\left(1+2\frac{\Omega_{nm}^2}{q^2}\right)\omega_m\sigma_C+\frac{\Omega_{nm}}{q^2}2\,(\boldsymbol{ql})\sigma_A\right]\Delta_H(\boldsymbol{q},\Omega_{nm}), \\
B(\boldsymbol{p}^2,\omega_n) &= m+\frac{4}{3}T\sum_{m=-\infty}^{\infty}\int\frac{\mathrm{d}^3l}{(2\pi)^3}\,3\,\sigma_B\Delta_H(\boldsymbol{q},\Omega_{nm}).
\end{aligned} \tag{2.5.17}$$

This is the final set of equations which defines the quark propagator at finite temperatures within the context of this thesis. Using Eq. (2.5.15), the notation $\lambda := \sqrt{\boldsymbol{l}^2}$, and $\kappa := \sqrt{\boldsymbol{p}^2}$ and omitting the squares at the functions' arguments it reads

$$\begin{aligned}
A(\kappa,\omega_n) &= 1+\frac{T}{3\pi^2}\sum_{m=-\infty}^{\infty}\int_0^\infty\mathrm{d}\lambda\,\lambda^2\int_{-1}^1\mathrm{d}t \\
&\quad\times\left[\left(\frac{t\lambda}{\kappa}+\frac{2\left(\kappa\lambda t-\lambda^2\right)\left(1-\frac{t\lambda}{\kappa}\right)}{\kappa^2+\lambda^2-2\kappa\lambda t+\Omega_{nm}^2}\right)\sigma_A(\lambda,\omega_m)\right.
\end{aligned} \tag{2.5.18}$$

[30] The lengthy restatement of Eq. (2.5.13) prescribed in terms of $p=|\boldsymbol{p}|$, $l=|\boldsymbol{l}|$ and t is omitted. In Eq. (2.5.18), the quark DSE at non-zero temperatures with specified gluon dressing is presented in explicit notation.

[31] See, e.g., the discussions in [Bla10] and [Cuc07].

[32] Note that the temperature enters the gluon dressing via the boson Matsubara frequency $\Omega_{nm} = \pi T(2n-2m)$, i.e. the temperature is encapsulated as a part of the gluon momentum.

$$+\frac{\Omega_{nm} 2\left(1-\frac{t\lambda}{\kappa}\right)\omega_m}{\kappa^2+\lambda^2-2\kappa\lambda t+\Omega_{nm}^2}\sigma_C(\lambda,\omega_m)\Bigg]\Delta_H(\kappa,\lambda,t,\Omega_{nm}),$$

$$\begin{aligned}
C(\kappa,\omega_n) &= 1+\frac{1}{\omega_n}\frac{T}{3\pi^2}\sum_{m=-\infty}^{\infty}\int_0^\infty \mathrm{d}\lambda\,\lambda^2\int_{-1}^{1}\mathrm{d}t \\
&\quad\times\Bigg[\frac{\Omega_{nm} 2\left(\kappa\lambda t-\lambda^2\right)}{\kappa^2+\lambda^2-2\kappa\lambda t+\Omega_{nm}^2}\sigma_A(\lambda,\omega_m) \\
&\quad+\left(\omega_m+\frac{2\Omega_{nm}^2\omega_m}{\kappa^2+\lambda^2-2\kappa\lambda t+\Omega_{nm}^2}\right)\sigma_C(\lambda,\omega_m)\Bigg]\Delta_H(\kappa,\lambda,t,\Omega_{nm}), \\
B(\kappa,\omega_n) &= m+\frac{T}{\pi^2}\sum_{m=-\infty}^{\infty}\int_0^\infty \mathrm{d}\lambda\,\lambda^2\int_{-1}^{1}\mathrm{d}t\,\sigma_B(\lambda,\omega_m)\Delta_H(\kappa,\lambda,t,\Omega_{nm})
\end{aligned}$$

with

$$\Delta_H(\kappa,\lambda,t,\Omega_{nm}) = 4\pi^2 D\frac{\kappa^2+\lambda^2-2\kappa\lambda t+\Omega_{nm}^2}{\omega^6}e^{-\frac{\kappa^2+\lambda^2-2\kappa\lambda t+\Omega_{nm}^2}{\omega^2}}. \tag{2.5.19}$$

3 Solutions of the quark DSE

This chapter is devoted to the solutions of the Dyson-Schwinger equation for the quark propagator in rainbow approximation and with the MT gluon kernel. The first part briefly discusses the vacuum solutions [1] to set a benchmark for comparison with solutions at non-zero temperatures. The second part presents these finite temperature solutions and elaborates on their properties. Finally, the chapter ends with a comparison of both regimes and with the discussion of the limit $T \to 0$.

Before treating the integral equations of Eqs. (2.4.8) and (2.5.17), the parameters of the model, namely the interaction strength D and the interaction range ω, can be fixed to inspirit the topic in view of rather technical considerations which open the following part of this chapter. As worked out in Sec. 2.3 the dimensionful parameters have to be chosen on a GeV scale. Further reasoning is aided by [Alk02, Mar99]. Here, combined studies of Dyson-Schwinger equations and the Bethe-Salpeter equation (DSE/BSE) provide numerical data on physical observables in vacuum. With respect to the pseudoscalar sector, the pion and kaon mass as well as their decay constants are calculated. With respect to vector mesons results for the ρ, K* and ϕ meson are presented. This system of observables is used to fit the model parameters ω and D to obtain the observables' experimental values. The specification

$$D = 1.0\,\mathrm{G}e\mathrm{V}^2, \quad \omega = 0.5\,\mathrm{G}e\mathrm{V}$$

is found to best fit the model's output to the experimental data. This is why this chapter first considers this very specification of the parameters. A further discussion on the influence of the parameters to the solutions at finite temperatures can be found in Sec. 4.1.1.

3.1 Vacuum solutions

The problem of this section is to find an appropriate way for solving the coupled set of integral equations for the dressing functions of the inverse propagator in vacuum, Eq. (2.4.8). An analytical solution seems to be rather difficult if not impossible, which is

[1] The first implementation of the quark DSE in vacuum (i.e. Eq. (2.4.8)) bases on the work of Sergey Dorkin, JINR Dubna.

why a numerical treatment is the first choice. After specifying and discussing the numerical procedure corresponding classes of solutions to the vacuum will be presented.

Since the integral equations for the dressing functions constitute a non-linear system, the well-known superposition principle cannot be applied to find the solution set. In general, considering non-linear integral equations statements on completeness of a set of found solutions are difficult to make; the solution set might consist of multiple qualitatively different functions. An approved way to find at least one of the integral equation's solutions is fixed-point iteration. In praxi, one sets a (reasonable) initial guess for the function in question and tries until the respective sequences of images generated by the integral operator converges. Generally, an integral operator has more than one fixed point. The choice of the initial guess determines the fixed point which the sequence converges to.

In this thesis, the method of fixed-point iteration is intensively used, in particular the direct iteration of the equations as described above. This method stands out due to its stability. Another variant of fixed point iteration is used in [Hil12], namely a Newton-Krylov (NK) algorithm in combination with direct iteration. Since the NK method calls for a *good* initial guess, the solution of direct iteration enters it as initial guess for a slightly modified integral equation. Such modifying may concern the equation's parameters.

Now, the direct iteration Eq. (2.4.8) is to be discussed, i.e. the integration starting from an initial function. Integration and iteration of Eq. (2.4.8) require numerical procedures. For this purpose, weighted quadrature rules are commonly used:

$$\int_a^b \mathrm{d}x f(x) = \int_a^b \mathrm{d}x g(x) w(x) = \sum_{i=1}^{n} g(x_i)\alpha_i + R_n(g). \tag{3.1.1}$$

The integrand f is decomposed into an appropriate weight function w and the respective remaining function g to represent the integral as weighted sum of values $g(x_i)$ of the remaining function added by the remainder $R_n(g)$. α_i denotes the i'th weight. The remainder depends not only on the function g but also on the number n of nodes taken into account. The nodes x_i are chosen such that the weighted sum results in the minimal remainder. Thus, $R_n(g)$ does not depend on them. For practical work, the number of nodes is assumed to be large enough to achieve an approximate result by neglecting the $R_n(g)$ [2]. An overview about quadrature rules can be found in [Abr64]. Detailed discussions are given e.g. in [Sto80] and [Gau11].

Equation (2.4.8) contains two integrals. The angular integration calls for the second-kind Gauss-Chebychev quadrature, because the weight function $w^{\mathrm{ch}}(x) = \sqrt{1-x^2}$ appears in

[2] In particular cases which are defined by the weighting function w and the number of nodes n, the remainder $R_n(g)$ vanishes.

the integrand explicitly. Thus,

$$\int_{-1}^{1} \mathrm{d}t\sqrt{1-t^2}g(t) \approx \sum_{j=1}^{n^{\mathrm{ch}}} g(t_j^{\mathrm{ch}})\alpha_j^{\mathrm{ch}} \tag{3.1.2}$$

with t_j^{ch} the second-kind Gauss-Chebychev nodes and α_j^{ch} the corresponding weights (cf. [Abr64, Eq. (25.4.40)]). The momentum integration does not contain any common weight function except for the trivial one, $w^{\mathrm{le}}(x) \equiv 1$. This weight function corresponds to the Gauss-Legendre quadrature. While the bounds of the angular integration in Eq. (2.4.8) equal those of the quadrature rule ($t \in [-1, 1]$), the infinite momentum range ($\lambda \in [0, \infty)$) needs to be mapped to the finite range of the Gauss-Legendre quadrature ($x \in [-1, 1]$). The mapping typically consists of a rational function. The following form is used throughout this thesis:

$$\lambda \in [0, \infty) \quad \longrightarrow \quad \lambda(x) := p_0 \frac{1+x}{1-x}, \quad x \in [-1, 1) \tag{3.1.3}$$

with the mapping parameter p_0, which maintains the mass dimension. Its value is ubiquitously set to $p_0 = 1\,\mathrm{G}e\mathrm{V}$. The integral transform and approximation read

$$\begin{aligned} \int_0^{\infty} \mathrm{d}\lambda g(\lambda) \;&\to\; \int_{-1}^{1} \mathrm{d}x \frac{2p_0}{(1-x)^2} g\left(\lambda(x)\right) \\ &\approx\; \sum_{i=1}^{n^{\mathrm{le}}} g(\lambda(x_i^{\mathrm{le}}))\alpha_i^{\mathrm{le}} \end{aligned} \tag{3.1.4}$$

with x_i^{le} the Gauss-Legendre nodes and α_i^{le} the corresponding weights (cf. [Abr64, Eq. (25.4.29)]) [3,4]. The final form of the approximated DSE in vacuum ready for implementation is shown in App. F.

After defining the integration procedure, the iteration process has to be specified. One iteration step consists of simultaneous integration of both the A and the B part of Eq. (2.4.8). Quantitative statements about the iteration progress call for the definition of a metric in the solution space $\{S\} = \{(A, B)\}$. Variable S denotes all discrete 2-dimensional functions

[3] Eventually, the mapping (3.1.3) causes a factor $(1+x)^5/(1-x)^3$ in the integrand of Eq. (3.1.4), cf. App. F. Hence, the integration via Gauss-Jacobi quadrature seems to be a better way. But according to experience, Gauss-Legendre very often approximates integrals of general integrable functions with high precision [Bro99]. This is why the possible improvements of Gauss-Jacobi quadrature are not considered.

[4] The values of α_i^{le} and x_i^{le} are available through the *gauleg* routine [Pre92], which only needs to be adapted to double precision.

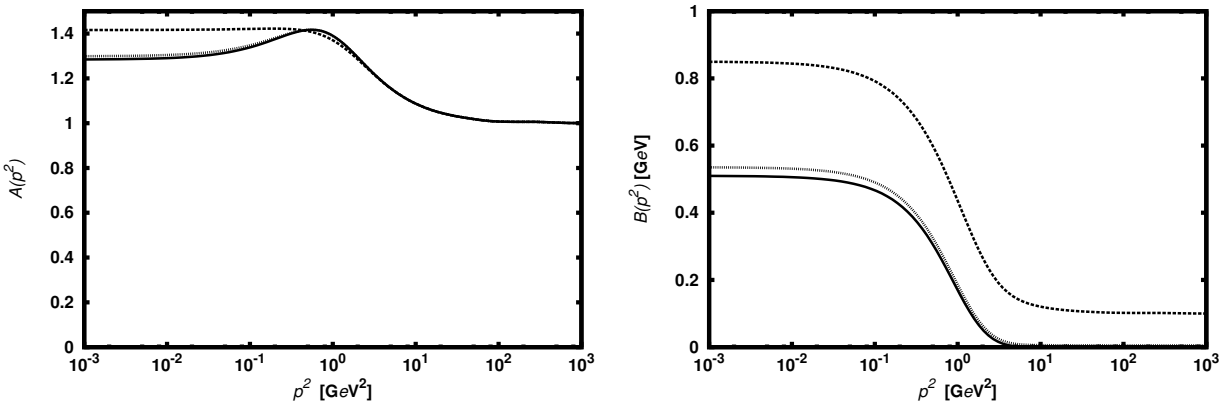

(a) Dressing of the Dirac part A.

(b) Dressing of the scalar part B.

Figure 3.1.1: Dressing functions in vacuum as a solution of Eq. (2.4.8) for three different bare quark masses: $m = 5\,\mathrm{MeV}$ (short-dashed), $m = 100\,\mathrm{MeV}$ (dashed) and $m = 0$ (solid).

(A, B) which are defined on their respective grids. A possible metric d reads

$$d\left((A_k, B_k), (A_l, B_l)\right) := \frac{1}{n^{\mathrm{le}}} \sum_{i=1}^{n^{\mathrm{le}}} \left[\left(A_k(x_i) - A_l(x_i)\right)^2 + \left(B_k(x_i) - B_l(x_i)\right)^2 \right]. \tag{3.1.5}$$

with $(A_k, B_k), (A_l, B_l) \in \{S\}$ [5]. The normalization to the number of Gauss-Legendre nodes n^{le} provides comparability for distances measured in different spaces. The iteration carries on until a given accuracy acc is achieved, i.e. until

$$d\left((A_{k+1}, B_{k+1}), (A_k, B_k)\right) \leq acc, \tag{3.1.6}$$

where the index k denotes the iteration step.

In this section, the number of Gauss-Legendre nodes is set to $n^{\mathrm{le}} = 96$, that of the Gauss-Chebychev ones to $n^{\mathrm{ch}} = 64$, and the accuracy to $acc = 10^{-13}$. First, the initial functions read $A_0 \equiv 1$ and $B_0 \equiv 1\,\mathrm{GeV}$. Figure 3.1.1 shows the solution of the quark DSE for different bare quark masses and the chiral limit ($m = 0$). In view of the investigations at finite temperatures, at least the feature of dynamical chiral symmetry breaking (DCSB) has to be mentioned. As argued in Sec. 2.4 the function $M = B/A$ can be interpreted as mass function. Its dependency w.r.t. the momentum is depicted in Fig. 3.1.2. The mass function M is a dynamical function with large values for low momentum squares and small values for large momentum squares. Considering the case $m = 0$ (solid line in Fig. 3.1.2) M remains zero for $p^2 > 100\,\mathrm{GeV}^2$, which corresponds to massless chirally symmetric quarks. For

[5] The summation in Eq. (3.1.5) concerns the numerical values of A and B ignoring their (different) mass dimensions.

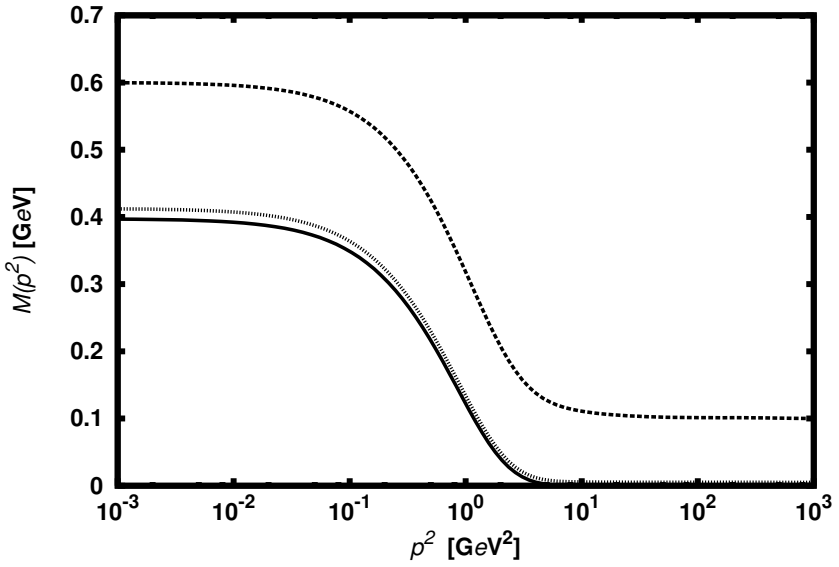

Figure 3.1.2: Mass function $M = B/A$ for three different bare quark masses: $m = 5\,\mathrm{M}e\mathrm{V}$ (short-dashed), $m = 100\,\mathrm{M}e\mathrm{V}$ (dashed) and $m = 0$ (solid).

$p^2 \lessapprox 10\,\mathrm{G}e\mathrm{V}^2$ quarks acquire a significant amount of mass (exceeding the value of 1/3 of the nucleon masses [6]), which indicates the chiral symmetry to be broken. Consequently, the model describes chiral symmetry breaking as a dynamical phenomenon.

In case of $m \neq 0$, the chiral symmetry is explicitly broken for all momenta. The mass function tends to the bare quark mass at large momentum squares rather than to zero (dashed and short-dashed lines, respectively). Considering this limit of the mass function as an approximation to chiral symmetry the dynamical breaking of this symmetry occurs in the same manner as in case of zero bare quark mass. An analogous result recurs in Sec. 4.1, where the chiral phase transition is investigated.

The last part of this section introduces another class of solutions to the quark DSE for the $m = 0$ case. A glance at the system of integral equations in Eq. (2.4.8) reveals that $B \equiv 0$ solves the equation for scalar dressing part and reduces the system to one integral equation, i.e. that for the Dirac dressing part A [7]. Figure 3.1.3 shows the solution for the remaining equation for initial function $A_0 = 1$ in comparison with the solution of the full system of equations given in Fig. 3.1.1. The solution $B \equiv 0$ explicitly disables DCSB. This mode is referred to as Wigner-Weyl (WW) solution, while $B \not\equiv 0$ is referred to as

[6] In the constituent quark model, the quark masses range between 300 and 500 $\mathrm{M}e\mathrm{V}$ [Gri08] for the first quark generation and the strange quark.

[7] From the perspective of finding fixed-points of the integral operator defined by Eq. (2.4.8) the choice $B_0 \equiv 0$ leads the iteration to a fixed-point with $B \equiv 0$. For a given small deviation of B_0 (e.g. 10^{-20} at a single grid point) the system will converge to the solution shown in Fig. 3.1.1. This behaviour characterizes the solution with $B \equiv 0$ as an unstable fixed-points.

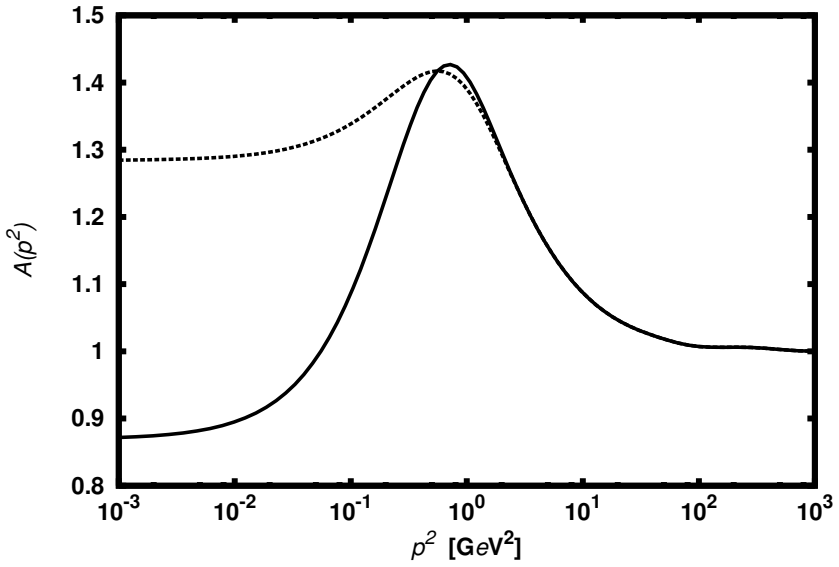

Figure 3.1.3: Dressing function A of the Wigner-Weyl solution (solid line) in comparison with that of the Nambu-Goldstone solution (dashed line).

Nambu-Goldstone (NG) solution [8].

3.2 Non-zero temperature solutions

This section first adapts the numerical approach of the vacuum-quark DSE (Sec. 3.1) to the quark DSE at non-zero temperatures (2.5.18) and elaborates on the necessary extensions and the inherent peculiarities. Afterwards, the solution of the non-zero-temperature DSE is discussed under different aspects.

3.2.1 Numerical approach

Comparing the truncated quark Dyson-Schwinger equation for zero and non-zero temperatures, i.e. Eqs. (2.4.8) and (2.5.18), the main difference is the additional dimension of the dressing functions' domain corresponding to the time-like momentum coordinate. This coordinate involves the summation in the self-energy integral in the DSE at non-zero temperatures. Furthermore, the complexity of the equations at non-zero temperatures complicates finding a solution by a method other than direct iteration. Thus, as motivated

[8] Equation (2.4.8) provides a further NG-like solution, which is obtained in the same manner as finding the WW solution. Multiplication of the function B with -1 transforms Eq. (2.4.8) identically (except a global minus sign in the second equation). Thus, a third solution is achieved by using negative initial conditions for B. It is identical to the ordinary (NG) solution except for the global minus in front of the values of B.

for the case of zero temperature the equations for the case of non-zero temperatures will be solved by direct iteration. For this purpose, the numerical integration and the treatment of the infinite sum have to be discussed.

Like in the vacuum case the Gauss-Legendre quadrature (cf. Eqs. (3.1.3) and (3.1.4)) can be used for the momentum integration. Since the angular integration $\int \mathrm{d}t$ in Eq. (2.5.18) lacks the weight function $\sqrt{1-t^2}$, here, the application of Gauss-Legendre for this integral seems to be appropriate, too. Approximating the angular and momentum integration via Gauss-Legendre and applying the momentum mapping corresponding to Eq. (3.1.3) converts the integral in Eq. (2.5.18) to

$$\begin{aligned} \int_0^\infty \mathrm{d}\lambda\, \lambda^2 \int_{-1}^{1} \mathrm{d}t f(\lambda, t) &= 2\, {p_0}^3 \int_{-1}^{1} \mathrm{dx} \frac{(1+x)^2}{(1-x)^4} \int_{-1}^{1} \mathrm{dt}\, f(\lambda(x), t) \\ &\approx 2\, {p_0}^3 \sum_{i=1}^{n_\lambda} \sum_{j=1}^{n_t} \frac{(1+x_i)^2}{(1-x_i)^4}\, \alpha_i\, \alpha_j\, f(\lambda(x_i), t_j) \end{aligned} \tag{3.2.1}$$

with α_i and α_j denoting the weights and x_i and t_i denoting the nodes of the Gauss-Legendre quadrature.

The remaining infinite sum over the Matsubara frequencies cannot be calculated explicitly [9]. An approximation to the infinite summation is to loosen the constraint of (anti-) periodicity of the (quark) gluon fields for higher momenta. In this approach, the summation is carried out symmetrically up to a certain index. Assuming a continuous distribution of the higher frequencies, the sum over the respective indices is approximated by integration. Indeed, since Matsubara frequencies are equally spaced, the difference between two Matsubara frequencies relative to their absolute value decreases for an increasing index value. On the other hand, this integration can be omitted if the self-energy is UV convergent because in this case, higher frequencies do not contribute significantly. The gluon dressing, Eq. (2.5.16), is UV convergent, which is why the integration of the higher frequencies contribution is dropped for the further discussion.

It depends on the temperature, how many frequencies have to be taken into account. With $-\hat{n}$ and $\hat{n}$ being the extremal indices of the frequencies symmetrically taken into account, i.e. $\omega_i \in \{\omega_{-\hat{n}}, \ldots, \omega_{\hat{n}}\}$, the square momentum reached by the highest available gluon frequency reads

$$p^2(\Omega_{-\hat{n}\hat{n}}) = (\pi T(2(-\hat{n}) - 2\hat{n})^2 = 16\pi^2 T^2 \hat{n}^2. \tag{3.2.2}$$

Assuming a temperature independent threshold, which distinguishes between relevant and negligible momenta, the number of necessary Matsubara frequencies increases with the

[9] In case renormalization is needed, the respective UV cut-off would truncate the summation, anyway.

T[MeV]	10	30	100	130	200	300
$\hat{n}$	80	27	8	7	4	3
N	161	55	17	15	9	7

Table 3.2.1: Number N of necessary Matsubara frequencies at different temperatures T restricting to squared momenta $p^2/\mathrm{GeV}^2 \in [0, 100]$. $\hat{n}$ corresponds to the extremal quark Matsubara frequencies $\omega_{-\hat{n}}$ and $\omega_{\hat{n}}$.

square of the inverse temperature. Taking into account the vacuum solution given in Fig. 3.1.1 [10] may allow to restrict the domain of necessary squared momenta to $p^2/\mathrm{GeV}^2 \in [0, 100]$. In Fig. 3.1.1, the quark dressing functions seem to have negligible momentum dependence at squared momenta $p > 100\,\mathrm{GeV}^2$. Due to momentum conservation the maximum squared momentum of the gluons $\hat{q}^2$ is of the same order. Considering $\hat{q}^2 = \hat{p}^2$ Tab. 3.2.1 lists the number of necessary Matsubara frequencies for several temperatures assuming $p^2(\Omega_{-\hat{n}\hat{n}}) = 100\,\mathrm{GeV}^2$. In praxi, the number of frequencies taken into account might be chosen smaller than suggested by the previous consideration. At frequencies in the neighbourhood of ω_0, the solutions for smaller and higher $\hat{n}$'s do not differ significantly (cf. App. H).

Truncating the summation at $\hat{n}$ and $-\hat{n}$ specifies an additional grid parameter. To enable statements about the iteration progression the difference between two solutions can be defined as (cf. Eq. (3.1.5))

$$\begin{aligned} d\left((A_k, B_k, C_k), (A_l, B_l, C_l)\right) \;:=\; & \frac{1}{n^{\mathrm{le}}\hat{n}} \sum_{i=1}^{n^{\mathrm{le}}} \sum_{m=-\hat{n}}^{\hat{n}} \Big[\left(A_k(x_i, \omega_m) - A_l(x_i, \omega_m)\right)^2 \\ & + \left(B_k(x_i, \omega_m) - B_l(x_i, \omega_m)\right)^2 \\ & + \left(C_k(x_i, \omega_m) - C_l(x_i, \omega_m)\right)^2 \Big] . \end{aligned} \tag{3.2.3}$$

The relation

$$d\left((A_{k+1}, B_{k+1}, C_{k+1}), (A_k, B_k, C_k)\right) \leq acc \tag{3.2.4}$$

defines the termination condition for the iteration with k denoting the iteration step. The calculations at non-zero temperatures use $n_\lambda = n_t = 64$ Gauss-Legendre nodes and the numerical initial values of the iteration are $A_0 \equiv B_0 \equiv C_0 \equiv 1$. As will be described in Sec. 4.1, especially in the neighbourhood of the critical temperature of chiral symmetry restoration, the convergence becomes rather slow. For this reason, the tolerance must

[10] Using the findings of the vacuum solutions is reasonable, since the low-temperature solution approximate the vacuum solution (cf. Sec. 3.3).

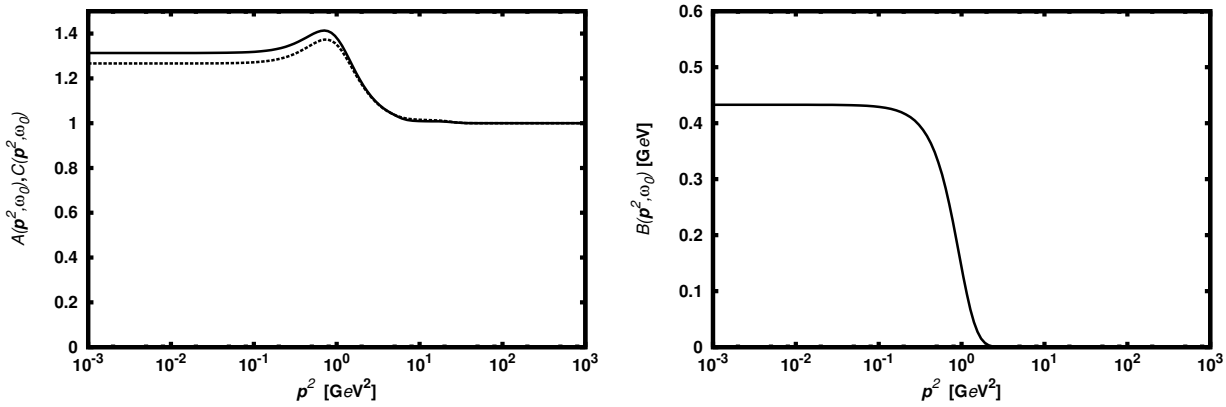

(a) Dressing A (solid) and C (dashed). **(b)** Dressing B.

Figure 3.2.1: Quark dressing functions at $T = 100\,\mathrm{MeV}$ as a solution of Eq. (2.5.17) shown for the lowest Matsubara frequency ω_0.

be chosen tighter than in the vacuum case [11]. $acc = 10^{-15}$ is used for the temperature calculations.

3.2.2 An exemplary solution

Figure 3.2.1 shows the solution of the quark DSE at $T = 100\,\mathrm{MeV}$ in the chiral limit ($m = 0$) for the lowest Matsubara frequency [12]. The shapes of the dressing functions A and B resemble those of the vacuum solution shown in Fig. 3.1.1. Furthermore, the dressing function of the time-like component C has a similar shape to that of the spatial component A. Note that the abscissa is labelled with spatial squared momenta $\boldsymbol{p}^2$ instead of full square momenta p^2 as in the vacuum case.

Comparing curves differently labelled in this manner is valid since the squared momentum at non-zero temperatures equals $p_n^2(T) = \boldsymbol{p}^2 + \omega_n^2$. Due to this relation, labelling with full squared momentum only brings a shift to higher numerical values. Thus, both representations have a comparable content. The full square momentum $p_n^2(T)$ has a finite minimum value $p_0^2(T) = p_{-1}^2(T) = \pi^2 T^2$. At small momenta, the values of C are slightly below that of A. The difference almost vanishes for squares of the spatial momentum larger than $1\,\mathrm{GeV}^2$. In the limit of large momenta, the dressings A and C are numerically one.

The scalar dressing function B acquires non-zero values only for low momenta, which

[11] Strictly speaking, comparability of the metrics defined in Eqs. (3.1.5) and (3.2.3) calls for a normalization w.r.t. the number n^{dr} of dressing functions, too. Thus, when migrating from zero to non-zero temperature, the required tightening of the precision is actually even stronger than described above (by factor 3/2).

[12] The term "lowest Matsubara frequency" refers to ω_0, since it has the lowest available absolute value of the Matsubara frequencies.

demonstrates dynamical chiral symmetry breaking [13]. At large momenta, B is strictly zero [14]. Consequently, taking into account the asymptotic behaviour of A and C the quark propagator degenerates to the bare quark propagator at large momenta. Up to now, this statement only holds for the lowest Matsubara frequency ω_0. For this reason, consider the surface plots of Fig. 3.2.2 broadening the view to multiple frequencies. Here, white curves represent the (actual) solution of the quark Dyson-Schwinger equation for the positive Matsubara frequencies at $T = 100\,\mathrm{MeV}$. Since the Matsubara frequencies are discretely distributed, surfaces only serve as eye guides. Concerning large momenta the statement of the asymptotic propagator to be the bare quark propagator holds also for frequencies other than ω_0. Furthermore, also in the limit of large frequency indices, the dressing functions exhibit the same behaviour. Therefore, the formalism of finite temperatures as introduced in Sec. 2.5 seems to implement no additional effects at large momenta.

To underline this finding and to allow for quantitative statements Fig. 3.2.3 shows the dressings A and B at different frequencies. The spatial square momentum is given using linear scaling to simplify comparison between the different frequencies and, additionally, to get a picture of the dressing functions' shape on linear scale. At first, the curves approve the trend of the surface plots. Already at the fifth Matsubara frequency ω_5, almost no non-trivial dressing is acquired. In particular, the scalar dressing B vanishes at the whole momentum range; only Dirac dressing A slightly differs from the dressing of the bare case. Referring to Tab. 3.2.1 the solution for ω_9 is displayed as a thin solid curve. With regard to B the truncation of the summation at $\hat{n} = 8$ is legal, since the B does not differ from the bare value for frequencies higher than $\omega_{\hat{n}}$ (in Fig. 3.2.3, the curve of ω_9 is hidden behind that of ω_5).

On the contrary, A does exhibit a small deviation from the respective bare value, which is why the truncation at $\hat{n} = 8$ may be argued to be a too strong approximation to the solution of the quark DSE (2.5.18) [15]. Both A and also C differ less than 10^{-2} from the bare value on the whole momentum grid only for frequencies higher than ω_16 [16]. Within the numerical evaluations at non-zero temperatures related to the thesis at hand, vanishing of non-trivial dressing for A and C like in the B case was hardly observed. With regard to the numerical

[13] The scalar dressing function $B(0, \omega_0)$ at zero momentum and lowest Matsubara frequency is argued to be an order parameter for chiral symmetry itself (cf. Sec. 4.1).

[14] According to the initial values of the iteration and the preceding number of iterations, B exhibits finite numerical values. These decrease for each further iteration.

[15] The solution presented in Figs. 3.2.1 - 3.2.3 belongs to truncation at $\hat{n} = 100$. This value is chosen that high to allow for discussing truncation as argued by Tab. 3.2.1. For the calculations in Ch. 4 the number of Matsubara frequencies taken into account respects Tab. 3.2.1 using a few extra frequencies as buffer.

[16] The term "frequencies higher than ω_n" implicates the term "frequencies lower than ω_{-n-1}" since the solutions are independent of the sign of the Matsubara frequencies (cf. Sec. 3.3).

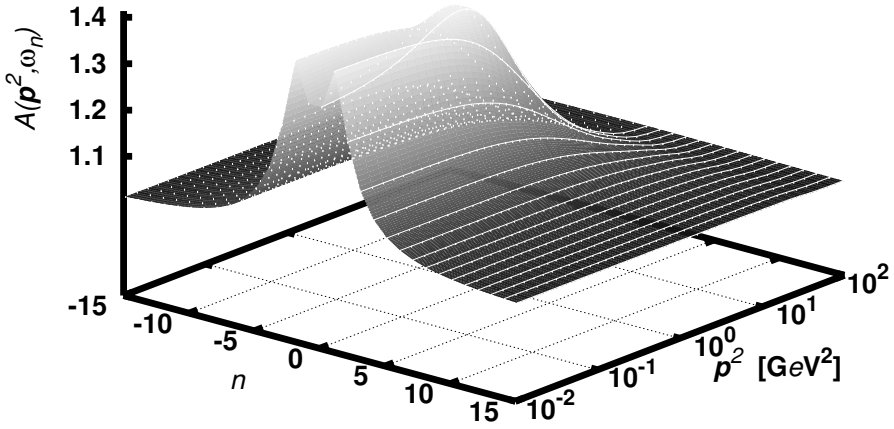

(a) Dressing A.

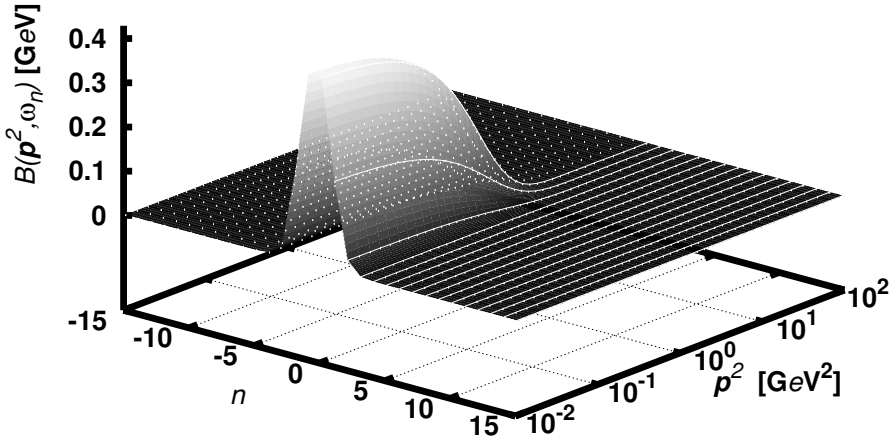

(b) Dressing B.

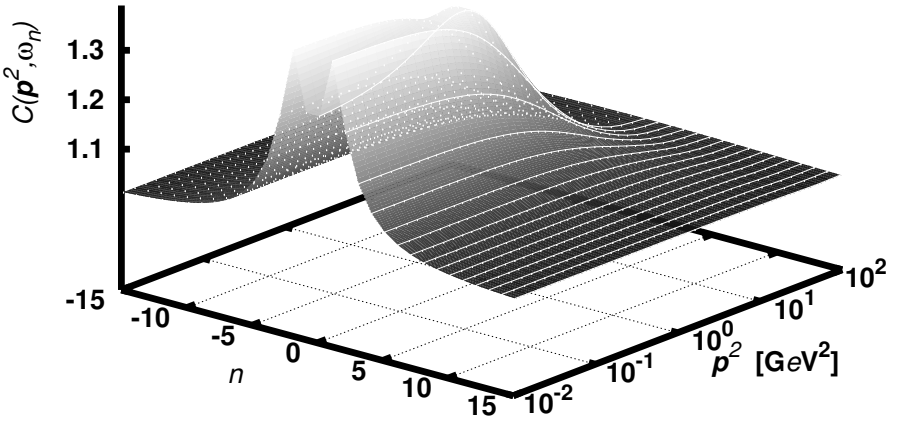

(c) Dressing C.

Figure 3.2.2: Quark dressing functions at $T = 100\,\mathrm{MeV}$ as a solution of Eq. (2.5.17). The actual solution for the positive Matsubara frequencies is represented by white curves.

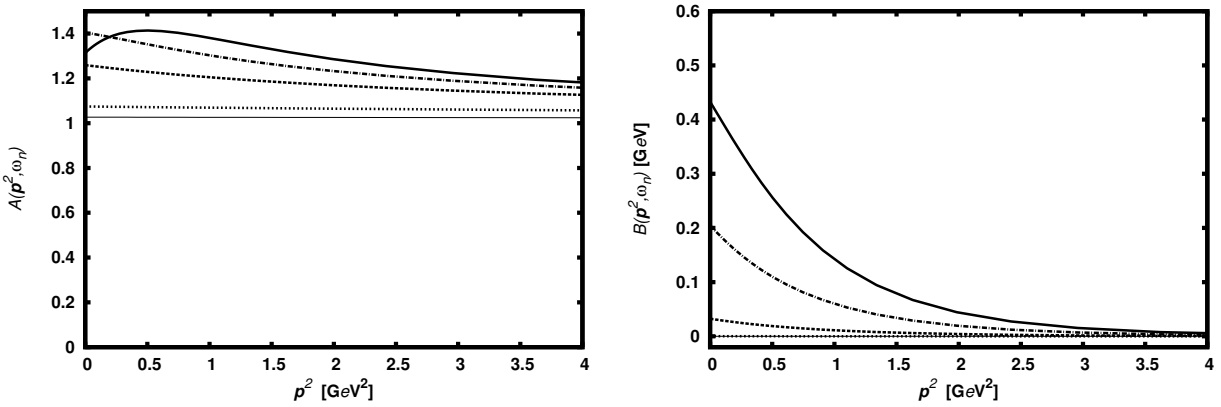

(a) Dressing A. **(b)** Dressing B.

Figure 3.2.3: Quark dressing at $T = 100\,\mathrm{MeV}$ for multiple frequencies ω_n: ω_0 (solid), ω_1 (dot dashed), ω_2 (dashed), ω_5 (short dashed), ω_9 (solid thin).

results presented in Figs. 3.2.1 - 3.2.3 the bare quark propagator is established for spatial squared momenta $\boldsymbol{p}^2 \gtrapprox 10^4\,\mathrm{GeV}^2$. Probably, as an effect of mapping the infinite momentum range to finite integration boundaries, the dressing becomes bare for all frequencies at once. Nevertheless, this fact numerically shows the neglect of renormalization (cf. Sec. 2.3) to be acceptable. The quark propagator fits the supposed renormalization condition

$$S(\boldsymbol{p},\omega_n)|_{\boldsymbol{p}^2=\mu^2,\omega_n=\omega_0} \stackrel{!}{=} S_0 \quad [17] \tag{3.2.5}$$

with $\mu = 100\,\mathrm{GeV}$.

Discussing lower momenta in combination with high frequencies "bareness" was not observed for any number $N = 2\hat{n}+1$ of frequencies taken into account and any level of tolerance *acc*. Compared with $\mu = 100\,\mathrm{GeV}$ in Eq. (3.2.5) and with Tab. 3.2.1, trivial dressing was expected for frequencies higher than ω_8. Thus, the finite temperature formalism implements a certain effect at high momenta p^2, which revises the first conjecture after examining Fig. 3.2.2.

One further aspect to discuss through Fig. 3.2.3 is the shift of the curves along the abscissa. Supposing the abscissa to be labelled with the full square momentum p^2 the

[17] In general, such renormalization condition is established by setting the renormalization constants appropriately. When iterating the system of equations for the dressing functions, those constants have to be adjusted after each new iteration. Practically speaking, having three dressing functions introduces three more grid points to be iterated. Note that setting the renormalization constants only at the end after iteration causes inconsistency, which is why the quark propagator "renormalized" this way would not fit the quark DSE that was iterated before.

curves start with an horizontal offset of ω_n^2. Their mutual shift is

$$\Delta_{kl} := |\omega_k^2 - \omega_l^2|. \tag{3.2.6}$$

At $T = 100\,\mathrm{M}e\mathrm{V}$, the offsets of the solutions at ω_0 and ω_1 differ from each other by $\Delta_{01} \approx 0.8\,\mathrm{G}e\mathrm{V}^2$. Further shifts are $\Delta_{12} \approx 1.6\,\mathrm{G}e\mathrm{V}^2$ and $\Delta_{01} \approx 2.4\,\mathrm{G}e\mathrm{V}^2$. Now, shifting the curves in Fig. 3.2.3 by the corresponding ω_n (or using Δ_{kl}) the values of A and B are similar for all curves. This discussion is continued in Sec. 3.3, where the shift is explicitly carried out for the comparison of low-temperature solutions and the vacuum solution. Nevertheless, the peaking of A, e.g., is shown to be an p^2 induced effect. Furthermore, the observation of similar values revealed by the anticipated shift, above, indicates that the destruction of the vacuum O(4) symmetry is moderate. This finding supports the picture mediated by Fig. 3.2.1, where time-like Dirac dressing C and spatial Dirac A only slightly differ from each other. Section 3.2.4 elaborates on the amount of destruction of O(4) symmetry in dependence of the temperature.

3.2.3 Wigner-Weyl solution

In comparison with the coupled equations for the dressing functions in the zero-temperature case, the equations at non-zero temperatures (2.5.13) allow for transformations of the function B, as well. Multiplication of B with zero leaves two equations for A and C. The corresponding solution of the remaining system is called Wigner-Weyl solution (cf. Sec. 3.1). Figure 3.2.4 presents this solution. Unlike the WW solution in vacuum (cf. Fig. 3.1.3), at $T = 100\,\mathrm{M}e\mathrm{V}$, dressing function A does not drop below the value one for small momenta. A discussion of the shift by ω_n^2 to establish the representation in dependency on the full squared momentum p^2 was given at the end of Sec. 3.2.2. This shift makes values $A < 1$ unavailable, because the smallest Matsubara frequency makes up a squared momentum $p_{n=0}^2 \approx 0.8\,\mathrm{G}e\mathrm{V}^2$, while the values $A < 1$ are supposed to be found for $p^2 \lessapprox 0.1\,\mathrm{G}e\mathrm{V}^2$ (cf. Fig. 3.1.3).

A qualitative examination at multiple frequencies reveals no differences between the WW case dressings A_{WW} and C_{WW} and the NG case dressings A_{NG} and C_{NG}. Only the gap between the lowest and the next frequency in the low momentum range increases significantly. This results from non-zero B being damped to the reduced dressing functions (cf. Eq. (C.19)) in the NG case. The WW case prohibits this damping by definition.

Before closing this section, note that multiplication of B in Eq. (2.5.13) with -1 also leads to a new class of solutions, i.e. A and C remain invariant and B acquires a global minus sign. This solution may be referred to as “inverse NG solution”.

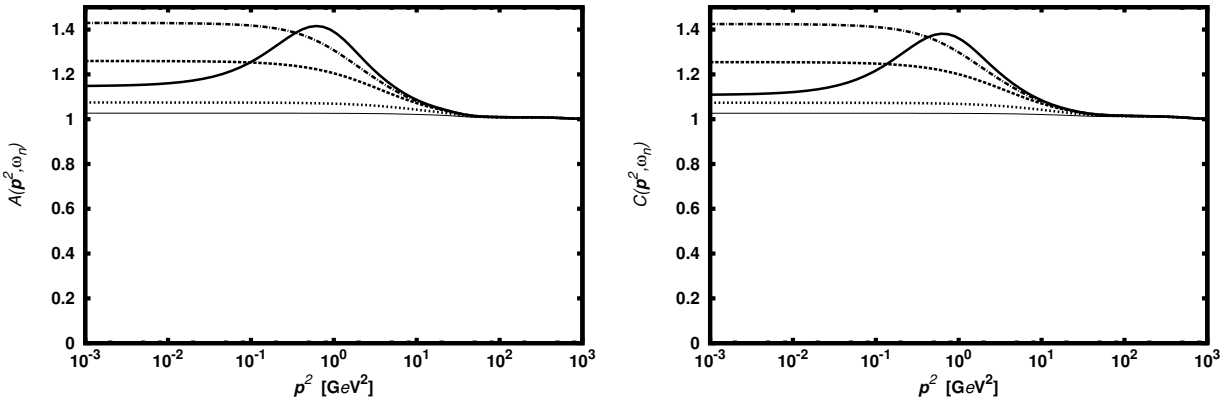

(a) Quark dressing A (left) and C (right) for multiple frequencies ω_n: ω_0 (solid), ω_1 (dot dashed), ω_2 (dashed), ω_5 (short dashed), ω_9 (solid thin).

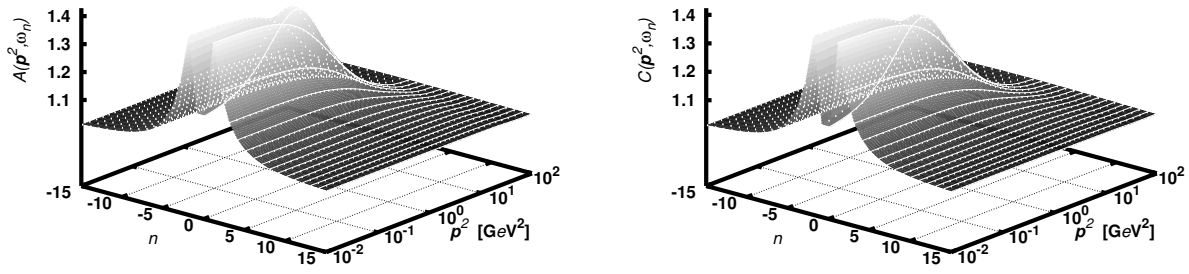

(b) Dressing A.

(c) Dressing C.

Figure 3.2.4: Quark dressing functions A and C at $T = 100\,\mathrm{MeV}$ as a solution of Eq. (2.5.17) in the WW mode, where $B \equiv 0$. In (b) and (c), white curves represent the solutions for the positive Matsubara frequencies. The surface serves as eye guide.

3.2.4 Temperature dependence

After studying solutions of the quark Dyson-Schwinger equation at non-zero temperatures, this subsection discusses effects of varying the temperature. If not indicated differently the following discussion refers to the NG solution introduced in Sec. 3.2.2, i.e. to the solution with potentially non-zero B. The WW solution, i.e. the solution B constraint to zero, only serves to illustrate the effect of chiral symmetry restoration.

Figure 3.2.5 displays the temperature dependence of the dressing functions for the lowest Matsubara frequency [18]. The vacuum data is included to establish curves and surfaces

[18]The left column of Fig. 3.2.5 can be compared with results in [Mo10] as has been done to confirm that the numerical code for the solution of the quark DSE works properly.

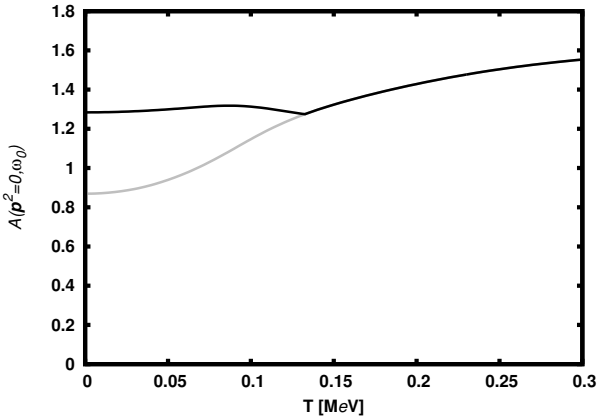

(a) Dressing $A(0, \omega_0)$.

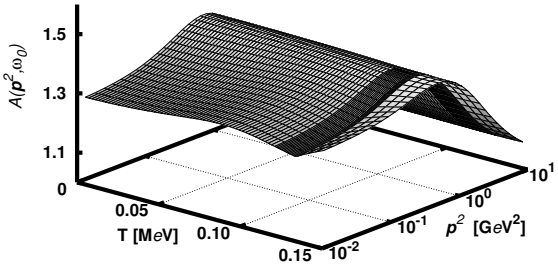

(b) Dressing $A(\boldsymbol{p}^2, \omega_0)$

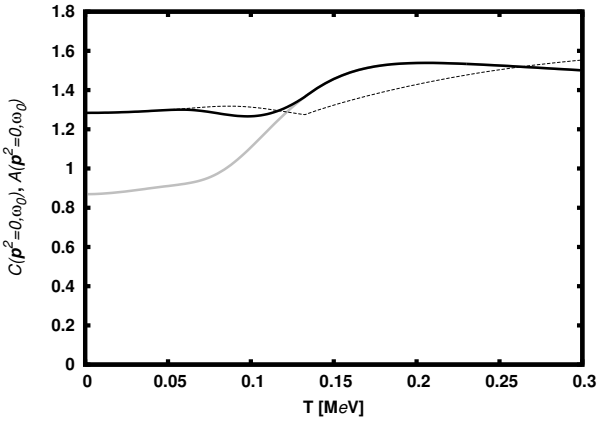

(c) Dressing $C(0, \omega_0)$.

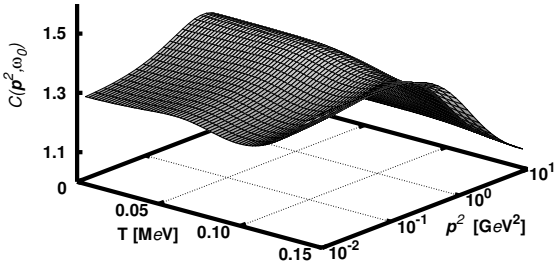

(d) Dressing $C(\boldsymbol{p}^2, \omega_0)$.

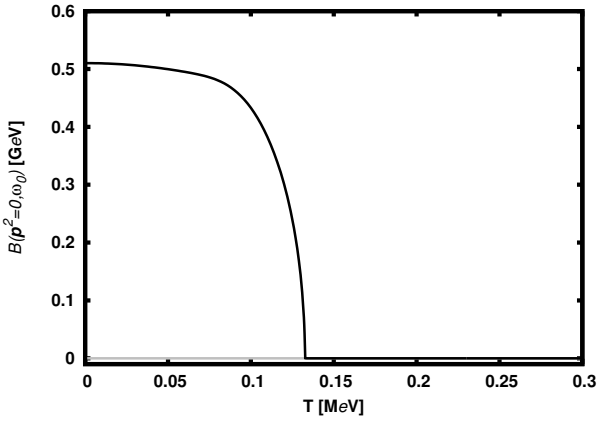

(e) Dressing $B(0, \omega_0)$.

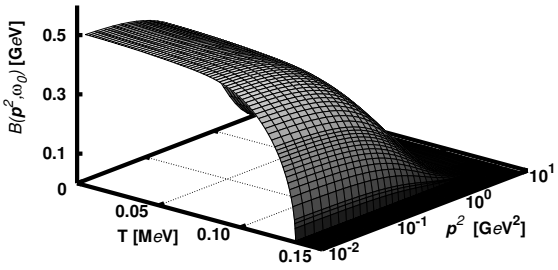

(f) Dressing $B(\boldsymbol{p}^2, \omega_0)$.

Figure 3.2.5: The quark dressing functions in dependency on the temperature:
The NG mode is represented at the lowest Matsubara frequency ω_0 and zero momentum $\boldsymbol{p}^2 = 0$ by thick black lines (left column) and for a continuous part of the whole spatial momentum range $\boldsymbol{p}^2$ (right column). The thin dashed line in Fig. (c) displays the dressing A in the NG mode for comparison.
The WW mode is represented at the lowest Matsubara frequency ω_0 and zero momentum $\boldsymbol{p}^2 = 0$ by thick grey lines (left column).

beginning at temperature $T = 0$. The left column shows the temperature dependence of the quark dressing for the lowest Matsubara frequency ω_0 and at zero spatial momentum $\boldsymbol{p}^2 = 0$ [19]. Black and grey lines display the NG and WW solution, respectively. For comparison Fig. 4.3.1c displays besides the curve of $C(0, \omega_0)$ that of $A(0, \omega_0)$ (thin dashed curve) in the NG mode given also in Fig. 4.4.3a. The right column shows the dressing in the NG mode for a continuous part of the momentum range to give a qualitative view on squared momenta p^2 other than the lowest.

Discussing the temperature dependency at $(\boldsymbol{p}^2, \omega_n) = (0, \omega_0)$ one observes that the dressing functions do only marginally change at low temperatures. The system approximately remains at its vacuum specifications. At about $T = 10\,\mathrm{MeV}$, deviations begin to grow. Especially, B changes with increasing slope. Note that the curves of A and C stick together until about $T = 50\,\mathrm{MeV}$. Hence, O(4) symmetry is destroyed significantly only for temperatures higher than $T = 50\,\mathrm{MeV}$ [20]. Between $T = 80\,\mathrm{MeV}$ and $T = 100\,\mathrm{MeV}$, A and C pass a local maximum and a local minimum, respectively. These are slightly displaced from each another. In this region, the slope of $B(0, \omega_0)$ begins to increase with an even higher rate compared to lower temperatures. With respect to the discussion of chiral symmetry restoration (cf. Sec. 4.1) this region might be considered as where the process of restoration starts. The curve of $B(0, \omega_0)$ tends to become a vertical and drops to zero between $T = 132\,\mathrm{MeV}$ and $T = 133\,\mathrm{MeV}$.

Discussing the numerical results, the dropping temperature is located between $T = 132.4\,\mathrm{MeV}$ and $T = 132.8\,\mathrm{MeV}$. In this region, the temperature was scanned by steps $\Delta T = 0.2\,\mathrm{MeV}$ and with a maximum number of iterations $\hat{n}_{\mathrm{it}} = 3000$. At $T = 132.6\,\mathrm{MeV}$, this number is not sufficient to establish the requested precision $acc < 10^{-15}$ (only $acc_{\hat{n}_{\mathrm{it}}} < 10^{-14}$ is achieved). This behaviour signifies a change in the characteristic of the NG solution of the quark DSE. That is, the actual NG solution, which is characterized by $B \neq 0$, vanishes and only the WW solution remains. In the left column of Fig. 3.2.5, this can be observed as the descent of the grey to the black curves [21].

The dropping of $B(0, \omega_0)$ forming a kink in its temperature dependence goes along with a kink in the temperature dependence of $A(0, \omega_0)$. Noticeably, $C(0, \omega_0)$ does not exhibit any peculiarities where $A(0, \omega_0)$ and $B(0, \omega_0)$ kink. This can be understood by picking up the discussion of beginning chiral symmetry restoration at $T = 50\,\mathrm{MeV}$. Chiral symmetry

[19] Since the the dressing functions are calculated on a grid not containing $\boldsymbol{p}^2 = 0$, the values of the dressing functions are linearly extrapolated to zero momenta. Note App. C.3.

[20] Comparing the numerical data of $A(0, \omega_0)$ and $C(0, \omega_0)$, up to $T = 22\,\mathrm{MeV}$ the values differ only in the tenth digit. At $T = 50\,\mathrm{MeV}$, the difference is lower than 10^{-3}. The occurrence of these differences have to be interpreted as an approximation to O(4) symmetry.

[21] If one considers the black curves in Fig. 3.2.5 as representing the actual NG solution rather than the solution with potentially non-zero B, these curves would end at $T \approx 132.6\,\mathrm{MeV}$.

restoration may be assumed to start when A and C begin to disconnect. In the context of the thesis at hand, this restoration is a temperature effect. Identifying $A(\boldsymbol{p}^2, \omega_n)$ and $B(\boldsymbol{p}^2, \omega_n)$ of the calculations at non-zero temperatures with $A(p^2)$ and $B(p^2)$ of those at zero temperature, these very functions sustain a final change when chiral symmetry is entirely restored. Interpreting a non-vanishing B as remnant of the vacuum case the dropping of B indicates the influence of vacuum effects to disappear completely. Considering C as a quantity that is given by the temperature formalism, a change in the vacuum induced specificities may let this quantity unaffected.

A feature of the temperature dependence of A and C is their intersection at $T = 262.5 \pm 2.5\,\mathrm{MeV}$. This will be picked up in Sec. 4.3.

With regard to the surface plots in Fig. 3.2.5 for low temperatures, the characteristic behaviour of the dressing functions along the $\boldsymbol{p}^2$ axis remains the same as that discussed in Sec. 3.2.2, though the magnitudes change (especially for B). At higher temperatures, only the scalar dressing $B(\boldsymbol{p}^2)$ changes its characteristic behaviour at $T \approx 132.6\,\mathrm{MeV}$, i.e. to uniformly vanishing values [22], while A and C practically keep their behaviour.

3.2.5 Solutions at non-zero masses

In the manner of Fig. 3.1.1, this section presents results for masses that correspond to the current quark masses of the first two quark generations. It serves as an introduction to Sec. 4.1.2, where the chiral phase transition is investigated for non-zero quark masses. Figure 3.2.6 shows the quark dressing for these masses and the chiral limit ($m = 0$) at $T = 100\,\mathrm{MeV}$ and $T = 200\,\mathrm{MeV}$ evaluated at the lowest Matsubara frequency [23]. Taking into account Sec. 4.1 those temperatures correspond to the non-chiral symmetric phase and the chiral symmetric phase, respectively (cf. Sec. 3.2.4). For increasing numerical value m the main trend seems to be given as a reduction of the temperature dependence, at least for the given temperature range. The curves of light quarks and those of the chiral limit have almost the same behaviour. Only the scalar dressing B exhibits a fundamental difference. At $T = 200\,\mathrm{MeV}$, $B_{(m=5\,\mathrm{MeV})}$ acquires values which are considerably above the bare value $B_{\mathrm{bare}} = 5\,\mathrm{MeV}$, i.e. $B_{(m=5\,\mathrm{MeV})}$ exhibits a considerable amount of DCSB also for temperatures higher than the critical temperature T_c [24]. This effect is even more

[22] For $T \gtrapprox 132.6\,\mathrm{MeV}$ the scalar dressing B vanishes at all squared momenta $p^2 = \boldsymbol{p}^2 + \omega_n^2$ as expected from a comparison with Fig. 3.2.2.

[23] In Fig. 3.2.7, note that the slight step appearing at $\boldsymbol{p}^2 \approx 20\,\mathrm{GeV}^2$ demonstrates the limitations of the numerical momentum integration. The effect disappears for increasing grid parameter $n^{\mathrm{le}} > 64$. It is accepted for the calculations within this thesis to reduce computing time (cf. Eq. (F.10)). This seems acceptable, since the respective momentum range contributes only marginally because of the gluon dressing's exponential (cf. Eq. (2.5.16)).

[24] The critical temperature of chiral symmetry restoration will be introduced in Sec. 4.1.1.

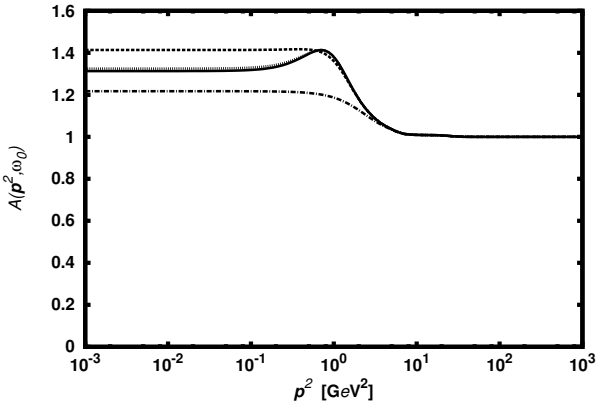

(a) Dressing A at $T = 100\,\mathrm{MeV}$.

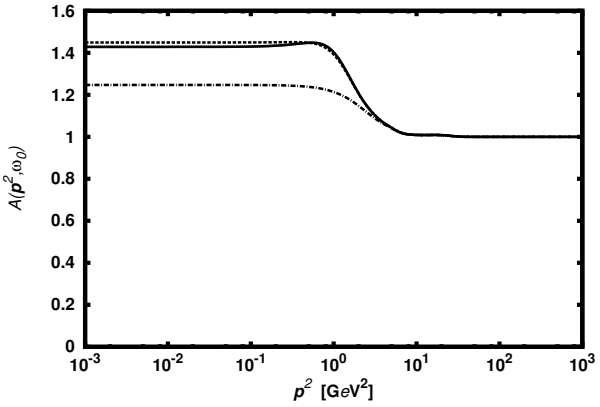

(b) Dressing A at $T = 200\,\mathrm{MeV}$.

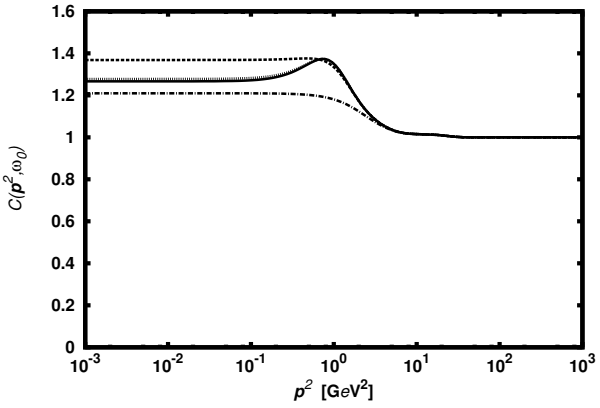

(c) Dressing C at $T = 100\,\mathrm{MeV}$.

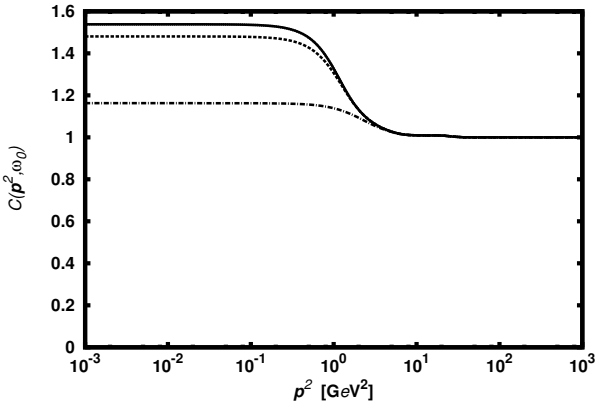

(d) Dressing A at $T = 200\,\mathrm{MeV}$.

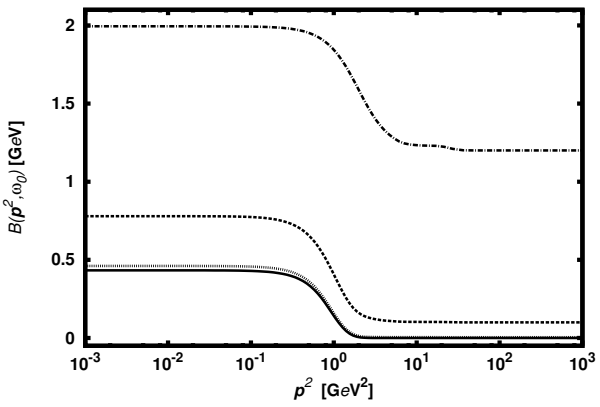

(e) Dressing B at $T = 100\,\mathrm{MeV}$.

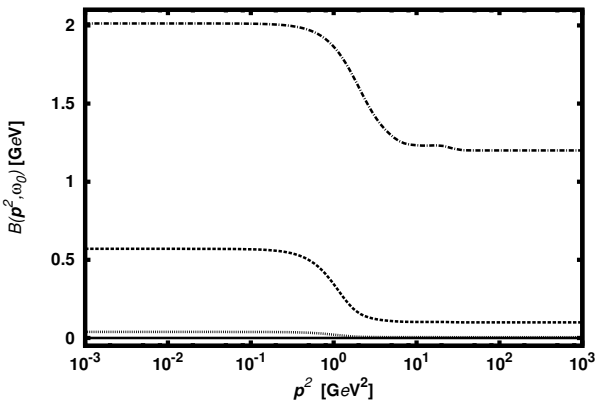

(f) Dressing B at $T = 200\,\mathrm{MeV}$.

Figure 3.2.6: Quark dressing functions for different values of m as a solution of Eq. (2.5.17) at $T = 100\,\mathrm{MeV}$ (left column) and at $T = 100\,\mathrm{MeV}$ (right column) shown for the lowest Matsubara frequency ω_0. Available values for the mass parameter:
$m = 0$ (solid), $m = 5\,\mathrm{MeV}$ (short-dashed),
$m = 100\,\mathrm{MeV}$ (dashed), $m = 1.2\,\mathrm{GeV}$ (dash-dotted).

pronounced for higher current quark masses. Eventually, the solution for the charm mass $m = 1.2\,\mathrm{G}e\mathrm{V}$ seems to be almost unaffected by the increase of the temperature. The investigations within this thesis focus on the chiral limit and light quark masses. Therefore, the difference between the cases of light and heavy masses is noticed as phenomenological fact only.

To show the scalar dressings' offset uniformly given via explicit chiral symmetry breaking (cf. [Hil12, Sec. 7.1.2]) Fig. 3.2.7 presents the solution for multiple Matsubara frequencies at $T = 200\,\mathrm{M}e\mathrm{V}$. Besides the offset and the effect of DCSB also for temperatures higher than T_c for the charm mass, this figure reveals reduced bumping of A and C along the n axis. This reduction is a consequence of the increased denominator of the integrands of A and C in the integral equations for the dressing functions (2.5.13).

3.3 Low temperatures

In this section, the limit of vanishing temperatures is investigated using the finite temperature formalism. As mentioned in the previous section at low temperatures, the solutions resemble those of the vacuum formalism. To compare the solutions extracted by these different settings one needs a common domain for the dressing functions. For this purpose, the full squared momentum p^2 and the spatial squared momentum $\boldsymbol{p}^2$ provide appropriate alternatives. Figure 3.3.1 illustrates the crucial point when switching between both domains. For a given squared momentum p^2 only certain frequency-spatial-momentum combinations can be used to set this value. Since the Matsubara frequencies are discretely distributed, the number of combinations is finite. The number depends on the respective squared momentum p^2 and on the temperature. For example, at $8\,\mathrm{M}e\mathrm{V}$, only the Matsubara frequencies from ω_{-20} to ω_{19} serve as possible values.

Using logarithmic scaling Fig. 3.3.2 displays the dressing functions at zero temperature (thin line) and non-zero temperatures (thick lines) at full squared momentum p^2 and different frequencies. Remarkably, all four curves coincide for square momenta higher than $p^2 \approx 1\,\mathrm{G}e\mathrm{V}^2$ [25]. The starts of the curves at non-zero temperature are each shifted by the respective square of the Matsubara frequency. Thus, not even the solution for ω_n^0 covers the vacuum solution. With respect to this the latter is uncovered only for low Momenta. Consequently, Fig. 3.3.2 shows the behaviour of the solution of the quark DSE at low temperatures that was expected, i.e. at low temperatures, the formalism approximates the vacuum case.

[25] The bump between $100\,\mathrm{G}e\mathrm{V}^2$ and $1000\,\mathrm{G}e\mathrm{V}^2$ is a numerical effect and vanishes for increasing the number of Gauss-Legendre nodes n^{le} (cf. Fn. 23).

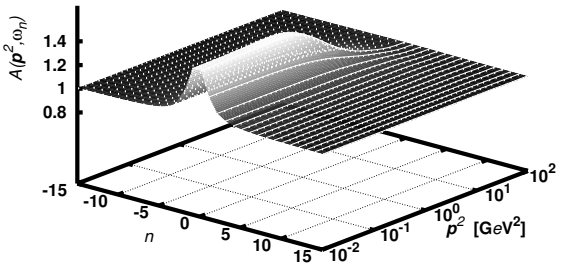

(a) Dressing A for $m = 5\,\mathrm{M}e\mathrm{V}$.

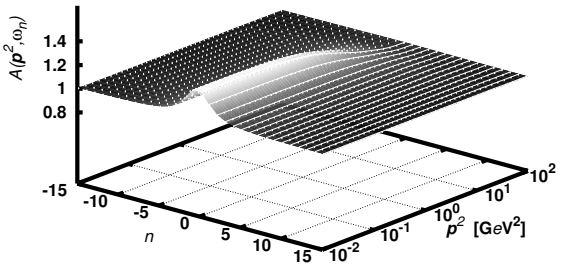

(b) Dressing A for $m = 1.2\,\mathrm{G}e\mathrm{V}$.

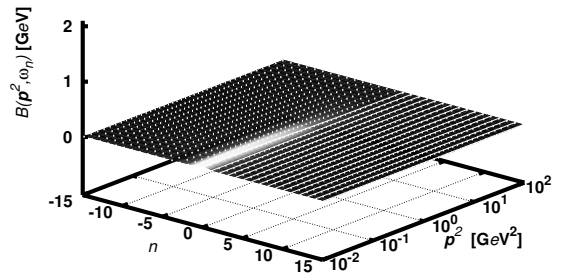

(c) Dressing B for $m = 5\,\mathrm{M}e\mathrm{V}$.

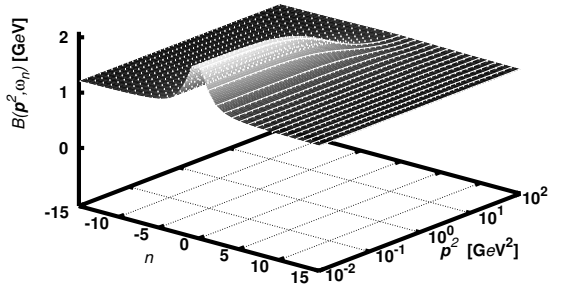

(d) Dressing B for $m = 1.2\,\mathrm{G}e\mathrm{V}$.

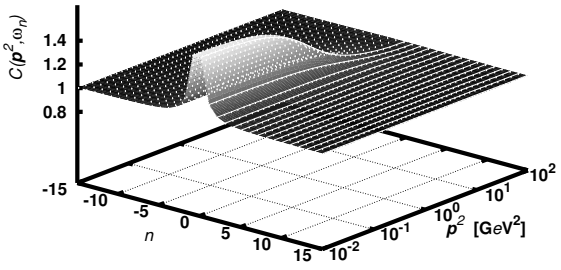

(e) Dressing C for $m = 5\,\mathrm{M}e\mathrm{V}$.

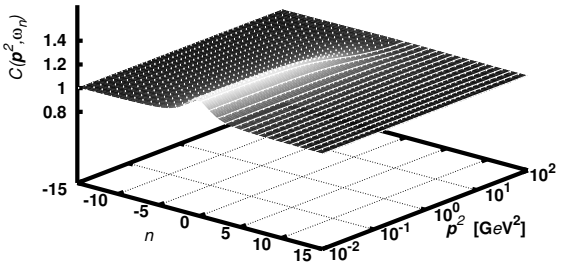

(f) Dressing C for $m = 1.2\,\mathrm{G}e\mathrm{V}$.

Figure 3.2.7: Quark dressing functions for $m = 5\,\mathrm{M}e\mathrm{V}$ (left column) and $m = 1.2\,\mathrm{G}e\mathrm{V}$ (right column) at $T = 200\,\mathrm{M}e\mathrm{V}$.

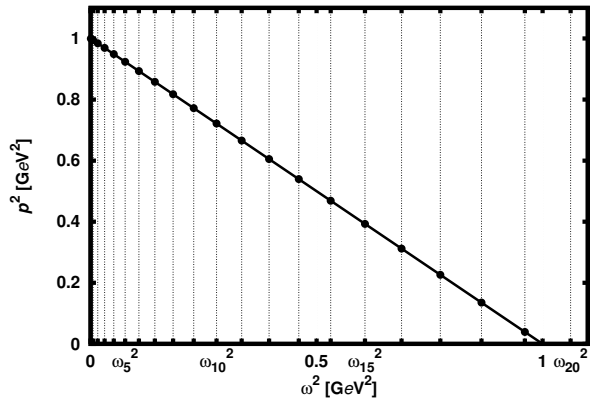

Figure 3.3.1: Spatial squared momentum $\boldsymbol{p}^2$ over time-like squared momentum ω^2. The grid displays the position of the squares of the Matsubara frequencies ω_n^2 at $T = 8\,\mathrm{MeV}$. Possible combinations of $(\boldsymbol{p}^2, \omega_n^2)$ to meet $p^2 = \boldsymbol{p}^2 + \omega_n^2 = 1\,\mathrm{GeV}^2$ are indicated by dots.

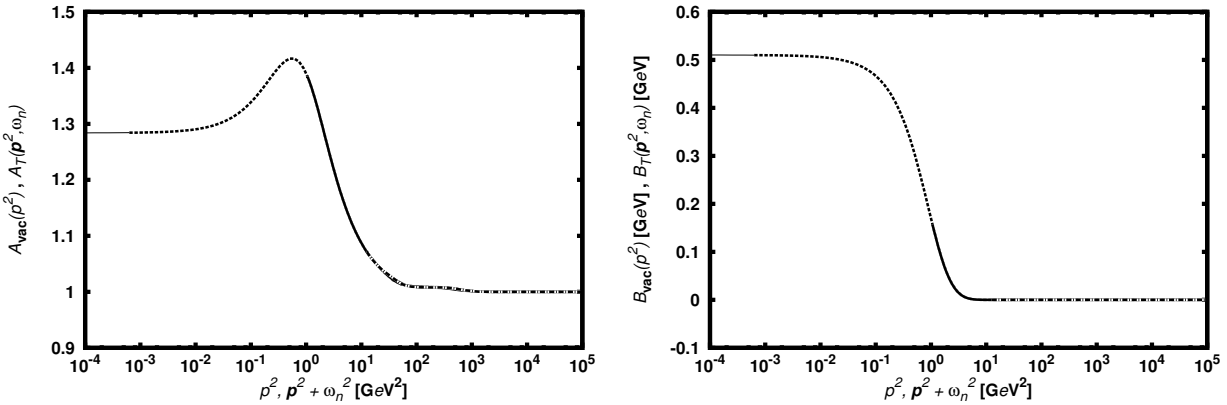

(a) Dressings A_{vac} and A_T.

(b) Dressings B_{vac} and B_T.

Figure 3.3.2: Comparison of the quark dressing at $T = 0$ (solid, thin) and at $T = 8\,\mathrm{MeV}$ for different Matsubara frequencies (thick): ω_0 (dashed), ω_{20} (solid), and ω_{70} (dash-dotted). Representation in dependency on the full squared momentum p^2. Except for low momenta, the curves of the $T = 0$ calculation are entirely covered.

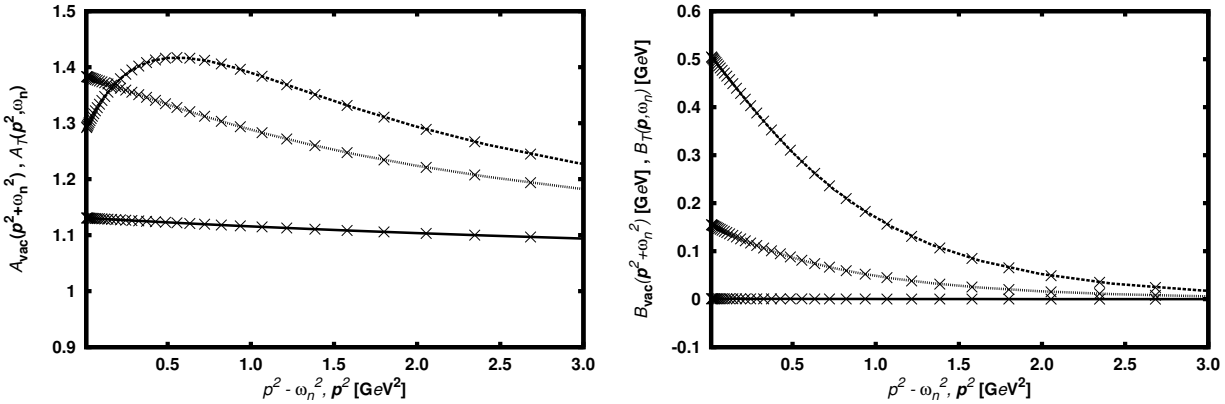

(a) **(b)**

Figure 3.3.3: Quark dressing at $T = 8\,\mathrm{MeV}$ for different Matsubara frequencies (thick curves): ω_0 (dashed), ω_{20} (short dashed), and ω_{-50} (solid). Representation in dependency on the spatial squared momentum $\boldsymbol{p}^2$. The corresponding dressing at $T = 0$ is indicated by crosses.

To provide an additional view on the comparison of the two formalisms Fig. 3.3.3 presents the solutions in dependency on the spatial square momentum. Here, thick lines present the solution at $T = 8\,\mathrm{MeV}$ for ω_0 (dashed), ω_{20} (short-dashed) and ω_{-50} (solid). Crosses represent the corresponding vacuum solutions. The latter have been calculated as follows:

(i) Iteration of the solution as described in Sec. 3.1,

(ii) Given a certain $(\boldsymbol{p}^2, \omega_n)$ as required for Fig. 3.3.3 integration of Eq. (2.4.6) with $p^2 = \boldsymbol{p}^2 + \omega_n^2$.

Discussing Fig. 3.3.3 one can observe at least two details. First, these plots reproduce the findings obtained in Fig. 3.3.2, i.e. coincidence of the solution at low temperature and zero temperature. Second, using the linear scale of this plot, the shift between the solution for ω_0 and that for ω_{20}, i.e. $\Delta_{0\,20} \approx 1.3\,\mathrm{GeV}^2$, can be explicitly measured (cf. the discussion of Fig. 3.2.3).

Finally, this section closes with the remark that at low temperatures, the summation over the Matsubara frequencies seems to resemble numerical integration via rectangle method. Since at low temperatures, the distribution of frequencies is rather dense (compared to larger temperatures), the corresponding number of grid points (i.e. $p^2(n) = \omega_n^2$) in the crucial region of non-trivial dressing ($p^2 \in I \approx [0, 10\,\mathrm{GeV}^2]$) seems to be sufficient to scan the functions A, B, and C appropriately.

4 Characteristic features of the quark propagator

This part of the thesis is devoted to the properties of quarks and the QCD medium in general, which are accessible via the quark Dyson-Schwinger equation. The numerical results cover investigations of the chiral phase transformation and the deconfinement transition as well as an approach to find the dispersion relation of quarks in the chiral symmetric phase. In relation to solving the Bethe-Salpeter equation, the analytical structure of the quark propagator is considered in vacuum.

4.1 Chiral phase transition

To investigate the chiral symmetry this thesis considers the di-quark condensate $\langle\bar{q}q\rangle$ as an order parameter, which is in line with e.g. [Mar98, Rob00, Alk01]. In the chiral limit, this quantity can be calculated by the trace over the quark propagator S [Mar98, Rob00, Alk01]

$$\langle\bar{q}q\rangle = -\operatorname{tr}_{c,D}(S), \tag{4.1.1}$$

where the indices c and D indicate the trace to be performed for the color structure and the Dirac structure [1]. Having the quark propagator in momentum space the trace operation includes integration over the whole momentum range. At zero temperatures, the di-quark condensate constitutes

$$\begin{aligned} \langle\bar{q}q\rangle_0 &= -N_C \int \frac{\mathrm{d}^4p}{(2\pi)^4} \operatorname{tr}_D(S(p)) \\ &= -4\,N_C \int \frac{\mathrm{d}^4p}{(2\pi)^4} \frac{B(p^2)}{p^2A^2(p^2)+B^2(p^2)} \end{aligned} \tag{4.1.2}$$

with the index 0 indicating zero temperature. The factor N_C denotes the number of considered colors and is a result of the color trace, since all colors contribute equally. Here, $N_C \stackrel{!}{=} 3$. The simplification from line one to line two uses the γ matrices to be traceless

[1] Equation (4.1.1) already includes the renormalization constants to be one, which was a result in Sec. 2.3.

and the trace of the identity matrix to give the number of space-time dimensions. At non-zero temperatures the momentum integration separates to the integration over the spatial momentum and the summation over the Matsubara frequencies. Consequently, the finite temperature condensate reads

$$\begin{aligned} \langle\bar{q}q\rangle_T &= -N_C\,T\sum_{n=-\infty}^{\infty}\int\frac{\mathrm{d}^3p}{(2\pi)^3}\,\mathrm{tr}(S(\boldsymbol{p},\omega_n)) \\ &= -4\,N_C\,T\sum_{n=-\infty}^{\infty}\int\frac{\mathrm{d}^3p}{(2\pi)^3}\frac{B(\boldsymbol{p}^2,\omega_n)}{\boldsymbol{p}^2A^2(\boldsymbol{p}^2,\omega_n)+{\omega_n}^2C^2(\boldsymbol{p}^2,\omega_n)+B^2(\boldsymbol{p}^2,\omega_n)} \end{aligned} \tag{4.1.3}$$

with the subscript T indicating non-zero temperature. The numerical treatment of the integration and summation in Eqs. (4.1.2) and (4.1.3) goes along with that introduced in Secs. 3.1 and 3.2.1.

Recalling the bare values of the dressing functions (cf. Sec. 3.2.2)

$$A_{\mathrm{bare}}=1,\quad C_{\mathrm{bare}}=1,\quad B_{\mathrm{bare}}=m \tag{4.1.4}$$

the quark condensate, Eq. (4.1.1), turns out to be quadratically divergent for non-zero current quark masses $m\neq 0$. Separating B into the bare contribution m and that of dynamical chiral symmetry breaking

$$B_{\mathrm{DCSB}}(p^2) := B(p^2)-m \tag{4.1.5}$$

the vacuum condensate has the form

$$\langle\bar{q}q\rangle_0 = -4\,N_C\int\frac{\mathrm{d}^4p}{(2\pi)^4}\frac{B_{\mathrm{DCSB}}(p^2)+m}{p^2A^2(p^2)+B^2(p^2)}. \tag{4.1.6}$$

Assuming the effect of DCSB to vanish sufficiently fast for large momenta, which is illustrated by Fig. 4.1.1a, the divergent contribution to the condensate can be separated,

$$\langle\bar{q}q\rangle_0 = \langle\bar{q}q\rangle_{0,\mathrm{DCSB}} - 4\,N_C\int\frac{\mathrm{d}^4p}{(2\pi)^4}\frac{m}{p^2A^2(p^2)+B^2(p^2)}, \tag{4.1.7}$$

where

$$\langle\bar{q}q\rangle_{0,\mathrm{DCSB}} := -4\,N_C\int\frac{\mathrm{d}^4p}{(2\pi)^4}\frac{B_{\mathrm{DCSB}}(p^2)}{p^2A^2(p^2)+B^2(p^2)}. \tag{4.1.8}$$

Taking into account the results of Sec. 3.1, namely $\lim_{p\to\infty}A=1$ and $\lim_{p\to\infty}B=m$ for the NG solution, the divergence $\Delta(\Lambda)$ can be estimated like

$$\Delta(\Lambda) := \langle\bar{q}q\rangle_{0,\mathrm{DCSB}} - \langle\bar{q}q\rangle_0 \tag{4.1.9}$$

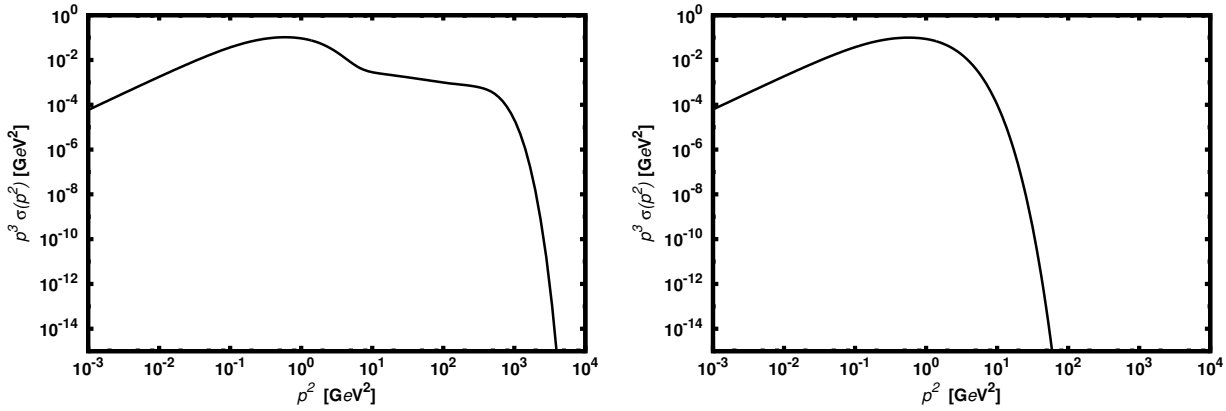

(a) Massive case, $m = 5\,\mathrm{MeV}$. **(b)** Chiral limit, $m = 0$.

Figure 4.1.1: Behaviour of the integrand in $\langle\bar{q}q\rangle_{0,\mathrm{DCSB}}$ for $m = 5\,\mathrm{MeV}$ and for the chiral limit: $\sigma(p^2) := B_{\mathrm{DCSB}}(p^2)(p^2A^2(p^2) + B^2(p^2))^{-1}$.

$$\begin{aligned} &= 4\,N_C \int^{\Lambda} \frac{\mathrm{d}^4p}{(2\pi)^4} \frac{m}{p^2A^2(p^2) + B^2(p^2)} \\ &\approx K' \int^{\Lambda} \mathrm{d}p \frac{p^3 m}{p^2 + m^2} \\ &\approx K\Lambda^2 m \end{aligned}$$

where K' and K absorb respective factors. The upper integration limit Λ is introduced to show the quadratic divergence explicitly. The limit $\Lambda \to \infty$ corresponds to the integration in Eq. (4.1.2).

In the chiral limit, $m = 0$, the quark condensate is finite. Thus, the distinction between the chiral limit ($m = 0$) and the case of non-zero quark masses introduces a criterion for the quark condensate to be finite or divergent. For $m = 0$ the quark condensate is referred to as chiral condensate. To fix the divergence in the case $m \neq 0$ this thesis considers the renormalized condensate, which is also referred to as subtracted condensate.

4.1.1 Chiral limit

This subsection presents the chiral phase transition at $m = 0$. Additionally, the influence of the interaction strength D and the interaction range ω of the phenomenological gluon dressing, Eq. (2.5.16), is discussed.

First, the qualification of $B(0, \omega_0)$ as an order parameter for the chiral phase transition as argued in [Bla10, Fis09b] is presented [2]. Assuming the chiral condensate to be an order parameter of the chiral phase transition, i.e. vanishing of $\langle\bar{q}q\rangle$ in the chiral symmetric

[2] At $T = 0$, the respective discussion for $B(0)$ resembles that of $B(0, \omega_0)$.

phase and non-vanishing of $\langle\bar{q}q\rangle$ in the phase of spontaneously broken chiral symmetry, the scalar dressing function B evaluated at $(\boldsymbol{p}^2, \omega_n) = (0, \omega_0)$ is an order parameter for chiral symmetry. Proving this statement, the crucial arguments are (semi-) positiveness of B on its full domain and $(\boldsymbol{p}^2, \omega_n) = (0, \omega_0)$ to be the position of the global maximum of B.

At least for the model considered within the thesis at hand, B can not acquire non-zero values, since the integrand of the integral equation for B is positive (cf. Eqs. (2.5.13) and (2.5.16)). To avoid circle reasoning one has to assume positive semi-definite initial values for the iteration of the integral equation for B. The global maximum of B to be at $\boldsymbol{p}^2 = 0$ follows also by induction assuming constant initial values. To relax the condition of positive semi-definite initial values for B or constant initial values for all dressing functions regard the discussion on initial values in App. D.

"$\Leftarrow$": Since B is positive semi-definite, for the chiral condensate to be zero the integration and summation in Eq. (4.1.3) requires $B(0, \omega_0)$ to be zero.

"$\Rightarrow$": Since B is positive semi-definite and has a global maximum at $(0, \omega_0)$, vanishing of $B(0, \omega_0)$ implicates vanishing of B on its full domain. Consequently, summation and integration in Eq. (4.1.3) yields the chiral condensate to be zero.

A comparison of the following results with that given in Sec. 3.2.4, where the temperature dependence of the quark dressing is presented, confirms the above considerations.

Figure 4.1.2a shows the temperature dependence of the normalized chiral condensate $\langle\bar{q}q\rangle_T / \langle\bar{q}q\rangle_0$. Resembling the shape of $B(0, \omega_n)$ as given in Fig. 3.2.5 the curve remains almost constant for small temperatures and drops to zero with increasing slope. Taking into account the discussion of the temperature dependence of B along Fig. 3.2.5 the critical temperature reads

$$T_c = 132.6^{+0.2}_{-0.2}\,\mathrm{MeV}.$$

Thus, for temperatures higher than $T = 132.8\,\mathrm{MeV}$ the effect of dynamical chiral symmetry breaking does not occur. Unlike the temperature dependence of $B(0, \omega_n)$, $\langle\bar{q}q\rangle_T$ remains constant up to $T = 80\,\mathrm{MeV}$ and begins to decrease only at this temperature [3]. This observation supports the conjecture of Sec. 3.2.4, which considered the chiral symmetry restoration to start in this region. Furthermore, constant $\langle\bar{q}q\rangle_T$ along decreasing $B(0, \omega_n)$ reveals changing contributions of scalar dressing's domain to the chiral condensate. However, this might be an effect of the integral measure $T\sum\int \mathrm{d}p^3$, especially of the factor T.

Since $T_c = 132.6^{+0.2}_{-0.2}\,\mathrm{MeV}$ is a value rather non-typical for chiral symmetry restoration, Fig. 4.1.2b displays three variants of setting the interaction range ω and strength D in

[3] Actually, $\langle\bar{q}q\rangle_T$ rises slightly, for temperatures lower than $T = 80\,\mathrm{MeV}$. This phenomenon becomes more explicit in Fig. 4.1.2b.

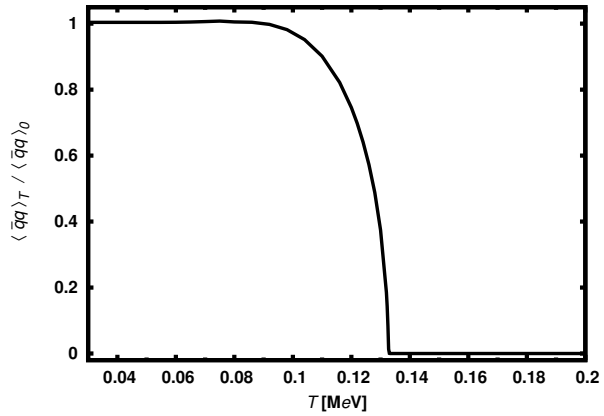

(a) Chiral symmetry restoration for $(D, \omega) = (1\,\mathrm{GeV}^2, 0.5\,\mathrm{GeV})$.

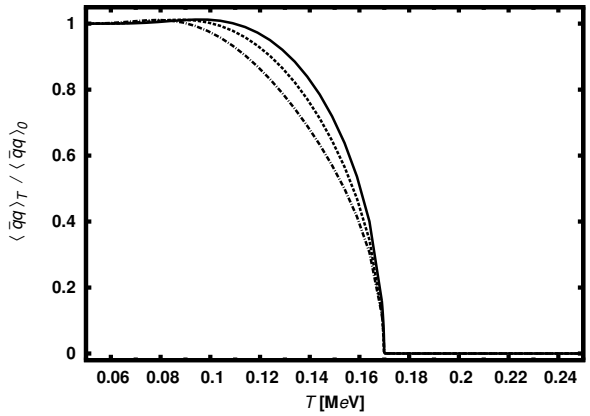

(b) Chiral symmetry restoration at $T = 170\,\mathrm{MeV}$ provided by different parameter sets. The line code is given in Tab. 4.1.1.

Figure 4.1.2: Temperature dependence of the chiral condensate $\langle \bar{q}q \rangle_T$ normalized to its vacuum value $\langle \bar{q}q \rangle_0$ for different parameter sets (D, ω) corresponding to those providing adequate predictions for observables (a) and those providing a typical value for the chiral phase transition (b).

$D[\mathrm{GeV}^2]$	1.445	1.285	1.087	1.000
$\omega[\mathrm{GeV}]$	0.50	0.45	0.4	0.50
$-\langle \bar{q}q \rangle_0^{1/3}[\mathrm{MeV}]$	286.1	265.6	241.5	251.1
(line code)	solid	dashed	dash-dotted	

Table 4.1.1: Parameter settings providing the critical temperature of chiral symmetry restoration at $T_c' = 170\,\mathrm{MeV}$ in comparison with the standard set (very right). The line code for Fig. 4.1.2b is added.

order to set the transition temperature to $T_c' = 170\,\mathrm{MeV}$, which corresponds to a value more common (cf. [Wei12]). Table 4.1.1 lists those settings and provides the vacuum values of the corresponding chiral condensates.

Taking into account the Gell-Mann–Oakes–Renner (GMOR) relation [Yag05, GM68]

$$f_\pi m_{\pi^0} \approx -\langle m_u \bar{u}u + m_d \bar{d}d \rangle_0 \tag{4.1.10}$$

with f_π denoting the pion decay constant, m_{π^0}, m_u, m_d being the masses of the neutral pion, the up quark and the down quark, respectively and $\bar{u}$, $\bar{d}$, u, d staying for the respective quark fields, these values reveal a discrepancy with hadron expectation values. Depending on the renormalization scale in vacuum, the chiral condensate has a value of [Rob94, Alk01, Yag05]

$$\langle \bar{q}q \rangle_0 \sim -(250\,\mathrm{MeV})^3.$$

The setting $(D, \omega) = (1.0\,\mathrm{GeV}^2, 0.5\,\mathrm{GeV})$ fits physical observables also via the chiral condensate (cf. the introduction of Ch. 3). From that point of view, the given settings do not meet the requirements given by the GMOR relation, Eq. (4.1.10). But since the values in Tab. 4.1.1 partly underestimate and partly overestimate the typical value of $\langle\bar{q}q\rangle_0 \sim -(250\,\mathrm{MeV})^3$, the existence of a setting which fits the GMOR relation and the requirement for a critical temperature $T_c = 170\,\mathrm{MeV}$ seems to be obvious. Appendix I presents the dependence of T_c on the parameters D and ω.

A readjustment of the parameters (D, ω) should include investigations of the hadron spectrum, e.g. using the BSE. Furthermore, the simple model applied in thesis may need sophistications to meet additional constraints such as a given critical temperature of chiral symmetry restoration. Those considerations exceed the scope of this thesis.

4.1.2 Nonzero quark masses

In the case of non-zero quark masses, the chiral symmetry is explicitly broken. But for light quark masses, $m_l \sim 5\,\mathrm{MeV}$, the chiral symmetry is assumed to be approximately established (cf. [Hil12, App. A]). In this sense, an investigation of chiral symmetry restoration for non-zero quark masses is reasonable.

As argued before quark condensate needs to be renormalized to fix the divergence originating from the quark mass m. For this purpose, this subsection considers the subtracted condensate $\Delta_{l,s}$ as an order parameter for chiral symmetry restoration. This quantity was proposed by [Che08] and is commonly used within the given context (cf. [Baz12, Fis13]). Its normalized form reads

$$\Delta_{l,s}(T) := \frac{\langle\bar{q}q\rangle_{l,T} - \frac{m_l}{m_s}\langle\bar{q}q\rangle_{s,T}}{\langle\bar{q}q\rangle_{l,0} - \frac{m_l}{m_s}\langle\bar{q}q\rangle_{s,0}} \tag{4.1.11}$$

where the subscripts l and s indicate the condensates to refer to those of light and strange quarks, respectively. Using the form of the quark condensate as given in Eq. (4.1.9) one has [4]

$$\begin{aligned} \langle\bar{q}q\rangle_l - \frac{m_l}{m_s}\langle\bar{q}q\rangle_s &\approx \langle\bar{q}q\rangle_{\mathrm{DCSB},l} - K\Lambda^2 m_l - \frac{m_l}{m_s}\left(\langle\bar{q}q\rangle_{\mathrm{DCSB},s} - K\Lambda^2 m_s\right) \\ &= \langle\bar{q}q\rangle_{\mathrm{DCSB},l} + \frac{m_l}{m_s}\langle\bar{q}q\rangle_{\mathrm{DCSB},s} \\ &\approx \langle\bar{q}q\rangle_{\mathrm{DCSB},l}. \end{aligned} \tag{4.1.12}$$

[4] The reasoning along Eq. (4.1.9) is extrapolated to arbitrary temperatures, which is why the subscript 0 (for $T = 0$) is omitted. The Matsubara formalism of non-zero temperatures involves a quadratic divergence, too. It has the form $\Delta_{\mathrm{M}}(\Lambda) = K_{\mathrm{M}} T\Lambda \sum_{-\infty}^{\infty} 1$ with K_{M} absorbing respective factors.

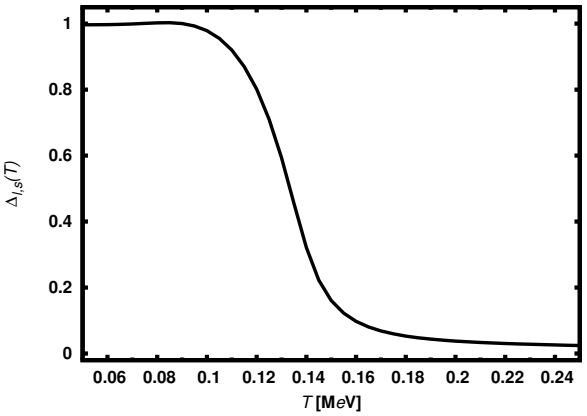

Figure 4.1.3: Temperature dependence of the normalized subtracted condensate for $m_s/m_l = 20$ and $m_l = 5\,\mathrm{MeV}$.

The last step assumes the contribution of DCSB to the strange quark condensate to be at the same order of magnitude as that of the light quark condensate, which leans on the discussion along Fig. 3.2.6 and that in [Hil12, Sec. 7.1.2]. For current quark masses ranging at $m_l \approx 5\,\mathrm{MeV}$ and $m_s \approx 100\,\mathrm{MeV}$ the second term of the second line in Eq. (4.1.12) is suppressed by $\approx 1/20$.

Figure 4.1.3 displays the temperature dependence of the subtracted condensate $\Delta_{l,s}$ for $m_l = 5\,\mathrm{MeV}$, $m_s = 100\,\mathrm{MeV}$ [5]. The behaviour of the subtracted condensate differs qualitatively from the behaviour of the chiral condensate. It lacks the characteristic kink indicating the transition temperature T_c. In the investigated region, the values of the subtracted condensate do not vanish at all. Regarding Eq. (4.1.12) this might result from the strange quark's contribution of DCSB $\langle \bar{q}q \rangle_{\mathrm{DCSB},s}$. This conjecture seems likely, since Sec. 3.2.5 already showed that for non-zero current quark masses m DCSB appears also at higher temperatures. Furthermore, this effect seemed to reach even higher temperatures for increasing mass m. Chapter 5 elaborates on this effect in some extend.

Disregarding the above discussion, especially accepting that the subtracted condensate does not vanish exactly, a pseudo-critical temperature $\tilde{T}_c$ can be defined as the position of the inflection point of the curve $\Delta_{l,s}(T)$

$$0 =: \left.\frac{\partial^2 \Delta_{l,s}(T)}{\partial T^2}\right|_{T=\tilde{T}_c}, \tag{4.1.13}$$

which corresponds to the peak position of the first derivative $\partial \Delta_{l,s}(T)/\partial T$. Thus, the

[5] The divergences in Eq. (4.1.11) are numerically treated by the truncation of the summation over the Matsubara frequencies (cf. Tab. 3.2.1) and a quasi cut-off, which enters the calculations when discretizing the momentum integration (cf. Eq. (3.2.1)).

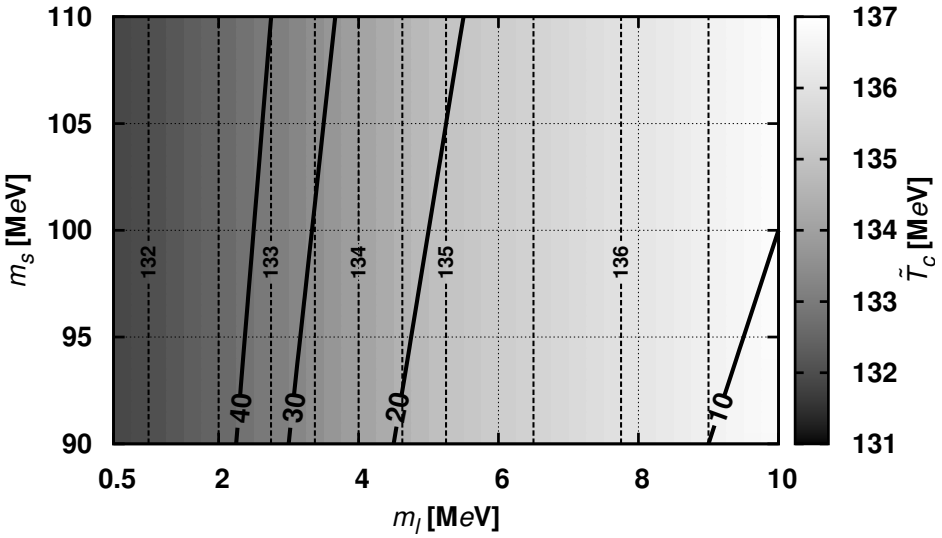

Figure 4.1.4: The critical temperature $\tilde{T}_c$ in dependency on the light quark mass m_l and the strange quark mass m_s. Thin dashed lines represent isotherms which are separated by 0.5 Me V. The labels are given in [MeV] every second line. Along the bold lines, the ratio m_s/m_l is constant and has the labelled value.

settings of Fig. 4.1.3 leads to a pseudo critical temperature [6]

$$\tilde{T}_c = 134.8\,\mathrm{MeV}.$$

Compared to the critical temperature T_c in the chiral limit $\tilde{T}_c$ is only slightly elevated. This result is expected, anyway, since the migration from zero mass to non-zero masses should be continuous. Otherwise, the assumption of massless current quarks would be not appropriate for practical considerations.

Figure 4.1.4 presents the critical temperature $\tilde{T}_c$ in dependency on the light quark mass m_l and the strange quark mass m_s scanning a neighbourhood of the values used in Fig. 4.1.3. Here, it ranges in $\tilde{T}_c \,/\, \mathrm{MeV} \in [131.9,\, 137.0]$. The behaviour along the m_l axis reveals the raising of the critical temperature for increasing current quark mass, which was suggested already in Sec. 3.2.5. Along the m_s axis $\tilde{T}_c$ remains constant. With regard to the correction

[6] To extract the position of the first derivative's peak the numerical data (41 numerical data points) has been interpolated using cubic splines, which provides a quasi functional relation between the subtracted condensate and the temperature, i.e. a polynomial of degree three, and therefore access to the derivative. Such routine is *splev* contained in the *scipy.interpolate* package. The interval $T \,/\, \mathrm{MeV} \in [50,\, 250]$ was interpolated using a mesh of 2000 points leading to a pseudo precision $\Delta T = 0.1\,\mathrm{MeV}$.

term $m_l/m_s\langle\bar{q}q\rangle_{\mathrm{DCSB},s}$ in Eq. (4.1.12) this should be a direct consequence of changing the strange mass only by $(\Delta m_s)/m_s \leq 10\%$. The influence of the fraction m_l/m_s in Eq. (4.1.12) can be omitted by investigating along lines of constant ratio between light quark mass and strange quark mass. Since Fig. 4.1.4 has limited scope the reasoning is vague. Along constant m_s/m_l, the critical temperature varies only in a small range. This indicates $\langle\bar{q}q\rangle_{\mathrm{DCSB},s}$ to have a minor influence on the transition temperature.

4.2 Dual condensate

This section elaborates on the possibility to investigate the model in terms of confinement. Confinement denotes the phenomenon of isolated color charges not been ever observed. However, the transition from confinement to phases of liberated color degrees of freedom is referred to as deconfinement (cf. [Yag05, Kap06] for an introduction to confinement and deconfinement). Following [Fis09a] the dual condensate Σ_n ($n \in \mathbb{Z}$) constitutes an order parameter for the deconfinement transition.

Originally, within the context of lattice QCD, the dual condensate is considered as an order parameter for center symmetry [Bil08]. The investigation of the center symmetry is motivated by understanding deconfinement as spontaneous breaking of the center symmetry [McL81], which is a result in pure gauge theory [7]. A discussion of confinement and potential characterizations is beyond the scope of this thesis. Consequently, only a selection of aspects concerning the dual condensate will be touched. All considerations use the chiral limit ($m = 0$).

4.2.1 Definition and properties

The dual condensate bases on the generalization of the anti-periodic boundary conditions of the quark fields (cf. Eq. (2.5.3)) to U(1)-valued boundary conditions

$$\psi(\boldsymbol{x}, 1/T) = e^{i\varphi}\psi(\boldsymbol{x}, 0) \tag{4.2.1}$$

with $\varphi \in [0, 2\pi)$. As a consequence the Matsubara frequencies are altered to be phase dependent quantities

$$\omega_n(\varphi) = \pi T(2n + \varphi/\pi) \tag{4.2.2}$$

[7] Pure gauge theory refers to a gauge theory not containing fermions [Yag05, Ch. 3]. See [Bil08] for relating the case of pure gauge to that of the quenched approximation (cf. Sec. 2.2 w.r.t. the quenched approximation).

and thus, the quark propagator is also dependent on φ

$$S^{-1}(\boldsymbol{p},\omega_n(\varphi)) = i\,\boldsymbol{\gamma p} A(\boldsymbol{p},\omega_n(\varphi)) + i\,\gamma\omega_n(\varphi) C(\boldsymbol{p},\omega_n(\varphi)) + B(\boldsymbol{p},\omega_n(\varphi)). \tag{4.2.3}$$

Using Eq. (4.1.3) the *ordinary* quark condensate becomes phase dependent, too,

$$\langle\bar{q}q\rangle_T(\varphi) \;=\; -N_C\,T\sum_{n=-\infty}^{\infty}\int\frac{\mathrm{d}^3p}{(2\pi)^3}\,\mathrm{tr}(S(\boldsymbol{p},\omega_n(\varphi))). \tag{4.2.4}$$

The definition of the dual condensate eventually reads

$$\Sigma_n \equiv \Sigma(n) := \int_0^{2\pi}\frac{\mathrm{d}\varphi}{2\pi} e^{-i\,\varphi n}\langle\bar{q}q\rangle_T(\varphi). \tag{4.2.5}$$

Note that this quantity acquires no imaginary part. This follows from the phase dependent condensate to be an even function w.r.t. $\varphi = \pi$

$$\langle\bar{q}q\rangle_T(\pi+\vartheta) = \langle\bar{q}q\rangle_T(\pi-\vartheta) \tag{4.2.6}$$

with $\varphi \in (0,\,\pi)$ [8]. Thus, using Euler's formula, $e^{i\varphi} = \cos\varphi + i\sin\varphi$, the dual condensate can be rewritten as

$$\Sigma_n = \int_0^{2\pi}\frac{\mathrm{d}\varphi}{2\pi}\cos(\varphi n)\langle\bar{q}q\rangle_T(\varphi). \tag{4.2.7}$$

The crucial property of the dual condensate is its behaviour under center transformation, i.e. under those gauge transformations $U(k)$ constituting the center $\mathrm{Z}(N_C)$ of the gauge group $\mathrm{SU}(N_C)$. The elements of $\mathrm{Z}(N_C)$ acting on the quark fields have the form $z(k) := e^{i\,2\pi k/N_C}$. A center transformation

$$U(k) : q(\boldsymbol{x},t) \mapsto z(k)q(\boldsymbol{x},t) = e^{i\,2\pi k/N_C}q(\boldsymbol{x},t) \tag{4.2.8}$$

with $k = 0, 1, \ldots N_C - 1$ introduces a phase shift $\Delta\varphi = 2\pi k/N_C$ to the phase dependent quark condensate (cf. Eqs. (4.2.1) and (4.2.2)), which leads to the transformation behaviour of the dual condensate

$$U(k) : \Sigma_n \mapsto {}^{z(k)}\Sigma_n = z(k)^n\Sigma_n. \tag{4.2.9}$$

This is a consequence of the 2π-periodicity of the phase dependent quark condensate (cf. App. E).

In the following, the particular case $n = 1$ is investigated. Here, the dual condensate Σ_1 transforms like the Polyakov line which is an order parameter of center symmetry [Yag05,

[8] Appendix E documents necessary properties of the phase dependent condensate.

Ch. 5.7]. This supports the consideration of Σ_1 as an order parameter of center symmetry. Applying a center transformation, examination of Eq. (4.2.9) reveals the dual condensate to remain constant if its value is zero. Consequently, vanishing dual condensate may indicate center symmetry of the system, and finite values of the dual condensate may indicate center symmetry to be absent.

4.2.2 Temperature dependence

For the numerical evaluation of Eq. (4.2.5) the quark DSE has to be solved dependently on the phase φ [9]. For convenience, the range of φ is represented by using a linear mapping

$$\varphi = \pi(x+1), \quad \mathrm{d}\varphi = \pi \mathrm{d}x, \quad x \in [-1,\, 1]. \tag{4.2.10}$$

Iteration of the quark Dyson-Schwinger equation at shifted Matsubara frequencies

$$\omega_n(\varphi(x_i)) = \pi T \left(2n + \frac{\pi(x_i+1)}{\pi} \right), \quad i = 1, 2, \ldots n^{\mathrm{le}} \tag{4.2.11}$$

with $x_1, \ldots, x_{n^{\mathrm{le}}}$ denoting the nodes of Gauss-Legendre approximation enables to use the numerical methods developed in Secs. 3.1 and 3.2.1. The corresponding form of the approximated dual condensate reads

$$\Sigma_1 \approx \sum_{i=1}^{n^{\mathrm{le}}} \frac{\pi \alpha_i}{2\pi} e^{-i\,\pi x_i} \langle \bar{q} q \rangle_T (\varphi(x_i)) \tag{4.2.12}$$

with α_i denoting the weights of the Gauss-Legendre quadrature. Figure 4.2.1 displays the temperature dependence of the dual condensate. For low temperatures its value remains zero. At about $T = 60\,\mathrm{M}e\mathrm{V}$ it begins to rise with increasing slope. After passing the inflection point at $T \approx 130\,\mathrm{M}e\mathrm{V}$, the slope decreases and remains almost constant at temperatures higher than $T = 150\,\mathrm{M}e\mathrm{V}$. With regard to the discussion in the last subsection, this behaviour indicates breaking of the center symmetry and therefore deconfinement. Using the position of the inflection point as a definition for the critical temperature

$$0 =: \left. \frac{\partial^2 \Sigma(T)}{\partial T^2} \right|_{T=T_c^{\mathrm{dec}}} \tag{4.2.13}$$

[9] One may think about the possibility of continuing the solution of the quark DSE, Eq. (2.5.13), that was obtained for the discrete set of Matsubara frequencies $\{\omega_n\}_{n\in\mathbb{Z}}$. Such a procedure can be derived from the discussion in App. C.3. At higher temperatures, this approach is ruled out by chiral symmetry restoration, which makes the scalar dressing function B to vanish (cf. Sec. 4.1.1). Continuation in the manner of App. C.3 would only provide trivial $B(\boldsymbol{p}, \omega_n(\varphi)$ and therefore zero condensate $\langle \bar{q} q \rangle_T(\varphi)$ and zero dual condensate Σ_n. Nevertheless, at temperatures sufficiently low, the procedure works.

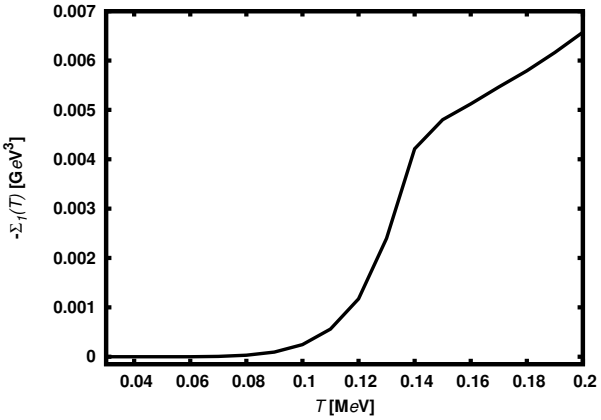

Figure 4.2.1: The dual condensate in dependency on the temperature.

the numerical data yield [10]

$$T_c^{\mathrm{dec}} = 133.7\,\mathrm{MeV}.$$

This temperature resembles the critical temperatures $T_c^{\chi} = 132.6\,\mathrm{MeV}$ and $\tilde{T}_c^{\chi} = 134.8\,\mathrm{MeV}$ of the chiral symmetry restoration in case of zero and non-zero current-quark mass, respectively [11]. This supports the results of [Fis09b], where the critical temperatures obtained by the slopes of the dual and chiral condensates are found to differ within $\Delta T \approx 1\,\mathrm{MeV}$ using a more elaborate model [12]. This may indicate that the suggested relation of chiral symmetry restoration and deconfinement is inherent in the structure of the quark DSE. Details of the theory's vertices and propagators may not be crucial for an approach to such relation.

4.3 Dispersion relation

This section presents an approach to the dispersion relation of quarks with current-quark mass zero in the chirally symmetric phase, i.e. $T > T_c$. The main challenge is to migrate from Euclidean space to Minkowski space. One possibility consists in using the spectral representation of the quark propagator and making an appropriate ansatz for the spectral density, whose parameters are fitted to the data at hand. In the following, this way is outlined basing on [Mue10]. Appendix G presents some necessary algebraic manipulations.

[10] To extract the inflection point of $\Sigma_1(T)$ the same procedure has been used as in Sec. 4.1.2.

[11] The critical temperature $\tilde{T}_c^{\chi}$ of chiral symmetry restoration in the massive case may be argued to be more appropriate for a comparison with T_c^{dec} of the deconfinement transition. Both $\tilde{T}_c^{\chi}$ and T_c^{dec} are extracted by using interpolation, while T_c^{χ} of chiral symmetry restoration is obtained directly from the drop of the chiral condensate.

[12] The model in [Fis09b] is beyond rainbow approximation and implements the transverse and longitudinal gluon dressings Δ_T and Δ_L to be different from each other.

The spectral representation of the quark propagator reads

$$S(\boldsymbol{p},\omega_n) \;=:\; \int_{-\infty}^{\infty} \frac{\mathrm{d}\omega'}{2\pi} \frac{\rho(\boldsymbol{p},\omega')}{i\omega_n - \omega'} \tag{4.3.1}$$

with $\rho(\boldsymbol{p},\omega')$ denoting the spectral density. For reasons of brevity, this outline skips discussing the details of the characteristic components of the spectral density and elaborates directly on the particular case of the chiral symmetric phase.

At temperatures higher than T_c the quark propagator has the form

$$S(\boldsymbol{p},\omega_n) \;= [i\boldsymbol{\gamma}\cdot\boldsymbol{p}A(\boldsymbol{p},\omega_n) + i\gamma_4\omega_n C(\boldsymbol{p},\omega_n)]^{-1} \tag{4.3.2}$$

or equivalently

$$S = S_-(\boldsymbol{p},\omega_n)P_-(\boldsymbol{p})\gamma_4 + S_+(\boldsymbol{p},\omega_n)P_+(\boldsymbol{p})\gamma_4 \tag{4.3.3}$$

with

$$P_\mp(\boldsymbol{p}) := \frac{1}{2}\left(1 \pm i\,\frac{\gamma_4\boldsymbol{\gamma}\boldsymbol{p}}{|\boldsymbol{p}|}\right) \tag{4.3.4}$$

and

$$S_\pm(\boldsymbol{p},\omega_n) := \frac{1}{\mp|\boldsymbol{p}|A + i\,\omega_n C}. \tag{4.3.5}$$

The indices of the projectors P_+ and P_- indicate the sign of the energy, which they project on. According to Eq. (4.3.1) the dressings S_+ and S_- have the spectral representation

$$S_\pm(\boldsymbol{p},\omega_n) =: \int_{-\infty}^{\infty} \frac{\mathrm{d}\omega'}{2\pi} \frac{\rho_\pm(\boldsymbol{p},\omega')}{i\omega_n - \omega'}. \tag{4.3.6}$$

Referring to the results in [Mue10, Kar09] the following ansatz [13,14] for the spectral density is reasonable

$$\rho_\pm(\boldsymbol{p},\omega) = 2\pi[Z_1\delta(\omega \mp E_1) + Z_2\delta(\omega \pm E_2)]. \tag{4.3.7}$$

The parameters E_1 and E_2 denote the δ-poles' positions and therefore refer to energies. The residua Z_1 and Z_2 are related to the possibility of each case (E_1 or E_2) to occur.

Using the ansatz given in Eq. (4.3.7) the quark propagator S is made up by four

[13] Evaluating the integral in Eq. (4.3.6) in terms of Cauchy's integral formula [Web04], i.e. using the S^{DSE} obtained from the quark DSE, should provide information about the actual spectral density. However, the methods used for solving the quark DSE in this thesis seem not to provide an appropriate access to the complex momentum plane (cf. Sec. 4.4)

[14] Cf. [Kar07].

contributions. Two of them have positive energies $+E_1$ and $+E_2$, and the other two have negative energies $-E_1$ and $-E_2$. Since both pairs of energies have the same absolute value by definition, one can concentrate on the positive ones. Equations (4.3.6) and (4.3.7) give the generic dressing

$$S_{\pm}^{\mathrm{tp}}(\boldsymbol{p},\omega_n) =: \int_{-\infty}^{\infty} \frac{\mathrm{d}\omega'}{2\pi} \frac{2\pi[Z_1\delta(\omega \mp E_1) + Z_2\delta(\omega \pm E_2)]}{i\omega_n - \omega'} \tag{4.3.8}$$

with the superscript (tp) pointing to the two-pole ansatz. To obtain 5-tupels (E_1, E_2, Z_1, Z_2, $\boldsymbol{p}$) containing the relations $E_1(\boldsymbol{p})$ and $E_2(\boldsymbol{p})$ the generic dressings S^{tp} can be fitted to the data resulting from the solution S^{DSE} of the quark DSE (cf. Eq. (4.3.5)) using

$$d_+(\boldsymbol{p}) \;:=\; \frac{1}{N+1} \sum_{n=0}^{N} \left| S_+^{\mathrm{tp}}(\boldsymbol{p},\omega_n) - S_+^{\mathrm{DSE}}(\boldsymbol{p},\omega_n) \right|^2 . \tag{4.3.9}$$

Figure 4.3.1 displays the dispersion relation $E_1(\boldsymbol{p})$ and $E_2(\boldsymbol{p})$ obtained by Eq. (4.3.9) for three different temperatures, $T/T_c = 1.5,\ 2.0,\ 2.5$. The critical temperature T_c was quantified in Sec. 4.1.1. The values are each normalized to the temperature T. The two branches are referred to as normal mode E_1 and (anti-) plasmino mode E_2 [15]. Compared to the results in [Mue10] the plasmino mode shows the characteristic minimum, known from the HTL approximation [Yag05]. For rising temperature its value shifts to lower spatial momenta $\boldsymbol{p}$ [16]. The existence of this minimum is related to the Van Hove singularities [Mus03]. Here, the lokal minimum causes a vanishing group velocity and therefore a divergence of certain production rates.

The plasmino branch does not enter the region of space-like momenta, which is contrast to the results of [Mue10]. There, Landau damping is argued as a reason for this feature. By considering the HTL continuum contribution in the fit ansatz for the spectral density the transition into the space-like region is disposed (at least for the two higher considered temperatures). Discussing on Fig. 4.3.1 the dispersion relation seems to be shifted globally to higher energies, c.f. $E_{1,2}/T$ at $\boldsymbol{p} = 0$, and thus, the transition to space-like region is avoided.

An unknown feature of the dispersion relation is that of a slight local minimum in the normal branch. This one appears for temperatures $T \gtrapprox 2\,T_c$. This effect should be given by the considered model. One argument for this proposal is the fact that the values of the dressing functions $A(0,\omega_0)$ and $C(0,\omega_0)$ intersect at $T \approx 2\,T_c$ (cf. Fig. 4.3.1c). To prove the proposal one may systematically investigate the influence of the model parameters D

[15] In Eq. (4.3.7), $\delta(\omega + E_2)$ corresponds to a contribution of a negative energy.
[16] For the consideration at hand, the minimum of the plasmino branch vanishes at $T \approx (2.32 \pm 0.02)T_c$.

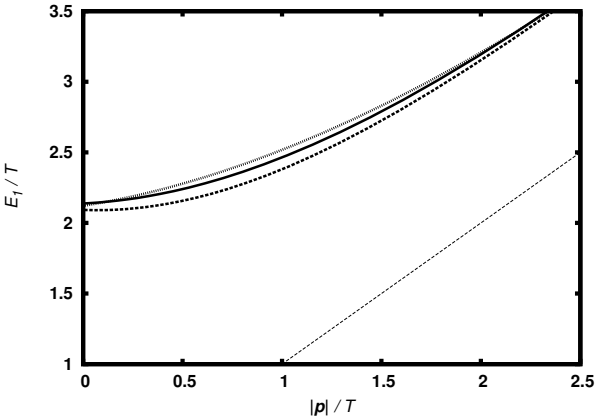

(a) Normal mode E_1.

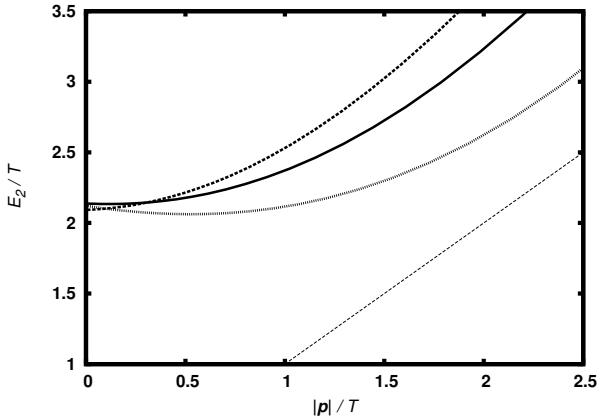

(b) Plasmino mode E_2.

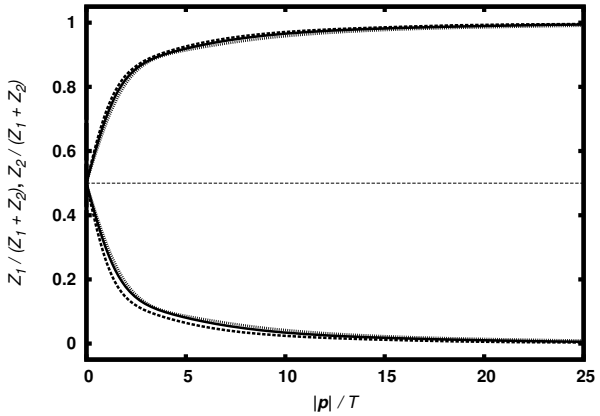

(c) Residua Z_1 and Z_2.

Figure 4.3.1: Dispersion relation of quarks obtained from d_+ in the chiral symmetric phase at three different temperatures: $T = 1.5\,T_c$ (dashed), $T = 2.0\,T_c$ (solid), $T = 2.5\,T_c$ (short-dashed). In subfigures (a) and (b), the light cone is represented by a thin dashed line.

and ω on the dispersion relation's shape and temperature dependence.

4.4 Pole structure

As shown in [Hil12] the quark propagator evaluated at complex momenta is of particular interest for solving the Bethe-Salpeter equation that provides access to the meson spectrum. In this context, the pole structure of the quark propagator is important to know. The existence of poles of the quark propagator in the complex momentum plane restricts the range of certain parameters when solving the Bethe-Salpeter equation. This section serves as an extension to the work done in [Hil12, Sec. 7.1.3] for the vacuum case and as a preparation of the systematic exploration of complex momentum range at non-zero temperatures.

4.4.1 Vacuum

Investigations on the quark propagator's pole structure in vacuum are available for different techniques [Mar92, Sta92, Bur98, Sou10]. This subsection uses direct continuation of the solution obtained along the real positive axis $p^2 \,/\, \mathrm{GeV}^2 \in (0\,\infty)$ to the complex plane $\mathbb{C}$. The continuation is carried out analogously to the procedure given in App. C.3.

Poles of the quark propagator

$$S(p) = \left[i\not{p} A(p^2) + B(p^2) \right]^{-1} \tag{4.4.1}$$

appear as roots of its denominator, i.e.

$$0 = p^2 A^2(p^2) + B^2(p^2). \tag{4.4.2}$$

Those roots are complex conjugated pairs [17], which is why consideration of the upper half of the complex plane suffices the investigation of the pole structure. Furthermore, investigation w.r.t. complex $\kappa := \sqrt{p^2}$ is more convenient, i.e. investigation of

$$f(\kappa) = 0 \tag{4.4.3}$$

for $f(\kappa) := \kappa A(\kappa^2) + i\, B(\kappa^2)$ [18]. Figure 4.4.1 shows this function in the neighbourhood of a root to illustrate the situation. Here, an arrow represents the value of f at κ with κ located at the back end of the arrow. One possibility to locate those roots uses the local minima of the absolute value of f. The function $|f|$ exhibits a local minimum for each root of f. Conversely, to check if a suspected minimum at $\tilde{\kappa}$ is a root of f one has to check, if both the real and the imaginary part of f change sign each for passing $\tilde{\kappa}$ parallel to the real and parallel to the imaginary axis (8 conditions).

A more elegant method uses the so-called "principle of argument" [Gon00]. Assuming the dressing functions to have no singularities, the number N of roots of f enclosed by the contour $\mathcal{C}$ is given by

$$N = \frac{1}{2\pi i} \oint_C \mathrm{d}\kappa \frac{f'(\kappa)}{f(\kappa)}. \tag{4.4.4}$$

After establishing $N = 1$ by choosing $\mathcal{C}$ appropriately systematic contraction of this contour

[17] Having a root $\tilde{p}^2$ Schwartz reflection principle [Web04] leads $(\tilde{p}^2)^*$ to be a root, too

$$(\tilde{p}^2)^* A^2((\tilde{p}^2)^*) + B^2((\tilde{p}^2)^*) = (\tilde{p}^2)^* (A^2(\tilde{p}^2))^* + (B^2(\tilde{p}^2))^* = 0^* = 0.$$

[18] The case $0 = \kappa A(\kappa^2) - i\, B(\kappa^2)$ corresponds to the lower complex plane of the p^2 consideration, Eq. (4.4.2), and is omitted therefore.

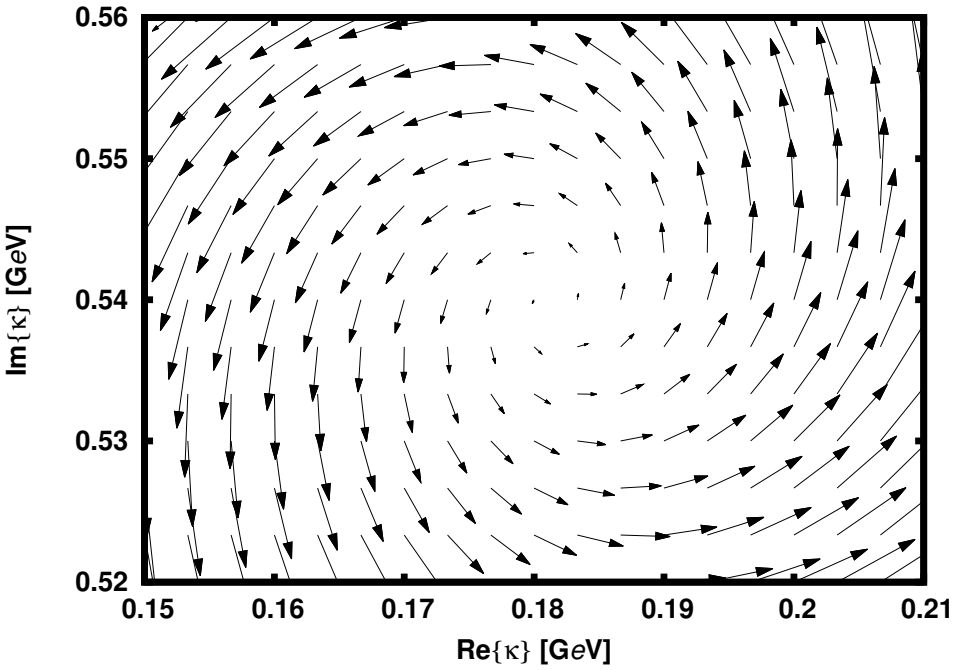

Figure 4.4.1: Function f for $m = 5\,\mathrm{MeV}$ in the neighbourhood of a root. The values $f(\kappa)$ are represented by arrows with their back end at κ: $\arg(f(\kappa))$ as angle w.r.t. the real axis and $|f(\kappa)|$ as length scaled by $0.2\,/\,\mathrm{GeV}$.

branch	$\kappa[\mathrm{GeV}]$	$p^2[\mathrm{GeV}^2]$
1	$0.177 + 0.527i$	$-0.250 + 0.176i$
2	$0.991 + 1.406i$	$-0.995 + 2.786i$
3	$1.335 + 1.817i$	$-1.521 + 4.851i$
4	$1.740 + 2.003i$	$-0.986 + 6.969i$

Table 4.4.1: Position of the complex poles in vacuum for $m = 0$.

determines the position of the enclosed root up to demanded precision.

Both methods find four roots of f in the upper complex momentum plane [19], whose positions are listed in Tab. 4.4.1 for the current quark mass $m = 0$. Increasing m shifts each root to higher momenta (absolute values). This effect is displayed in Fig. 4.4.2 for a quasi continuous scan from zero bare quark mass $m = 0$ to higher masses. The positions of the poles for light quarks and partly those of the strange and charm quarks are indicated as an orientation. Each branch starts at $m = 0$ [20]. The endings as given in Fig. 4.4.2 are unexpected. They rather reveal the limitation of the continuation procedure, which should

[19] The results presented in this subsection refer to investigation via the principle of argument, since for large quark masses the method using minima of $|f|$ turned out to be less stable than the other method.

[20] On the real axis, setting $m < 0$ leads to solutions with $B < 0$ (cf. Sec. 3.2.3). Consequently, this case corresponds to $0 = \kappa A(\kappa^2) - i\,B(\kappa^2)$. Thus, $m < 0$ give the same branches but reflected w.r.t. the real axis of the complex p^2 plane.

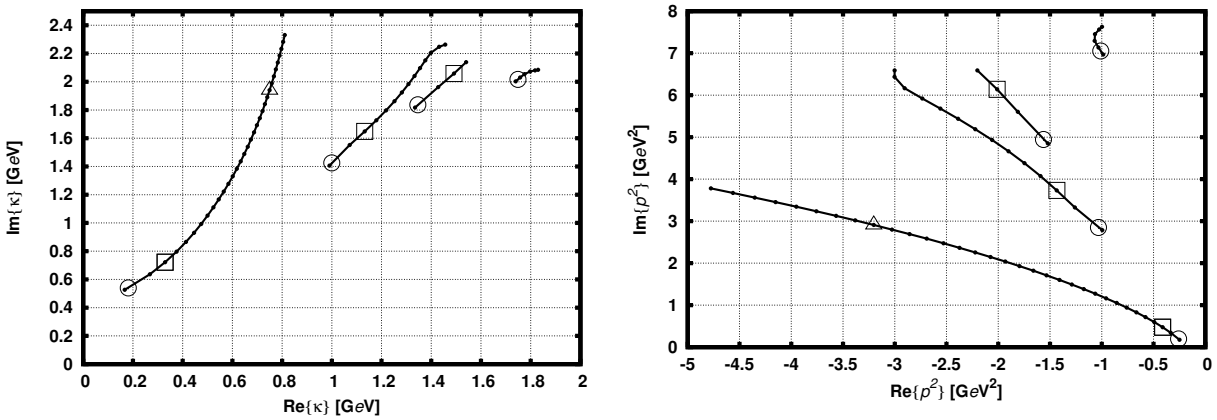

(a) Representation w.r.t. κ. **(b)** Representation w.r.t. p^2.

Figure 4.4.2: Positions of the quark propagator's poles for various current quark masses m. Variation of m generates four branches out of the four poles existing for a given value m. Moving along one branch dots indicate the progress every $\Delta m = 50\,\mathrm{MeV}$. Particular masses are indicated by the center of circles ($m = 5\,\mathrm{MeV}$), squares ($m = 100\,\mathrm{MeV}$), and triangles ($m = 1.2\,\mathrm{GeV}$).

be mainly influenced by the oscillations in the gluon dressing's exponential.

4.4.2 Non-zero temperatures

Analogously to the vacuum case the search for poles of the quark propagator

$$S(\boldsymbol{p}, \omega_n) = \left[i\,\boldsymbol{\gamma p} A(\boldsymbol{p}^2, \omega_n) + i\,\gamma_4 \omega_n C(\boldsymbol{p}^2, \omega_n) + B(\boldsymbol{p}^2, \omega_n) \right]^{-1} \tag{4.4.5}$$

corresponds to the search for roots of its denominator

$$0 = \boldsymbol{p}^2 A^2(\boldsymbol{p}^2, \omega_n) + \omega_n^2 C^2(\boldsymbol{p}^2, \omega_n) + B^2(\boldsymbol{p}^2, \omega_n). \tag{4.4.6}$$

Since the low temperature solutions resemble those of the vacuum case (cf. Sec. 3.3), poles are expected to be found in the same regions as displayed in Fig. 4.4.2, at least for low temperatures. However, complex squared momenta can be created in a twofold way, because the quark momentum consists of two distinguishable components, $p = (\boldsymbol{p}, \omega_n)$. Imaginary contributions γ may be added to the space-like (subscript s) momentum component

$$\kappa_{|\boldsymbol{p}|,s} := \sqrt{\boldsymbol{p}^2} + i\,\gamma_s \tag{4.4.7}$$

index	$\kappa_{\lvert\boldsymbol{p}\rvert,s}$[GeV]	$\boldsymbol{p}^2$[GeV^2]	$\boldsymbol{p}^2+\omega_0^2$[GeV^2]	$p^2(T=0)$[GeV^2]
1	$0.146+0.575i$	$-0.309+0.168i$	$-0.246+0.168i$	$-0.250+0.176i$
2	$0.975+1.413i$	$-1.044+2.756i$	$-0.981+2.756i$	$-0.995+2.786i$
3	$1.256+1.674i$	$-1.227+4.205i$	$-1.164+4.205i$	
4	$1.417+1.523i$	$-0.310+4.316i$	$-0.247+4.316i$	
5	$1.425+1.506i$	$-0.238+4.291i$	$-0.175+4.291i$	
6	$0.985+1.909i$	$-2.674+3.760i$	$-2.611+3.760i$	

Table 4.4.2: Positions of complex poles obtained for $\omega_{n,t}=\omega_0+0i$ at $(m,T)=(0,80\,\mathrm{MeV})$. For comparison, the vacuum positions are given for the first two poles.

or to the time-like (subscript t) momentum component [21]

$$\omega_{n,t} := \omega_n + i\,\gamma_t. \tag{4.4.8}$$

Both cases provide the possibility to continue the solution obtained on the real axis to complex values in the manner of App. C.3.

The function

$$g(\kappa_{|\boldsymbol{p}|,s},\omega_{n,t}) := \kappa_{|\boldsymbol{p}|,s}^2 A^2 + \omega_{n,t}^2 C^2 + B^2 \tag{4.4.9}$$

is the center of interest. For the determination of the poles' positions either $\kappa_{|\boldsymbol{p}|,s}$ or $\omega_{n,t}$ have to be kept constant while varying the respective other variable. A method using the minima of $|g|$ applies to both cases. The method using the principle of argument only applies to the case varying $\kappa_{|\boldsymbol{p}|,s}$, because a derivation of g w.r.t. $\omega_{n,t}$ is impossible, due to the discrete distribution of the Matsubara frequencies. However, the pole structure has three parameters. That is T and m and also γ_t or γ_s, respectively. This fact may imply a rich structure of the poles at non-zero temperatures.

A first attempt to quantify the pole structure is to use the principle of argument for $\kappa_{|\boldsymbol{p}|,s}$ and fixing the frequency like $\omega_{n,t}=\omega_0+0i$. For this configuration, Tab. 4.4.2 lists the positions of the poles with lowest absolute value $|\kappa_{|\boldsymbol{p}|,s}|$ at $(m,T)=(0,80\,\mathrm{MeV})$. More poles are expected at higher momenta. All those poles occur in quartets given via the inversions of the imaginary parts and the real parts. As a result of a scan to lower temperatures, those poles with the indices (1) and (2) belong to the poles of branch (1) and (2) given in Tab. 4.4.1.

As an example for the temperature dependence of a pole's position Fig. 4.4.2 displays a quasi continuous temperature shift from $T=0$ to $T=120\,\mathrm{MeV}$. In the κ- and in

[21] Note that $\omega_{n,t} := \omega_n + i\,\gamma_t$ corresponds to introducing a chemical potential (cf. [Cha07]).

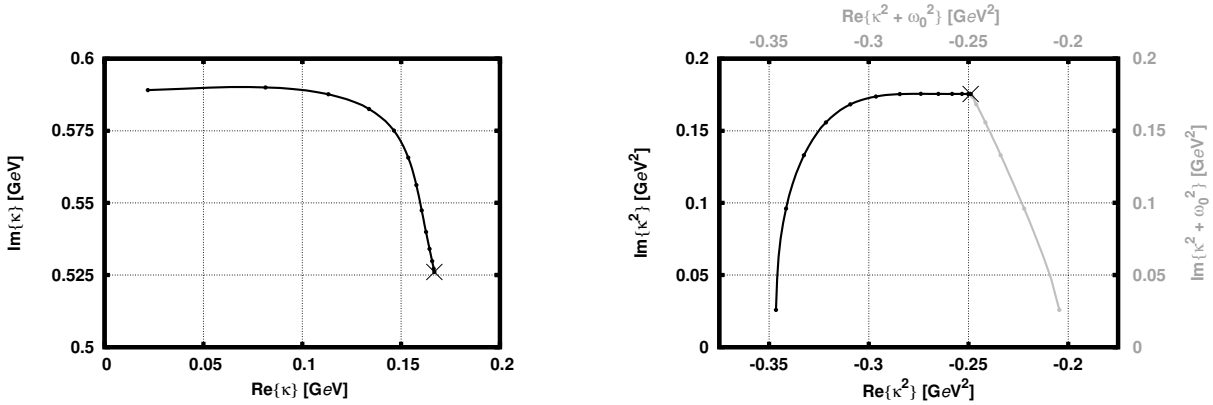

(a) Representation w.r.t. κ.

(b) Representation w.r.t. κ^2 (black) and $\kappa^2 + \omega_0^2$ (grey).

Figure 4.4.3: Temperature dependence of pole (1) given in Tab. 4.4.2 in the range $T/\mathrm{MeV} \in [0, 120]$. Dots indicate the position every 10 MeV starting from $T = 0$. The temperature $T = 0$ is marked additionally by a cross.

the κ^2-representation, the pole's position exhibits a considerable temperature dependence beginning right at $T = 0$. The influence increases at higher temperatures, which is indicated by the density of the dots.

Figure 4.4.3b displays the temperature dependence also in the $(\kappa^2 + \omega_0^2)$-representation, that is w.r.t. the full squared momentum p^2. There, the position remains constant for $T \lessapprox 60\,\mathrm{MeV}$ and only changes for higher temperatures. Such influence of the temperature is already known from the chiral condensate, whose value remained constant for low temperatures, cf. Sec. 4.1.1. Thus, the behaviour of the poles' positions may qualify for the characterization of some QCD phases. A proposal characterizing confinement in terms of having poles off the real momentum axis is given in [Rob12, Ch. 2.4]. But an investigation of a suspected physical meaning of the poles is beyond the scope of this thesis.

5 Summary and Outlook

This thesis presented the Dyson-Schwinger equation (DSE) for the quark propagator as a non-perturbative method for QCD. The introduction of non-zero temperatures provided access to the region along the temperature axis of the QCD phase diagram. The quark propagator can be used as input for the Bethe-Salpeter equation (BSE), which qualifies for investigating heavy-light mesons. Therefore, this thesis contributes to the complex of investigating in-medium modifications of D mesons, which are among the research programs of the collaborations CBM and PANDA at FAIR. The DSE/BSE approach needs to be checked carefully. For this reason a variety of experiences was presented.

The first part of the thesis defined the specific model that was to be investigated. Phenomenological input (the MT-like gluon dressing and the rainbow approximation) served for decoupling the exact quark DSE from the DSEs of the gluon propagator and the quark-gluon vertex. Three parameters (current quark mass, interaction range, interaction strength) were left to determine the eventual model. The interaction strength and the interaction range were set to values which are known to yield suitable results for hadron observables at zero temperature (vacuum).

The development of the numerical procedure mainly involved finding of a reasonable truncation of the infinite summation over the Matsubara frequencies. Direct iteration was chosen for solving the coupled set of integral equations for the decomposed quark propagator. After presenting the three known classes of solutions (NG, WW, inverse NG), further investigations focussed on the NG class. The case of zero temperature has always been used as a benchmark.

One crucial aspect of investigating finite temperatures is chiral symmetry restoration signalled by vanishing of the chiral condensate at the critical temperature T_c. In the case of light quark masses, the subtracted condensate maintains the renormalization of the divergent di-quark condensate and serves for investigating the chiral symmetry restoration. The inflection point of its temperature dependence served for defining the critical temperature $\tilde{T}_c$. Another quantity available from the quark DSE is the dual condensate. Following [Fis09a] it has been considered as measure for deconfinement. The inflection point was used to extract the critical temperature T_c^{dec}.

When extracting the dispersion relation of quarks from the quark propagator, the main challenge is the transformation of the numerical data obtained in Euclidean-space formalism to Minkowski space. For this purpose, the quark propagator was rewritten in spectral representation using a two-pole ansatz for the spectral density [Mue10, Kar09]. This trail function qualified for a fit to the numerical data obtained from the quark DSE, which consequently, yielded a dispersion relation exhibiting two branches. The minimum of the so-called plasmino branch corresponds to a divergence of certain production rates, which is interrelated with the occurrence of Van Hove singularities. While the plasmino minimum vanishes at higher temperatures, the so-called normal branch forms a local minimum for temperatures $T \gtrapprox 2T_c$, which was clearly unexpected and needs to be explained.

The investigation of complex quark momenta revealed limitations for using the quark propagator as input for the BSE. That is, the existence of complex poles restricts the choice of possible reference frames with respect to the meson. In addition to the work done in [Hil12], the situation of increasing current quark mass was clarified for the vacuum case. The method of numeric continuation into the complex plane worked properly for small imaginary parts of the momentum. Leaving the vacuum case, complex momenta are available in two different ways. This prospects a rich variety of the pole structure. A first investigation found multiple poles, whose positions depend on the temperature. This work has to be expanded for future applications of the quark propagator.

Elaborating on the results of in more detail the extracted critical temperatures range around $T_c = 133\,\mathrm{MeV}$, which is too low according to present lattice QCD thermodynamics. A readjustment of the model parameters to a more compatible value $T_c = 170\,\mathrm{MeV}$ would introduce tensions with certain hadron observables, which could be quantified especially by the BSE. Therefore, the model can be characterized to base on too stringent simplifications in the truncation scheme. This may also cause the existence of the unexpected local minimum of the dispersion relation's normal branch.

Future studies will have to modify the approximations applied to the full DSEs to provide a consistent parametrization of the interaction. Those considerations cover the extension of the gluon kernel and probably sophistications of the quark-gluon vertex. Albeit these perspectives, the introduced and tested model qualifies to serve as in input for investigating temperature effects on the hadron spectrum, e.g. by the Bethe-Salpeter equation. Thereby, the obligatory systematic investigation of the quark propagator's pole structure may reveal a new perspective on phase transitions. That is, the dependence of the poles on the temperature and possibly other thermodynamic parameters may posses a certain physical meaning.

To cope with the programs of CBM and PANDA at FAIR in future investigations, also

the chemical potential needs to be considered. This extension will provide full access to the QCD phase diagram. Thus, the approach using the Dyson-Schwinger and Bethe-Salpeter equations enters a large area of physical research questions. Those steps are beyond the scope of this thesis and call for separate studies. But they also require preparatory work such as presented in the last five chapters.

A Derivation of the Dyson-Schwinger equation for the quark propagator

This appendix adds some details to the main steps of the derivation of the quark DSE outlined in Sec. 2.1 to enable a better understanding of this equation.

The derivation of the quark DSE is shown right in Euclidean space [1]. Note that Euclidean space does not need to distinguish between upper and lower indices (cf. Appendix B). Furthermore, color space does not, either. Therefore, the summation convention is defined by summing twice appearing same Lorentz indices (μ, ν, ...) and Gell-Mann indices (a, b, ...) over all available values. This convention is used throughout the thesis if not explicitly indicated differently.

In Euclidean space, the action functional of unrenormalized QCD and that of the corresponding sources read [Rob00, Ch. 2.1]

$$\begin{aligned} S_{QCD}\left[q,\bar{q},\omega,\bar{\omega},B\right] \;:=\; \int \mathrm{d}^4x \Bigg\{ & \sum_{f=1}^{N_f} \bar{q}_f \left(\gamma_\mu\partial_\mu + m_f + i\,g t^a \gamma_\mu B_\mu^a\right) q_f \\ & + \frac{1}{4} F_{\mu\nu}^a F_{\mu\nu}^a \\ & + \frac{1}{2\xi}(\partial_\mu B_\mu^a)(\partial_\nu B_\nu^a) \\ & - \left[\partial_\mu\bar{\omega}^a\partial_\mu\omega^a + g f^{abc}\partial_\mu\bar{\omega}^a\omega^b B_\mu^c\right] \Bigg\} \end{aligned} \tag{A.1}$$

and

$$\begin{aligned} S_{source}\left[q,\bar{q},\omega,\bar{\omega},B,\bar{\xi},\xi,\bar{\eta},\eta,\lambda\right] \;:=\; \int \mathrm{d}^4x \Bigg\{ & \sum_{f=1}^{N_f} \bar{q}_f\xi_f + \bar{\xi}_f q_f + \lambda_\mu^a B_\mu^a \\ & + \bar{\eta}_a\omega_a + \bar{\omega}_a\eta_a \Bigg\}. \end{aligned} \tag{A.2}$$

[1] Deriving in Minkowski space and prescribing the terms to the Euclidean space afterwards may not result in solutions related to Minkowski space solutions in terms of analytical continuation, cf. [Rob00, p. 6].

These give the generating functional of QCD by

$$\mathcal{Z}\left[\bar{\xi},\xi,\bar{\eta},\eta,\lambda\right] := \int \mathcal{D}\mu\, e^{-S_{QCD}[q,\bar{q},\omega,\bar{\omega},B]+S_{source}\left[q,\bar{q},\omega,\bar{\omega},B,\bar{\xi},\xi,\bar{\eta},\eta,\lambda\right]}. \tag{A.3}$$

The expression $\mathcal{D}\mu = \mathcal{D}\mu(q,\bar{q},\omega,\bar{\omega},B)$ denotes the measure of the path integral, which reads more explicitly

$$\mathcal{D}\mu(q,\bar{q},\omega,\bar{\omega},B) := \prod_{x\in\mathbb{R}^4}\prod_{f=1}^{N_f}\prod_{\rho=1}^{N_C}\mathcal{D}\bar{q}_{f,\rho}(x)\mathcal{D}q_{f,\rho}(x)\prod_{a=1}^{N_C^2-1}\mathcal{D}\bar{\omega}^a(x)\mathcal{D}\omega^a(x)\prod_{\mu=1}^{4}\mathcal{D}B^a_\mu(x). \tag{A.4}$$

Using the generating functional of Euclidean QCD the quark propagator and the gluon propagator take the form [2]

$$\begin{aligned}
S(x-y) &:= \langle 0|Tq(x)\bar{q}(y)|0\rangle \\
&= \frac{\int \mathcal{D}\mu\, q(x)\bar{q}(y)e^{-S_{QCD}}}{\int \mathcal{D}\mu\, e^{S_{QCD}}} \\
&= \left.\frac{\int \mathcal{D}\mu\, q(x)\bar{q}(y)e^{-S_{QCD}+S_{Source}}}{\int \mathcal{D}\mu\, e^{-S_{QCD}+S_{Source}}}\right|_{\bar{\xi}=0,\,\xi=0,\,\bar{\eta}=0,\,\eta=0,\,\lambda=0} \\
&= \left.\frac{\frac{\delta}{\delta\bar{\xi}(x)}\frac{\delta}{\delta\xi(y)}\mathcal{Z}\left[\bar{\xi},\xi,\bar{\eta},\eta,\lambda\right]}{\mathcal{Z}\left[\bar{\xi},\xi,\bar{\eta},\eta,\lambda\right]}\right|_{\bar{\xi}=0,\,\xi=0,\,\bar{\eta}=0,\,\eta=0,\,\lambda=0} \\
&= \left.\frac{\delta}{\delta\bar{\xi}(x)}\frac{\delta}{\delta\xi(y)}\log\mathcal{Z}\left[\bar{\xi},\xi,\bar{\eta},\eta,\lambda\right]\right|_{\bar{\xi}=0,\,\xi=0,\,\bar{\eta}=0,\,\eta=0,\,\lambda=0},
\end{aligned} \tag{A.5}$$

$$\begin{aligned}
D^{ab}_{\mu\nu}(x-y) &:= \langle 0|TB^a_\mu(x)B^b_\nu(y)|0\rangle \\
&= \frac{\int \mathcal{D}\mu\, B^a_\mu(x)B^b_\nu(y)e^{-S_{QCD}}}{\int \mathcal{D}\mu\, e^{-S_{QCD}}} \\
&= \left.\frac{\delta}{\delta\lambda^a_\mu(x)}\frac{\delta}{\delta\lambda^b_\nu(y)}\log\mathcal{Z}\left[\bar{\xi},\xi,\bar{\eta},\eta,\lambda\right]\right|_{\bar{\xi}=0,\,\xi=0,\,\bar{\eta}=0,\,\eta=0,\,\lambda=0}.
\end{aligned} \tag{A.6}$$

The first step of the derivation is preparing an appropriate differential operator acting on the generating functional. For this purpose, consider the fact that the generating functional $\mathcal{Z}[\ldots]$ is independent of the QCD fields. In particular, for $\bar{q}(x)$ this leads to

$$\begin{aligned}
0 &= \frac{\delta\mathcal{Z}}{\delta\bar{q}(x)}\left[\bar{\xi},\xi,\bar{\eta},\eta,\lambda\right] \\
&= \int \mathcal{D}\mu\,\frac{\delta}{\delta\bar{q}(x)}e^{-S_{QCD}+S_{source}}
\end{aligned} \tag{A.7}$$

[2] Note that the path integral absorbs the time ordering $T(\ldots)$ (cf. [Das06, Sec. 4.2]).

$$
\begin{aligned}
&= \int \mathcal{D}\mu \left(-\frac{\delta S}{\delta \bar{q}(x)} \left[q, \bar{q}, \omega, \bar{\omega}, B \right] + \xi(x) \right) e^{-S_{QCD} + S_{source}} \\
&= \left(-\frac{\delta S}{\delta \bar{q}(x)} \left[\frac{\delta}{\delta \bar{\xi}}, \frac{\delta}{\delta \xi}, \frac{\delta}{\delta \bar{\eta}}, \frac{\delta}{\delta \eta}, \frac{\delta}{\delta \lambda} \right] + \xi(x) \right) \mathcal{Z} \left[\bar{\xi}, \xi, \bar{\eta}, \eta, \lambda \right].
\end{aligned}
$$

The notation of the operator $\delta/\delta\bar{q}(x)$ representing the functional derivative w.r.t. an (anti-) quark field omits both the color index and the flavour index. This is valid because all colors and flavours contribute equally and do not directly couple to one another. The last step uses the chain rule. Thus, within the braces of the last line, the first object is a functional differential operator acting on the generating functional $\mathcal{Z}[\ldots]$. The QCD fields in the $\delta/\delta\bar{q}\, S_{QCD}$ are prescribed to functional derivatives with respect to the corresponding sources [3]. Consequently, with

$$
\frac{\delta S}{\delta \bar{q}(x)} \left[q, \bar{q}, \omega, \bar{\omega}, B \right] = \left(\gamma_\mu \partial_\mu + m + i\, g t^a \gamma_\mu B^a_\mu(x) \right) q(x) \tag{A.8}
$$

this operator reads

$$
\frac{\delta S}{\delta \bar{q}(x)} \left[\frac{\delta}{\delta \bar{\xi}}, \frac{\delta}{\delta \xi}, \frac{\delta}{\delta \bar{\eta}}, \frac{\delta}{\delta \eta}, \frac{\delta}{\delta \lambda} \right] = \left(\gamma_\mu \partial_\mu + m + i\, g t^a \gamma_\mu \frac{\delta}{\delta \lambda^a_\mu(x)} \right) \frac{\delta}{\delta \bar{\xi}(x)}. \tag{A.9}
$$

Finally, Eq. (A.7) is attached by one more derivative by applying a further functional derivative w.r.t. the source $\xi(y)$ [4]

$$
0 = \left(-\left(\frac{\delta S}{\delta \bar{q}(x)} \left[\frac{\delta}{\delta \bar{\xi}}, \frac{\delta}{\delta \xi}, \frac{\delta}{\delta \bar{\eta}}, \frac{\delta}{\delta \eta}, \frac{\delta}{\delta \lambda} \right] \frac{\delta}{\delta \xi(y)} \right) + \delta(x-y) \right) \mathcal{Z}[\bar{\xi}, \xi, \bar{\eta}, \eta, \lambda]. \tag{A.10}
$$

Division by $\mathcal{Z}$ and application of the chain rule once more prepares the expressions for the identification of connected Greens functions at the end of the derivation,

$$
\begin{aligned}
0 &= -\frac{\left(\frac{\delta S}{\delta \bar{q}(x)} \left[\frac{\delta}{\delta \bar{\xi}}, \frac{\delta}{\delta \xi}, \frac{\delta}{\delta \bar{\eta}}, \frac{\delta}{\delta \eta}, \frac{\delta}{\delta \lambda} \right] \frac{\delta}{\delta \xi(y)} \right) \mathcal{Z} \left[\bar{\xi}, \xi, \bar{\eta}, \eta, \lambda \right]}{\mathcal{Z} \left[\bar{\xi}, \xi, \bar{\eta}, \eta, \lambda \right]} + \delta(x-y) \qquad \text{(A.11)} \\
&= -\left(\frac{\delta S}{\delta \bar{q}(x)} \left[\frac{\delta}{\delta \bar{\xi}}, \frac{\delta}{\delta \xi}, \frac{\delta}{\delta \bar{\eta}}, \frac{\delta}{\delta \eta}, \frac{\delta}{\delta \lambda} \right] \frac{\delta}{\delta \xi(y)} \right) \log \mathcal{Z} \left[\bar{\xi}, \xi, \bar{\eta}, \eta, \lambda \right] + \delta(x-y).
\end{aligned}
$$

Plugging Eq. (A.9) into Eq. (A.11) gives (arguments of $\mathcal{Z}$ suppressed)

$$
0 = -\left(\gamma_\mu \partial_\mu + m + i\, g t^a \gamma_\mu \frac{\delta}{\delta \lambda^a_\mu(x)} \right) \frac{\delta}{\delta \bar{\xi}(x)} \frac{\delta}{\delta \xi(y)} \log \mathcal{Z} + \delta(x-y) \tag{A.12}
$$

[3] These prescriptions read $q(x) \to \delta/\delta\bar{\xi}(x)$, $\bar{q}(x) \to \delta/\delta\xi(x)$, etc.

[4] The functional derivative $\delta/\delta\xi(y)$ acts from the right. Furthermore, the term $\xi(x)\delta\mathcal{Z}/\delta\xi(y)$ is omitted, because the following steps do not include further functional derivatives. In the limit of vanishing sources, $\xi(x)\delta/\delta(y)\,\mathcal{Z}$ gives zero.

$$
\begin{aligned}
&= -(\gamma_\mu \partial_\mu + m)\frac{\delta^2 \log \mathcal{Z}}{\delta\bar{\xi}(x)\delta\xi(y)} - i\,g t^a \gamma_\mu \frac{\delta^3 \log \mathcal{Z}}{\delta\lambda^a_\mu(x)\delta\bar{\xi}(x)\delta\xi(y)} + \delta(x-y) \\
&= -(\gamma_\mu \partial_\mu + m)\frac{\delta^2 \log \mathcal{Z}}{\delta\bar{\xi}(x)\delta\xi(y)} \\
&\quad -i\,g t^a \gamma_\mu \int \mathrm{d}^4 v \int \mathrm{d}^4 w \delta(v-x)\delta(w-x)\frac{\delta^3 \log \mathcal{Z}}{\delta\lambda^a_\mu(v)\delta\bar{\xi}(w)\delta\xi(y)} \\
&\quad +\delta(x-y).^5
\end{aligned}
$$

Analogously to Eq. (A.5), $\delta^3 \log \mathcal{Z}/\delta\lambda^a_\mu(v)\delta\bar{\xi}(w)\delta\xi(y)$ equals the connected 3-point function with two outer quark lines and one outer gluon line. Nevertheless, this very function can be expressed in terms of the one-particle irreducible (1PI) vertex function using the Legendre transformation of the QCD generating functional's logarithm $\log \mathcal{Z}$. After defining the Legendre transformation and deriving two crucial identities, the relation between the connected 3-point function of Eq. (A.12) and the 1PI vertex function is established.

The functional Legendre transformation of $\log Z$ (neglecting flavour, color, Gell-Mann and Lorentz indices) is defined as

$$
\begin{aligned}
&\Gamma\left[\frac{\delta \log \mathcal{Z}}{\delta\bar{\xi}}, \frac{\delta \log \mathcal{Z}}{\delta\xi}, \frac{\delta \log \mathcal{Z}}{\delta\lambda}, \frac{\delta \log \mathcal{Z}}{\delta\bar{\eta}}, \frac{\delta \log \mathcal{Z}}{\delta\eta}\right] := \\
&\int \mathrm{d}^4 x \left\{\bar{\xi}\frac{\delta \log \mathcal{Z}}{\delta\bar{\xi}} + \frac{\delta \log \mathcal{Z}}{\delta\xi}\xi + \lambda\frac{\delta \log \mathcal{Z}}{\delta\lambda} + \bar{\eta}\frac{\delta \log \mathcal{Z}}{\delta\bar{\eta}} + \frac{\delta \log \mathcal{Z}}{\delta\eta}\eta\right\} - \log \mathcal{Z}
\end{aligned}
\tag{A.13}
$$

and

$$
\Gamma[q, \bar{q}, \omega, \bar{\omega}, B] := \int \mathrm{d}^4 x \left\{\bar{\xi} q + \bar{q}\xi + \lambda B + \bar{\eta}\omega + \bar{\omega}\eta\right\} - \log \mathcal{Z}. \tag{A.14}
$$

The identifications connecting Eq. (A.13) and Eq. (A.14), e.g. $q(x) = \delta/\delta\bar{\xi}(x)$, are justified by

$$
\begin{aligned}
\langle 0|q(x)|0\rangle &= \frac{\int \mathcal{D}\mu\, q(x) e^{-S_{QCD}}}{\int \mathcal{D}\mu\, e^{-S_{QCD}}} \\
&= \left.\frac{\delta \log \mathcal{Z}}{\delta\bar{\xi}(x)}\right|_{\bar{\xi}=0,\,\xi=0,\,\bar{\eta}=0,\,\eta=0,\,\lambda=0} \\
&=: q_c(x)
\end{aligned}
\tag{A.15}
$$

(and analogously for the other field operators). The subscript c is neglected from now on [6].

[5] To allow for a clearly performed prescription of the threefold derivative the dependency w.r.t. the argument x is separated in this very function.

[6] The subscript c stands for "classical". See e.g. [Das06] for a discussion, whose notation explicitly distinguishes between the functions denoted by the subscript c and the corresponding field operators.

The functional $\Gamma[q, \bar{q}, \omega, \bar{\omega}, B]$ is referred to as effective action. From its definition follow three identities follow

$$\delta(w-u) = \frac{\delta\bar{\xi}(u)}{\delta\bar{\xi}(w)} = \int \mathrm{d}^4 s \frac{\delta\bar{\xi}(u)}{\delta\bar{q}(s)} \frac{\delta\bar{q}(s)}{\delta\bar{\xi}(w)} = \int \mathrm{d}^4 s \frac{\delta^2\Gamma}{\delta\bar{q}(s)\delta q(u)} \frac{\delta^2 \log \mathcal{Z}}{\delta\bar{\xi}(w)\delta\xi(s)}, \tag{A.16}$$

$$\delta(s-y) = \frac{\delta\bar{q}(y)}{\delta\bar{q}(s)} = \int \mathrm{d}^4 u \frac{\delta\bar{q}(y)}{\delta\bar{\xi}(u)} \frac{\delta\bar{\xi}(u)}{\delta\bar{q}(s)} = \int \mathrm{d}^4 u \frac{\delta^2 \log \mathcal{Z}}{\delta\bar{\xi}(u)\delta\xi(y)} \frac{\delta^2\Gamma}{\delta\bar{q}(s)\delta q(u)} \tag{A.17}$$

and

$$\frac{\delta}{\delta\lambda^a_\mu(v)} = \int \mathrm{d}^4 t \frac{\delta B^b_\nu(t)}{\delta\lambda^a_\mu(v)} \frac{\delta}{\delta B^b_\nu(t)} = \int \mathrm{d}^4 t \frac{\delta^2 \log \mathcal{Z}}{\delta\lambda^a_\mu(v)\delta\lambda^b_\nu(t)} \frac{\delta}{\delta B^b_\nu(t)} \tag{A.18}$$

by applying the chain rule [7]. From Eq. (A.16) and with the aid of Eq. (A.18) the product rule generates a functional equation relating the connected 3-point function of Eq. (A.12) to the 1PI vertex function:

$$\begin{aligned}
0 &= \frac{\delta}{\delta\lambda^a_\mu(v)} \left[\delta(w-u)\right] \qquad (A.19)\\
&= \frac{\delta}{\delta\lambda^a_\mu(v)} \left[\int \mathrm{d}^4 s \frac{\delta^2\Gamma}{\delta\bar{q}(s)\delta q(u)} \frac{\delta^2 \log \mathcal{Z}}{\delta\bar{\xi}(w)\delta\xi(s)}\right]\\
&= \int \mathrm{d}^4 s \left\{ \frac{\delta}{\delta\lambda^a_\mu(v)} \left[\frac{\delta^2\Gamma}{\delta\bar{q}(s)\delta q(u)}\right] \frac{\delta^2 \log \mathcal{Z}}{\delta\bar{\xi}(w)\delta\xi(s)} + \frac{\delta^2\Gamma}{\delta\bar{q}(s)\delta q(u)} \frac{\delta}{\delta\lambda^a_\mu(v)} \left[\frac{\delta^2 \log \mathcal{Z}}{\delta\bar{\xi}(w)\delta\xi(s)}\right] \right\}\\
&= \int \mathrm{d}^4 s \left\{ \int \mathrm{d}^4 t \left(\frac{\delta^2 \log \mathcal{Z}}{\delta\lambda^a_\mu(v)\delta\lambda^b_\nu(t)} \frac{\delta}{\delta B^b_\nu(t)} \left[\frac{\delta^2\Gamma}{\delta\bar{q}(s)\delta q(u)}\right] \frac{\delta^2 \log \mathcal{Z}}{\delta\bar{\xi}(w)\delta\xi(s)} \right) + \right.\\
&\qquad \left. + \frac{\delta^2\Gamma}{\delta\bar{q}(s)\delta q(u)} \frac{\delta}{\delta\lambda^a_\mu(v)} \left[\frac{\delta^2 \log \mathcal{Z}}{\delta\bar{\xi}(w)\delta\xi(s)}\right] \right\}\\
&= \int \mathrm{d}^4 s \int \mathrm{d}^4 t \frac{\delta^2 \log \mathcal{Z}}{\delta\lambda^a_\mu(v)\delta\lambda^b_\nu(t)} \frac{\delta^3\Gamma}{\delta B^b_\nu(t)\delta\bar{q}(s)\delta q(u)} \frac{\delta^2 \log \mathcal{Z}}{\delta\bar{\xi}(w)\delta\xi(s)} +\\
&\quad \int \mathrm{d}^4 s \frac{\delta^2\Gamma}{\delta\bar{q}(s)\delta q(u)} \frac{\delta^3 \log \mathcal{Z}}{\delta\lambda^a_\mu(v)\delta\bar{\xi}(w)\delta\xi(s)}.
\end{aligned}$$

To explicitly express the 3-point function in Eq. (A.12) shift the first summand of the equation above to the left-hand side and multiply the new equation by $\delta^2 \log \mathcal{Z}/\delta\bar{\xi}(u)\delta\xi(y)$

[7] Keep in mind the summation over the Gell-Mann and Lorentz indices in Eq. (A.18).

from the left. Finally, integrate w.r.t. u and apply Eq. (A.17), i.e. [8]

$$\begin{aligned}
&\int \mathrm{d}^4 s \int \mathrm{d}^4 t \int \mathrm{d}^4 u \frac{\delta^2 \log \mathcal{Z}}{\delta\bar{\xi}(u)\delta\xi(y)} \frac{\delta^2 \log \mathcal{Z}}{\delta\lambda^a_\mu(v)\delta\lambda^b_\nu(t)} \frac{\delta^3 \Gamma}{\delta B^b_\nu(t)\delta\bar{q}(s)\delta q(u)} \frac{\delta^2 \log \mathcal{Z}}{\delta\bar{\xi}(w)\delta\xi(s)} \\
= & -\int \mathrm{d}^4 s \int \mathrm{d}^4 u \frac{\delta^2 \log \mathcal{Z}}{\delta\bar{\xi}(u)\delta\xi(y)} \frac{\delta^2 \Gamma}{\delta\bar{q}(s)\delta q(u)} \frac{\delta^3 \log \mathcal{Z}}{\delta\lambda^a_\mu(v)\delta\bar{\xi}(w)\delta\xi(s)} \\
= & -\int \mathrm{d}^4 s\, \delta(s-y) \frac{\delta^3 \log \mathcal{Z}}{\delta\lambda^a_\mu(v)\delta\bar{\xi}(w)\delta\xi(s)} \\
= & -\frac{\delta^3 \log \mathcal{Z}}{\delta\lambda^a_\mu(v)\delta\bar{\xi}(w)\delta\xi(y)}.
\end{aligned} \tag{A.20}$$

The function $\delta^3\Gamma/\delta B^b_\nu(t)\delta\bar{q}(s)\delta q(u)$ is the 1PI quark gluon vertex [Das06, Ch. 10.2].

By applying Eq. (A.20), Eq. (A.12) can be expressed by means of 1PI n-point functions

$$\begin{aligned}
0 = & -(\gamma_\mu\partial_\mu + m)\frac{\delta^2 \log \mathcal{Z}}{\delta\bar{\xi}(x)\delta\xi(y)} \\
& -i\,g t^a \gamma_\mu \int \mathrm{d}^4 v \int \mathrm{d}^4 w\, \delta(v-x)\delta(w-x) \int \mathrm{d}^4 s \int \mathrm{d}^4 t \int \mathrm{d}^4 u \\
& \qquad \times \left\{ -\frac{\delta^2 \log \mathcal{Z}}{\delta\bar{\xi}(u)\delta\xi(y)} \frac{\delta^2 \log \mathcal{Z}}{\delta\lambda^a_\mu(v)\delta\lambda^b_\nu(t)} \frac{\delta^3 \Gamma}{\delta B^b_\nu(t)\delta\bar{q}(s)\delta q(u)} \frac{\delta^2 \log \mathcal{Z}}{\delta\bar{\xi}(w)\delta\xi(s)} \right\} \\
& +\delta(x-y) \\
= & -(\gamma_\mu\partial_\mu + m)\frac{\delta^2 \log \mathcal{Z}}{\delta\bar{\xi}(x)\delta\xi(y)} \\
& +i\,g t^a \gamma_\mu \int \mathrm{d}^4 s \int \mathrm{d}^4 t \int \mathrm{d}^4 u \frac{\delta^2 \log \mathcal{Z}}{\delta\bar{\xi}(u)\delta\xi(y)} \frac{\delta^2 \log \mathcal{Z}}{\delta\lambda^a_\mu(x)\delta\lambda^b_\nu(t)} \frac{\delta^3 \Gamma}{\delta B^b_\nu(t)\delta\bar{q}(s)\delta q(u)} \frac{\delta^2 \log \mathcal{Z}}{\delta\bar{\xi}(x)\delta\xi(s)} \\
& +\delta(x-y) \\
= & -(\gamma_\mu\partial_\mu + m) S(x-y) \\
& +i\,g t^a \gamma_\mu \int \mathrm{d}^4 s \int \mathrm{d}^4 t \int \mathrm{d}^4 u\, S(u-y) D^{ab}_{\mu\nu}(x-t)\Gamma^b_\mu(t,s,u) S(x-s) \\
& +\delta(x-y).
\end{aligned} \tag{A.21}$$

[9]

This is the quark Dyson-Schwinger equation for the unrenormalized quark propagator in configuration space. Subsequent Fourier transformation and multiplication by the inverse quark propagator yields the quark DSE in momentum space.

[8] Because $\delta^2 \log \mathcal{Z}/\delta\bar{\xi}(u)\delta\xi(y)$ does not depend on s or t this function can be pulled to the right of the respective integral operators. The functions are assumed to be well-behaved, which is why the integral operators commute with each other.

[9] In the last step, the limit of vanishing sources is implicitly carried out.

B Euclidean space formalism

All calculations of this thesis use Euclidean space. For a short introduction to Euclidean space formalism see e.g. [Rob94]. In the following, only those details crucial to the presented calculations are given.

The Euclidean metric reads

$$g_{\mu\nu} = \begin{pmatrix} 1 & 0 & 0 & 0 \\ 0 & 1 & 0 & 0 \\ 0 & 0 & 1 & 0 \\ 0 & 0 & 0 & 1 \end{pmatrix} = \delta_{\mu\nu} \tag{B.1}$$

with the Euclidean indices $\mu, \nu = 1, 2, 3, 4$. These indices are also referred to as Lorentz indices (cf. [Alk01]). Because the metric corresponds to the unity matrix, there is no need to distinguish between covariant and contravariant vectors. For this reason in this thesis, Euclidean space indices are lower indices by convention. Furthermore, the summation over twice appearing Euclidean indices is implicit,

$$a_\mu b_\mu \equiv \sum_{\alpha=1}^{4} a_\alpha b_\alpha. \tag{B.2}$$

Following [Rob00] O(4) symmetry is considered for space-time transformations.

As familiar from Minkowski space quantum theory (cf. [Itz05]) the description of spin-1/2 particles in Euclidean space calls for a Clifford algebra defined by

$$\{\gamma_\mu, \gamma_\nu\} = \gamma_\mu\gamma_\nu + \gamma_\nu\gamma_\mu = 2g_{\mu\nu}\mathbb{I}_4 \tag{B.3}$$

with $g_{\mu\nu} = \delta_{\mu\nu}$. The construction of a matrix representation of this algebra in d dimensions can be found in [ZJ93]. In $d = 4$ dimensions, one representation of the Euclidean γ matrices

is given as:

$$\gamma_1 = \begin{pmatrix} 0 & 0 & 0 & 1 \\ 0 & 0 & 1 & 0 \\ 0 & 1 & 0 & 0 \\ 1 & 0 & 0 & 0 \end{pmatrix}, \qquad \gamma_2 = \begin{pmatrix} 0 & 0 & 0 & -i \\ 0 & 0 & i & 0 \\ 0 & -i & 0 & 0 \\ i & 0 & 0 & 0 \end{pmatrix}, \tag{B.4}$$

$$\gamma_3 = \begin{pmatrix} 0 & 0 & 1 & 0 \\ 0 & 0 & -1 & 0 \\ 1 & 0 & 0 & 0 \\ 0 & 1 & 0 & 0 \end{pmatrix}, \quad \gamma_4 = \begin{pmatrix} 0 & 0 & -i & 0 \\ 0 & 0 & 0 & -i \\ i & 0 & 0 & 0 \\ 0 & i & 0 & 0 \end{pmatrix}.$$

Contrary to the Minkowski space representation, the Euclidean γ matrices are hermitian.

The Feynman slash notation can be adapted to the Euclidean space, as well, i.e.

$$\not{a} := \gamma_\mu a_\mu. \tag{B.5}$$

In Euclidean space, identities of products of slash expressions resemble those in Minkowski space [1]. The manipulations on the decomposed quark propagator require the following identities:

$$\begin{aligned}
\not{a}\not{b} &= a_\mu b_\nu \gamma_\mu \gamma_\nu = \frac{1}{2}\left(a_\mu b_\nu \gamma_\mu \gamma_\nu + a_\nu b_\mu \gamma_\nu \gamma_\mu\right) = \delta_{\mu\nu} a_\mu b_\nu = a_\mu b_\nu, \\
\not{a}^2 &= a^2, \\
\gamma_\mu \not{a} \gamma_\mu &= a_\nu \gamma_\mu \gamma_\nu \gamma_\mu = a_\nu \gamma_\mu (2\,\delta_{\mu\nu} - \gamma_\mu \gamma_\nu) = 2\,a_\nu \gamma_\nu - 4\,a_\nu \gamma_\nu = -2\not{a}, \\
\not{a}\not{b}\not{a} &= a_\mu b_\nu a_\lambda \gamma_\mu \gamma_\nu \gamma_\lambda \\
&= a_\mu b_\nu a_\lambda \gamma_\mu \left(2\,\delta_{\nu\lambda} - \gamma_\lambda \gamma_\nu\right) \\
&= 2\,b_\nu a_\nu a_\mu \gamma_\mu - a_\mu a_\lambda \gamma_\mu \gamma_\lambda b_\nu \gamma_\nu \\
&= 2ab\not{a} - a^2\not{b}.
\end{aligned} \tag{B.6}$$

[1] Those identities follow from the Clifford algebra.

C Integral equations for the dressing functions

The quark propagator can be decomposed with respect to its Dirac structure. This treatment results in the quark dressing functions $A(p^2)$ and $B(p^2)$ in case of the vacuum DSE and essentially in the dressing functions $A(\boldsymbol{p}^2, \omega_n)$, $B(\boldsymbol{p}^2, \omega_n)$ and $C(\boldsymbol{p}^2, \omega_n)$ in case of considering finite temperatures. Thus, the DSE for the quark propagator is transformed into coupled integral equations for the dressing functions.

C.1 Vacuum

This section shows the decomposition of the quark DSE in vacuum (cf. Eq. (2.4.6))

$$S^{-1}(p) = (i\not{p} + m) + \frac{4}{3}\int \frac{\mathrm{d}^4 l}{(2\pi)^4} \Delta_D\left((p-l)^2\right)\left(\delta_{\mu\nu} - \frac{q_\mu q_\nu}{q^2}\right)\gamma_\mu S(l)\gamma_\nu \tag{C.1}$$

with $q_\mu = p_\mu - l_\mu$ by means of the dressing functions A and B constituting the inverse quark propagator

$$S^{-1}(p) \;=\; i\not{p}A(p^2) + B(p^2). \tag{C.2}$$

This task mainly involves the evaluation of the index structure in Eq. (C.1)

$$\left(\delta_{\mu\nu} - \frac{q_\mu q_\nu}{q^2}\right)\gamma_\mu S(l)\gamma_\nu = \gamma_\mu S(l)\gamma_\mu - \not{q}S(l)\not{q}\frac{1}{q^2}, \tag{C.3}$$

i.e. the reduction of the Dirac structure. The matrix structure of the quark propagator $S(l)$ follows by virtue of an expansion [1]

$$\begin{aligned} S(l) &= \frac{1}{(i\not{l}A(l^2) + B(l^2))}\frac{(-i\not{l}A(l^2) + B(l^2))}{(-i\not{l}A(l^2) + B(l^2))} \\ &= \frac{-i\not{l}A(l^2) + B(l^2)}{\not{l}^2 A^2(l^2) + B^2(l^2)} \end{aligned} \tag{C.4}$$

[1] Note that $\{\gamma_\mu, \mathbb{I}_4\} = 0$.

$$= \frac{-i\not{l}A(l^2)+B(l^2)}{l^2A^2(l^2)+B^2(l^2)}.$$

Hence, the first term on the right hand side of Eq. (C.3) yields

$$\begin{aligned}\gamma_\mu S(l)\gamma_\mu &= \gamma_\mu \frac{-i\not{l}A(l^2)+B(l^2)}{l^2A^2(l^2)+B^2(l^2)}\gamma_\mu \\ &= \frac{1}{l^2A^2(l^2)+B^2(l^2)}\left(-i\,\gamma_\mu\not{l}\gamma_\mu A(l^2)+\gamma_\mu\gamma_\mu B(l^2)\right) \\ &= \frac{1}{l^2A^2(l^2)+B^2(l^2)}\left(-i\,(-2\not{l}A(l^2))+4B(l^2)\right) \\ &= \frac{2i\not{l}A(l^2)+4B(l^2)}{l^2A^2(l^2)+B^2(l^2)},\end{aligned} \tag{C.5}$$

and the second one is

$$\begin{aligned}\not{q}S(l)\not{q}\frac{1}{q^2} &= \frac{1}{q^2}\frac{1}{l^2A^2(l^2)+B^2(l^2)}\left(-i\,\not{q}\not{l}\not{q}A(l^2)+\not{q}\not{q}B(l^2)\right) \\ &= \frac{1}{q^2}\frac{1}{l^2A^2(l^2)+B^2(l^2)}\left(-i\,\left[2ql\not{q}-q^2\not{l}\right]A(l^2)+q^2B(l^2)\right) \\ &= \frac{+i\,q^2\not{l}A(l^2)-2i\,ql\not{q}A(l^2)+q^2B(l^2)}{l^2A^2(l^2)+B^2(l^2)}\frac{1}{q^2}.\end{aligned} \tag{C.6}$$

Finally, the index structure of Eq. (C.3) reads

$$\begin{aligned}L &:= \left(\delta_{\mu\nu}-\frac{q_\mu q_\nu}{q^2}\right)\gamma_\mu S(l)\gamma_\nu \\ &= \frac{2i\not{l}A(l^2)+4B(l^2)}{l^2A^2(l^2)+B^2(l^2)}-\frac{+i\,q^2\not{l}A(l^2)-2i\,ql\not{q}A(l^2)+q^2B(l^2)}{l^2A^2(l^2)+B^2(l^2)}\frac{1}{q^2} \\ &= \frac{1}{l^2A^2(l^2)+B^2(l^2)}\left\{2i\not{l}A(l^2)+4B(l^2)-\frac{+i\,q^2\not{l}A(l^2)-2i\,ql\not{q}A(l^2)+q^2B(l^2)}{q^2}\right\} \\ &= \frac{1}{l^2A^2(l^2)+B^2(l^2)}\left\{\left(\not{l}+\frac{2ql\not{q}}{q^2}\right)i\,A(l^2)+3B(l^2)\right\}.\end{aligned} \tag{C.7}$$

Consequently, the quark DSE has the following form

$$\begin{aligned}S^{-1}(p) &= i\not{p}A(p^2)+B(p^2) \\ &= (i\not{p}+m)+\frac{4}{3}\int\frac{\mathrm{d}^4l}{(2\pi)^4}\frac{\Delta_D\left((p-l)^2\right)}{l^2A^2(l^2)+B^2(l^2)}\left\{\left(\not{l}+\frac{2ql\not{q}}{q^2}\right)i\,A(l^2)+3B(l^2)\right\}.\end{aligned} \tag{C.8}$$

The integrand of the self-energy term contains the non-factorizing slashed term $\not{l}$. This is treated by the argument that the integral has to be O(4) invariant. Generally, the integration of an expression containing slashed terms (and no products of slashed terms)

gives

$$\int \frac{\mathrm{d}^4 l}{(2\pi)^4} \not{l} f(l) = \gamma_1 I_1 + \gamma_2 I_2 + \gamma_3 I_3 + \gamma_4 I_4 \tag{C.9}$$

with f a scalar integrable function and I_μ denote the coefficients to be determined. In case of the quark DSE, this integral is constrained to be O(4) invariant. Hence, it becomes

$$\int \frac{\mathrm{d}^4 l}{(2\pi)^4} \not{l} f(l) = \not{p} I. \tag{C.10}$$

The factor I can be specified by using the relations between slashed variables,

$$\begin{aligned}
\not{p} I &= \int \frac{\mathrm{d}^4 l}{(2\pi)^4} \not{l} f(l), \qquad (C.11)\\
\frac{1}{p^2} \not{p} (\not{p} I) \not{p} &= \frac{1}{p^2} \not{p} \left(\int \frac{\mathrm{d}^4 l}{(2\pi)^4} \not{l} f(l) \right) \not{p},\\
I \not{p} &= \int \frac{\mathrm{d}^4 l}{(2\pi)^4} \frac{1}{p^2} \not{p} \not{l} \not{p} f(l)\\
&= \int \frac{\mathrm{d}^4 l}{(2\pi)^4} \frac{1}{p^2} \left[2pl \not{p} - p^2 \not{l} \right] f(l)\\
&= \int \frac{\mathrm{d}^4 l}{(2\pi)^4} \frac{1}{p^2} 2pl \not{p} - I \not{p}\\
&= \int \frac{\mathrm{d}^4 l}{(2\pi)^4} \frac{pl}{p^2} \not{p}.
\end{aligned}$$

Using $\not{q} = \not{p} - \not{l}$ this conversion [2] transforms Eq. (C.8) into

$$\begin{aligned}
S^{-1}(p) &= i \not{p} A(p^2) + B(p^2) \qquad (C.12)\\
&= (i \not{p} + m) + \frac{4}{3} \int \frac{\mathrm{d}^4 l}{(2\pi)^4} Q(p,l) \left\{ \not{p} \left(\frac{pl}{p^2} + \frac{2ql}{q^2} \left(1 - \frac{pl}{p^2} \right) \right) i\, A(l^2) + 3B(l^2) \right\}\\
&= (i \not{p} + m) + i \frac{4}{3} \not{p} \int \frac{\mathrm{d}^4 l}{(2\pi)^4} Q(p,l) \left(\frac{pl}{p^2} + \frac{2ql}{q^2} \left(1 - \frac{pl}{p^2} \right) \right) A(l^2)\\
&\qquad + \frac{4}{3} \int \frac{\mathrm{d}^4 l}{(2\pi)^4} Q(p,l) 3B(l^2)
\end{aligned}$$

with

$$Q(p,l) := \frac{\Delta_D\left((p-l)^2\right)}{l^2 A^2(l^2) + B^2(l^2)}. \tag{C.13}$$

[2] The transformation (C.10) is sometimes referred to as Passarino-Veltman trick, cf. [Pas79].

By equating coefficients w.r.t. $\not{p}$ and $\mathbb{I}_4$ one arrives at

$$\begin{aligned} A(p^2) &= 1 + \frac{4}{3}\int \frac{\mathrm{d}^4 l}{(2\pi)^4} Q(p,l)\left(\frac{pl}{p^2} + \frac{2ql}{q^2}\left(1 - \frac{pl}{p^2}\right)\right) A(l^2) \\ B(p^2) &= m + 4\int \frac{\mathrm{d}^4 l}{(2\pi)^4} Q(p,l) B(l^2). \end{aligned} \tag{C.14}$$

C.2 Non-zero temperatures

This section shows the decomposition of the quark DSE at finite temperatures (cf. Eq. (2.5.13))

$$\begin{aligned} S^{-1}(\boldsymbol{p},\omega_n) &= i\,\boldsymbol{\gamma p} + i\,\gamma_4\omega_n + m + \frac{4}{3}T\sum_{m=-\infty}^{\infty}\int \frac{\mathrm{d}^3 l}{(2\pi)^3} g^2 D_{\mu\nu}(q^2)\gamma_\mu S(\boldsymbol{l},\omega_m)\gamma_\nu \\ &= i\,\boldsymbol{\gamma p} + i\,\gamma_4\omega_n + m + \frac{4}{3}T\sum_{m=-\infty}^{\infty}\int \frac{\mathrm{d}^3 l}{(2\pi)^3} \\ &\qquad \times \Big[{P^L}_{\mu\nu}(\boldsymbol{q},\Omega_{nm})\gamma_\mu S(\boldsymbol{l},\omega_m)\gamma_\nu \Delta_F(\boldsymbol{q},\Omega_{nm}) \\ &\qquad\quad + {P^T}_{\mu\nu}(\boldsymbol{q},\Omega_{nm})\gamma_\mu S(\boldsymbol{l},\omega_m)\gamma_\nu \Delta_G(\boldsymbol{q},\Omega_{nm})\Big] \end{aligned} \tag{C.15}$$

with $\boldsymbol{q} = \boldsymbol{p} - \boldsymbol{l}$ and $\Omega_{nm} = \omega_n - \omega_m$ with respect to the dressing functions A, C and B constituting the inverse quark propagator at finite temperatures

$$S^{-1}(\boldsymbol{p},\omega_n) = i\,\boldsymbol{\gamma p} A(\boldsymbol{p}^2,\omega_n) + i\,\gamma_4\omega_n C(\boldsymbol{p}^2,\omega_n) + B(\boldsymbol{p}^2,\omega_n). \tag{C.16}$$

Like in the vacuum case, this mainly involves the reduction of the Dirac structure in Eq. (C.15)

$$T := {P^T}_{\mu\nu}\gamma_\mu S\gamma_\nu \qquad \text{and} \qquad L := {P^L}_{\mu\nu}\gamma_\mu S\gamma_\nu. \tag{C.17}$$

The objects ${P^T}_{\mu\nu}$ and ${P^L}_{\mu\nu}$ denote the projectors mapping transversally and longitudinally to the vector q given in the heat-bath rest frame

$$\begin{aligned} {P^T}_{\mu\nu}(\boldsymbol{q},\Omega_{nm}) &:= \begin{cases} 0; & \mu = 4 \quad \text{and/or} \quad \nu = 4 \\ \delta_{ij} - \frac{q_i q_j}{\boldsymbol{q}^2}; & i,j = \mu,\nu = 1,2,3 \end{cases}, \\ {P^L}_{\mu\nu}(\boldsymbol{q},\Omega_{nm}) &:= \delta_{\mu\nu} - \frac{q_\mu q_\nu}{q^2} - {P^T}_{\mu\nu}(\boldsymbol{q},\Omega_{nm}) \end{aligned}$$

$$= \begin{cases} \delta_{\mu\nu} - \frac{q_\mu q_\nu}{q^2}; & \mu = 4 \quad \text{and/or} \quad \nu = 4 \\ \frac{\Omega_{nm}^2}{q^2}\frac{q_i q_j}{\boldsymbol{q}^2}; & i,j = \mu,\nu = 1,2,3 \quad . \end{cases}$$

The matrix structure of the quark propagator follows by expansion [3,4]

$$\begin{aligned} S(\boldsymbol{l},\omega_m) &= \frac{1}{(i\,\boldsymbol{\gamma l} A + i\,\gamma_4\omega_m C + B)}\frac{(-i\,\boldsymbol{\gamma l} A - i\,\gamma_4\omega_m C + B)}{(-i\,\boldsymbol{\gamma l} A - i\,\gamma_4\omega_m C + B)} \\ &= \frac{-i\,\boldsymbol{\gamma l} A - i\,\gamma_4\omega_m C + B}{(\boldsymbol{\gamma l} A + \gamma_4\omega_m C)^2 + B^2} \\ &= \frac{-i\,\boldsymbol{\gamma l} A - i\,\gamma_4\omega_m C + B}{\boldsymbol{p}^2 A^2 + {\omega_m}^2 C^2 + B^2} \\ &= -i\,\boldsymbol{\gamma l}\sigma_A - i\,\gamma_4\omega_m\sigma_C + \sigma_B \end{aligned} \tag{C.18}$$

using the definition of the reduced dressing functions:

$$\sigma_F(\boldsymbol{l}^2,\omega_m) := \frac{F(\boldsymbol{l}^2,\omega_m)}{\boldsymbol{p}^2 A^2(\boldsymbol{l}^2,\omega_m) + {\omega_m}^2 C^2(\boldsymbol{l}^2,\omega_m) + B^2(\boldsymbol{l}^2,\omega_m)} \tag{C.19}$$

with F being dummy for A, B, and C, respectively.

In preparation to integrate T and L over the spatial momentum range, Eq. (C.11) of the vacuum case is adapted to the finite temperature case involving O(3) symmetry [5]

$$\begin{aligned} \int \frac{\mathrm{d}^3 l}{(2\pi)^3}\boldsymbol{\gamma l}\, g(l) &= \boldsymbol{p} J \\ &= \int \frac{\mathrm{d}^3 l}{(2\pi)^3}\frac{\boldsymbol{pl}}{\boldsymbol{p}^2}\boldsymbol{\gamma p} \end{aligned} \tag{C.20}$$

with g an integrable function and J a respective constant. Thus, the transversal part T reduces to

$$\begin{aligned} T &= {P^T}_{\mu\nu}\gamma_\mu S\gamma_\nu \\ &= {P^T}_{44}\gamma_4 S\gamma_4 + {P^T}_{4j}\gamma_4 S\gamma_j + {P^T}_{i4}\gamma_i S\gamma_4 + {P^T}_{ij}\gamma_i S\gamma_j \\ &= 0 + 0 + 0 + {P^T}_{ij}\gamma_i S\gamma_j \\ &= \left(\delta_{ij} - \frac{q_i q_j}{\boldsymbol{q}^2}\right)\gamma_i(-i\,\boldsymbol{\gamma l}\sigma_A - i\,\gamma_4\omega_m\sigma_C + \sigma_B)\gamma_j \\ &= \left(\delta_{ij} - \frac{q_i q_j}{\boldsymbol{q}^2}\right)\gamma_i\left\{\gamma_j(i\,\boldsymbol{\gamma l}\sigma_A + i\,\gamma_4\omega_m\sigma_C + \sigma_B) - i\,2\delta_{kj}l_k\sigma_A\right\} \end{aligned} \tag{C.21}$$

[3] For convenience, the arguments of the dressing functions and of the to-be defined functions σ_A, σ_B and σ_C are omitted.

[4] Note that $[\gamma_\mu, \mathbb{I}_4] = 0$ and $\{\boldsymbol{\gamma}, \gamma_4\} = 0$.

[5] When using the identities Eq. (B.6) for O(3) considerations, the Euclidean indices include only $\mu,\nu = 1$, 2, and 3.

$$
\begin{aligned}
&= \gamma_i\gamma_i(i\,\boldsymbol{\gamma l}\sigma_A + i\,\gamma_4\omega_m\sigma_C + \sigma_B) - i\,\gamma_i 2\delta_{ki}l_k\sigma_A \\
&\quad -\frac{q_iq_j}{\boldsymbol{q}^2}\gamma_i\gamma_j(i\,\boldsymbol{\gamma l}\sigma_A + i\,\gamma_4\omega_m\sigma_C + \sigma_B) + 2i\,\frac{q_iq_j}{\boldsymbol{q}^2}\gamma_i\delta_{kj}l_k\sigma_A \\
&= 3(i\,\boldsymbol{\gamma l}\sigma_A + i\,\gamma_4\omega_m\sigma_C + \sigma_B) - 2i\,\boldsymbol{\gamma l}\sigma_A \\
&\quad -1\cdot(i\,\boldsymbol{\gamma l}\sigma_A + i\,\gamma_4\omega_m\sigma_C + \sigma_B) + 2i\,\frac{(\boldsymbol{ql})}{\boldsymbol{q}^2}\boldsymbol{\gamma q}\sigma_A \\
&= 2i\,\frac{(\boldsymbol{ql})}{\boldsymbol{q}^2}\boldsymbol{\gamma q}\sigma_A + 2i\,\gamma_4\omega_m\sigma_C + 2\sigma_B \\
&\quad \text{(application of Passarino-Veltman trick in view of having } T \text{ in the integrand)} \\
&= i\,\boldsymbol{\gamma p}\,2\frac{(\boldsymbol{ql})}{\boldsymbol{q}^2}\left(1-\frac{\boldsymbol{pl}}{\boldsymbol{p}^2}\right)\sigma_A + i\,\gamma_4\,2\omega_m\sigma_C + 2\sigma_B.
\end{aligned}
$$

The reduction of the longitudinal part is conveniently separated into three parts

$$
\begin{aligned}
L &= P^L{}_{\mu\nu}\gamma_\mu S\gamma_\nu \qquad\qquad\qquad\qquad\qquad\qquad\qquad\qquad\qquad\qquad (C.22)\\
&= P^L{}_{44}\gamma_4 S\gamma_4 \;+\left(P^L{}_{4j}\gamma_4 S\gamma_j + P^L{}_{i4}\gamma_i S\gamma_4\right) + P^L{}_{ij}\gamma_i S\gamma_j \\
&= L_1 \qquad\qquad + L_2 \qquad\qquad\qquad\qquad + L_3
\end{aligned}
$$

which give

$$
\begin{aligned}
L_1 &:= P^L{}_{44}\gamma_4 S\gamma_4 \qquad\qquad\qquad\qquad\qquad\qquad\qquad\qquad\qquad\qquad (C.23)\\
&= \left(\delta_{44}-\frac{q_4q_4}{q^2}\right)\gamma_4(-i\,\boldsymbol{\gamma l}\sigma_A - i\,\gamma_4\omega_m\sigma_C + \sigma_B)\gamma_4 \\
&= \left(1-\frac{\Omega_{nm}^2}{q^2}\right)\gamma_4\gamma_4(i\,\boldsymbol{\gamma l}\sigma_A - i\,\gamma_4\omega_m\sigma_C + \sigma_B) \\
&= (i\,\boldsymbol{\gamma l}\sigma_A - i\,\gamma_4\omega_m\sigma_C + \sigma_B) - \frac{\Omega_{nm}^2}{q^2}(i\,\boldsymbol{\gamma l}\sigma_A - i\,\gamma_4\omega_m\sigma_C + \sigma_B), \\
L_2 &:= P^L{}_{4j}\gamma_4 S\gamma_j + P^L{}_{i4}\gamma_i S\gamma_4 \\
&= \left(\delta_{4j}-\frac{q_4q_j}{q^2}\right)\gamma_4(-i\,\boldsymbol{\gamma l}\sigma_A - i\,\gamma_4\omega_m\sigma_C + \sigma_B)\gamma_j \\
&\quad +\left(\delta_{i4}-\frac{q_iq_4}{q^2}\right)\gamma_i(-i\,\boldsymbol{\gamma l}\sigma_A - i\,\gamma_4\omega_m\sigma_C + \sigma_B)\gamma_4 \\
&= \frac{q_4q_i}{q^2}\,[\gamma_4(i\,\gamma_k l_k\sigma_A + i\,\gamma_4\omega_m\sigma_C - \sigma_B)\gamma_i \\
&\qquad + \gamma_i(i\,\gamma_k l_k\sigma_A + i\,\gamma_4\omega_m\sigma_C - \sigma_B)\gamma_4] \\
&= \frac{q_iq_4}{q^2}[i\,(\gamma_i\gamma_k+\gamma_k\gamma_i)l_k\sigma_A\gamma_4 + i\,(\gamma_i\gamma_4\gamma_4+\gamma_4\gamma_4\gamma_i)\omega_m\sigma_C - (\gamma_i\gamma_4+\gamma_4\gamma_i)\sigma_B] \\
&= \frac{q_iq_4}{q^2}[i\,2\delta_{ik}l_k\sigma_A\gamma_4 + 2i\,\gamma_i\omega_m\sigma_C - 0] \\
&= \frac{\Omega_{nm}}{q^2}[2i\,(\boldsymbol{ql})\gamma_4\sigma_A + 2i\,\boldsymbol{\gamma q}\omega_m\sigma_C],
\end{aligned}
$$

$$
\begin{aligned}
L_3 &:= P^L{}_{ij}\gamma_i S\gamma_j \\
&= \frac{\Omega_{nm}^2}{q^2}\frac{q_i q_j}{(\boldsymbol{q}^2)}\gamma_i(-i\,\boldsymbol{\gamma l}\sigma_A - i\,\gamma_4\omega_m\sigma_C + \sigma_B)\gamma_j \\
&\overset{\text{cf. } T}{=} \frac{\Omega_{nm}^2}{q^2}\left[1\cdot(i\,\boldsymbol{\gamma l}\sigma_A + i\,\gamma_4\omega_m\sigma_C + \sigma_B) - 2i\,\frac{(\boldsymbol{ql})}{\boldsymbol{q}^2}\boldsymbol{\gamma q}\sigma_A\right] \\
&= \frac{\Omega_{nm}^2}{q^2}(i\,\boldsymbol{\gamma l}\sigma_A + i\,\gamma_4\omega_m\sigma_C + \sigma_B) - \frac{\Omega_{nm}^2}{q^2}2i\,\frac{(\boldsymbol{ql})}{\boldsymbol{q}^2}\boldsymbol{\gamma q}\sigma_A
\end{aligned}
$$

and altogether

$$
\begin{aligned}
L &= (i\,\boldsymbol{\gamma l}\sigma_A - i\,\gamma_4\omega_m\sigma_C + \sigma_B) - \frac{\Omega_{nm}^2}{q^2}(i\,\boldsymbol{\gamma l}\sigma_A - i\,\gamma_4\omega_m\sigma_C + \sigma_B) \\
&\quad + \frac{\Omega_{nm}}{q^2}[2i\,\gamma_4(\boldsymbol{ql})\sigma_A + 2i\,\boldsymbol{\gamma q}\omega_m\sigma_C] \\
&\quad + \frac{\Omega_{nm}^2}{q^2}(i\,\boldsymbol{\gamma l}\sigma_A + i\,\gamma_4\omega_m\sigma_C + \sigma_B) - \frac{\Omega_{nm}^2}{q^2}2i\,\frac{(\boldsymbol{ql})}{\boldsymbol{q}^2}\boldsymbol{\gamma q}\sigma_A \\
&= (i\,\boldsymbol{\gamma l}\sigma_A - i\,\gamma_4\omega_m\sigma_C + \sigma_B) \\
&\quad + \frac{\Omega_{nm}}{q^2}[2i\,\gamma_4(\boldsymbol{ql})\sigma_A + 2i\,\boldsymbol{\gamma q}\omega_m\sigma_C] \\
&\quad + \frac{\Omega_{nm}^2}{q^2}(2i\,\gamma_4\omega_m\sigma_C) - \frac{\Omega_{nm}^2}{q^2}2i\,\frac{(\boldsymbol{ql})}{\boldsymbol{q}^2}\boldsymbol{\gamma q}\sigma_A \\
&= i\,\boldsymbol{\gamma l}\sigma_A - i\,(1 - 2\frac{\Omega_{nm}^2}{q^2})\gamma_4\omega_m\sigma_C + \sigma_B + \frac{\Omega_{nm}}{q^2}[2i\,\gamma_4(\boldsymbol{ql})\sigma_A + 2i\,\boldsymbol{\gamma q}\omega_m\sigma_C] \\
&\quad - \frac{\Omega_{nm}^2}{q^2}2i\,\frac{(\boldsymbol{ql})}{\boldsymbol{q}^2}\boldsymbol{\gamma q}\sigma_A \\
&= i\,\boldsymbol{\gamma l}\sigma_A + \frac{\Omega_{nm}}{q^2}2i\,\boldsymbol{\gamma q}\omega_m\sigma_C - \frac{\Omega_{nm}^2}{q^2}2i\,\frac{(\boldsymbol{ql})}{\boldsymbol{q}^2}\boldsymbol{\gamma q}\sigma_A - i\,(1 - 2\frac{\Omega_{nm}^2}{q^2})\gamma_4\omega_m\sigma_C \\
&\quad + \frac{\Omega_{nm}}{q^2}2i\,\gamma_4(\boldsymbol{ql})\sigma_A + \sigma_B \\
&\quad \text{(application of Passarino-Veltman trick in view of having } L \text{ in the integrand)} \\
&= i\,\boldsymbol{\gamma p}\left[\frac{\boldsymbol{pl}}{\boldsymbol{p}^2}\sigma_A + \frac{\Omega_{nm}}{q^2}2\,(1 - \frac{\boldsymbol{pl}}{\boldsymbol{p}^2})\omega_m\sigma_C - \frac{\Omega_{nm}^2}{q^2}2\,\frac{(\boldsymbol{ql})}{\boldsymbol{q}^2}(1 - \frac{\boldsymbol{pl}}{\boldsymbol{p}^2})\sigma_A\right] \\
&\quad + i\,\gamma_4\left[-(1 - 2\frac{\Omega_{nm}^2}{q^2})\omega_m\sigma_C + \frac{\Omega_{nm}}{q^2}2\,(\boldsymbol{ql})\sigma_A\right] + \sigma_B.
\end{aligned}
\tag{C.24}
$$

Finally, setting Eqs. (C.21) and (C.24) into Eq. (C.15) yields

$$
\begin{aligned}
S^{-1}(\boldsymbol{p},\omega_n) &= i\,\boldsymbol{\gamma p}A(\boldsymbol{p}^2,\omega_n) + i\,\gamma_4\omega_n C(\boldsymbol{p}^2,\omega_n) + B(\boldsymbol{p}^2,\omega_n) \\
&= i\,\boldsymbol{\gamma p} + i\,\gamma_4\omega_n + m + \frac{4}{3}T\sum_{m=-\infty}^{\infty}\int\frac{\mathrm{d}^3 l}{(2\pi)^3}
\end{aligned}
\tag{C.25}
$$

$$
\begin{aligned}
&\times\Bigg[\Bigg\{i\,\boldsymbol{\gamma p}\left[\frac{\boldsymbol{pl}}{\boldsymbol{p}^2}\sigma_A+\frac{\Omega_{nm}}{q^2}2\left(1-\frac{\boldsymbol{pl}}{\boldsymbol{p}^2}\right)\omega_m\sigma_C-\frac{\Omega_{nm}^2}{q^2}2\,\frac{(\boldsymbol{ql})}{\boldsymbol{q}^2}\left(1-\frac{\boldsymbol{pl}}{\boldsymbol{p}^2}\right)\sigma_A\right]\\
&\qquad+i\,\gamma_4\left[-\left(1-2\frac{\Omega_{nm}^2}{q^2}\right)\omega_m\sigma_C+\frac{\Omega_{nm}}{q^2}2\,(\boldsymbol{ql})\sigma_A\right]+\sigma_B\Bigg\}\Delta_F(\boldsymbol{q},\Omega_{nm})\\
&\qquad+\left\{i\,\boldsymbol{\gamma p}\,2\frac{(\boldsymbol{ql})}{\boldsymbol{q}^2}\left(1-\frac{\boldsymbol{pl}}{\boldsymbol{p}^2}\right)\sigma_A+i\,\gamma_4\,2\omega_m\sigma_C+2\sigma_B\right\}\Delta_G(\boldsymbol{q},\Omega_{nm})\Bigg]\\
=\;& i\,\boldsymbol{\gamma p}+i\,\gamma_4\omega_n+m+\frac{4}{3}T\sum_{m=-\infty}^{\infty}\int\frac{\mathrm{d}^3l}{(2\pi)^3}\\
&\times\Bigg[i\,\boldsymbol{\gamma p}\Bigg\{\Bigg[\frac{\boldsymbol{pl}}{\boldsymbol{p}^2}\sigma_A+\frac{\Omega_{nm}}{q^2}2\left(1-\frac{\boldsymbol{pl}}{\boldsymbol{p}^2}\right)\omega_m\sigma_C\\
&\qquad-\frac{\Omega_{nm}^2}{q^2}2\,\frac{(\boldsymbol{ql})}{\boldsymbol{q}^2}\left(1-\frac{\boldsymbol{pl}}{\boldsymbol{p}^2}\right)\sigma_A\Bigg]\Delta_F(\boldsymbol{q},\Omega_{nm})\\
&\qquad+\;2\frac{(\boldsymbol{ql})}{\boldsymbol{q}^2}\left(1-\frac{\boldsymbol{pl}}{\boldsymbol{p}^2}\right)\sigma_A\Delta_G(\boldsymbol{q},\Omega_{nm})\Bigg\}\\
&\quad+i\,\gamma_4\Bigg\{\Bigg[-\left(1-2\frac{\Omega_{nm}^2}{q^2}\right)\omega_m\sigma_C+\frac{\Omega_{nm}}{q^2}2\,(\boldsymbol{ql})\sigma_A\Bigg]\Delta_F(\boldsymbol{q},\Omega_{nm})\\
&\qquad+2\omega_m\sigma_C\Delta_G(\boldsymbol{q},\Omega_{nm})\}\\
&\quad+\sigma_B\left\{2\,\Delta_G(\boldsymbol{q},\Omega_{nm})+\Delta_F(\boldsymbol{q},\Omega_{nm})\right\}\Bigg].
\end{aligned}
$$

Equating coefficients gives the desired expressions for the dressing functions

$$
\begin{aligned}
A(\boldsymbol{p}^2,\omega_n) &= 1+\frac{4}{3}T\sum_{m=-\infty}^{\infty}\int\frac{\mathrm{d}^3l}{(2\pi)^3} \qquad\text{(C.26)}\\
&\times\Bigg\{\left[\frac{\boldsymbol{pl}}{\boldsymbol{p}^2}\sigma_A+\frac{\Omega_{nm}}{q^2}2\left(1-\frac{\boldsymbol{pl}}{\boldsymbol{p}^2}\right)\omega_m\sigma_C-\frac{\Omega_{nm}^2}{q^2}2\,\frac{(\boldsymbol{ql})}{\boldsymbol{q}^2}\left(1-\frac{\boldsymbol{pl}}{\boldsymbol{p}^2}\right)\sigma_A\right]\Delta_F(\boldsymbol{q},\Omega_{nm})\\
&\quad+\;2\frac{(\boldsymbol{ql})}{\boldsymbol{q}^2}\left(1-\frac{\boldsymbol{pl}}{\boldsymbol{p}^2}\right)\sigma_A\Delta_G(\boldsymbol{q},\Omega_{nm})\Bigg\},\\
C(\boldsymbol{p}^2,\omega_n) &= 1+\frac{1}{\omega_n}\frac{4}{3}T\sum_{m=-\infty}^{\infty}\int\frac{\mathrm{d}^3l}{(2\pi)^3}\\
&\times\Bigg\{\left[-\left(1-2\frac{\Omega_{nm}^2}{q^2}\right)\omega_m\sigma_C+\frac{\Omega_{nm}}{q^2}2\,(\boldsymbol{ql})\sigma_A\right]\Delta_F(\boldsymbol{q},\Omega_{nm})\\
&\quad+2\omega_m\sigma_C\Delta_G(\boldsymbol{q},\Omega_{nm})\Bigg\},
\end{aligned}
$$

$$B(\boldsymbol{p}^2,\omega_n) \;=\; m+\frac{4}{3}T\sum_{m=-\infty}^{\infty}\int\frac{\mathrm{d}^3l}{(2\pi)^3}\,\sigma_B\{2\,\Delta_G(\boldsymbol{q},\Omega_{nm})+\Delta_F(\boldsymbol{q},\Omega_{nm})\}.$$

C.3 Vanishing spatial momentum

After iteration of the quark dressing functions on a given grid, these functions are available for the full range $|\boldsymbol{p}|\in(0,\infty)$; even complex momenta are possible. Having $A(\boldsymbol{l}^2),B(\boldsymbol{l}^2),C(\boldsymbol{l}^2)$ at disposal for a finite set of values $|\boldsymbol{l}|$, Eq. (C.26) provides A, B and C as ordinary functions with $\boldsymbol{p}^2$ as argument. Principally, also the coordinate ω_n can be continued to arbitrary real or complex values in this way.

The point $|\tilde{\boldsymbol{p}}|=0$ constitutes a special case and has to be treated separately [6]. Because the integrand of the integral equation for A contains $1/\boldsymbol{p}^2$ terms, the evaluation of the integral in Eq. (C.26) is not possible. But note that the shapes of the dressing functions remain quasi constant at low momenta (cf. Fig. 3.2.1). In particular, A does not exhibit a pole at $|\boldsymbol{p}|=0$. This observation serves as a numerical evidence for the dressing functions to be continuous at this point. Thus, at $|\boldsymbol{p}|=0$ the value of A is set to

$$A(0,\omega_n):=\lim_{|\boldsymbol{p}|\to 0}A(\boldsymbol{p}^2,\omega_n). \tag{C.27}$$

[6] Also the point $|\tilde{p}|=0$ of the vacuum case has to be treated separately (cf. Eq. (C.14)).

D Symmetry w.r.t. time-like momenta

Concerning Figs. 3.2.2 and 3.2.4, the solution of the quark DSE at non-zero temperatures seems to be symmetric w.r.t. the Matsubara frequencies. This observation is the following appendix devoted to.

Using the particular gluon parametrization given in Eq. (2.5.16) and direct iteration to find a solution to the system of equations, Eq. (2.5.13), the quark dressing functions $F(|\boldsymbol{p}|, \omega_n)$, $F = A$, B, C have the symmetry

$$F(\boldsymbol{p}^2, \omega_n) = F(\boldsymbol{p}^2, -\omega_n) \ ^1. \tag{D.1}$$

The following proof assumes the initial values for the numerical iteration to be constant, i.e.

$$A_0 \equiv c_A, \quad B_0 \equiv c_B, \quad C_0 \equiv c_C \tag{D.2}$$

with c_A, c_B and c_C being arbitrary constants. This assumption is valid without loss of generality unless a particular choice of the initial values results in a solution different to the NG, WW or inverse NG solution. Those classes of solutions are discussed in Secs. 3.2.2 and 3.2.3. Since all attempts to use certain initial values failed to find fixed-points other than these three classes of solutions [2] one could assume that it exists no other solutions for direct iteration. Thus, if all choices of the initial values lead to the same solution, these choices are equivalent, in this sense, and the proof can use a particular (conveniently chosen) representative.

The proof consists of two main steps: (i) exposure of a crucial detail of Matsubara frequency distribution, and (ii) investigation of the structure of the integral equations for the dressing functions. In a third step (iii), the main steps will be concatenated.

[1] Note that this statement does not imply the relation $F(\boldsymbol{p}^2, \omega_n) = F(\boldsymbol{p}^2, \omega_{-n})$.

[2] A literature research on finding classes of solutions (for direct iteration) other than discussed in Secs. 3.2.2 and 3.2.3 turned out to the affirmative, too.

(i) Distribution of the Matsubara frequencies for fermions ($n \in \mathbb{Z}$):

$$\begin{aligned} \omega_n &= \pi T(2n+1) \\ &= -\pi T(2(-n-1)+1) \\ &= -\omega_{-n-1} \\ F(\boldsymbol{p}^2, \omega_n) &= F(\boldsymbol{p}^2, -\omega_{-n-1}). \end{aligned} \tag{D.3}$$

(ii) From the integral equations for the quark dressing functions the relation

$$F(\boldsymbol{p}^2, \omega_n) = F(\boldsymbol{p}^2, \omega_{-n-1}) \tag{D.4}$$

follows. To proof this note that the equations are each of the form

$$\begin{aligned} F(\boldsymbol{p}^2, \omega_n) &= k + \sum_{m=-\infty}^{\infty} \int \mathrm{d}^3 l \\ &\quad \times g(\{G(\boldsymbol{l}^2, \omega_n), G \in \{A, B, C\}\}, {\omega_n}^2, \omega_m \omega_n, \frac{\omega_m}{\omega_n}) \end{aligned} \tag{D.5}$$

with g being an integrable function and k is a constant. The Matsubara frequencies ω_n only appear in the combinations ${\omega_n}^2$, $\omega_m \omega_n$ and $\frac{\omega_m}{\omega_n}$. These three cases are studied in the following.

1. The dependency $\frac{\omega_m}{\omega_n}$ can be reduced to both the other dependencies by $\frac{\omega_m}{\omega_n} = \frac{\omega_m \omega_n}{{\omega_n}^2}$. Thus, $\frac{\omega_m}{\omega_n}$ does not independently occur in the equations for the quark dressing functions and can be omitted.
2. Obviously, the first case does not contradict the statement in question

   $({\omega_n}^2 = (-\omega_{-n-1})^2 = {\omega_{-n-1}}^2)$.
3. The second case can be treated by mathematical induction. Subject to the induction is the iteration step i. The induction hypothesis reads $F_i(\boldsymbol{p}^2, \omega_n) = F_i(\boldsymbol{p}^2, \omega_{-n-1})$. The crucial point is the choice of the initial values of the dressing functions, i.e. $F_i(\boldsymbol{p}^2, \omega_{-n-1}), i = 0, F_i \in \{A_i, B_i, C_i\}$. The canonical choice $F_0(\boldsymbol{p}^2, \omega_{-n-1}) \equiv 1, F \in \{A, B, C\}$ serves as the induction basis. The induction step follows [3]:

[3] Remember, the induction step reads $F_i(\boldsymbol{p}^2, \omega_n) = F_i(\boldsymbol{p}^2, \omega_{-n-1})$ by using $F_{i-1}(\boldsymbol{p}^2, \omega_n) = F_{i-1}(\boldsymbol{p}^2, \omega_{-n-1})$.

Abbreviations:

I.H.: induction hypothesis,

S.M.: symmetry of the Matsubara frequencies (cf. (i)),

S.S.: symmetry of summation (i.e. $\sum_{m=-\infty}^{+\infty} f(m) = \sum_{m=-\infty}^{+\infty} f(-m)$)].

Consider $\lim_{N\to\infty}$ for

$$\begin{aligned}
F_i(\boldsymbol{p}^2,\omega_n) &= k + \sum_{m=-N}^{N} \int \mathrm{d}^3 l \, g(\{G_{i-1}(\boldsymbol{l}^2,\omega_m),\ldots\},{\omega_n}^2,\omega_m\omega_n) \qquad \text{(D.6)}\\
&\overset{\text{I. H.}}{=} k + \sum_{m=-N}^{N} \int \mathrm{d}^3 l \, g(\{G_{i-1}(\boldsymbol{l}^2,\omega_{-m-1}),\ldots\},{\omega_n}^2,\omega_m\omega_n)\\
&\overset{\text{S. M.}}{=} k + \sum_{m=-N}^{N} \int \mathrm{d}^3 l \\
&\qquad \times g(\{G_{i-1}(\boldsymbol{l}^2,\omega_{-m-1}),\ldots\},(-\omega_{-n-1})^2,(-\omega_{-m-1})(-\omega_{-n-1}))\\
&= k + \sum_{m=-N}^{N} \int \mathrm{d}^3 l \, g(\{G_{i-1}(\boldsymbol{l}^2,\omega_{-m-1}),\ldots\},{\omega_{-n-1}}^2,\omega_{-m-1}\omega_{-n-1})\\
&\overset{\text{S. S.}}{=} k + \sum_{m=-N}^{N} \int \mathrm{d}^3 l \, g(\{G_{i-1}(\boldsymbol{l}^2,\omega_{m-1}),\ldots\},{\omega_{-n-1}}^2,\omega_{m-1}\omega_{-n-1})\\
&= k + \sum_{m=-N-1}^{N-1} \int \mathrm{d}^3 l \, g(\{G_{i-1}(\boldsymbol{l}^2,\omega_m),\ldots\},{\omega_{-n-1}}^2,\omega_m\omega_{-n-1})\\
&= F_i(\boldsymbol{p}^2,\omega_{-n-1}).
\end{aligned}$$

(iii) In conclusion,

$$F(\boldsymbol{p}^2,\omega_{-n-1}) = F(\boldsymbol{p}^2,\omega_n) = F(\boldsymbol{p}^2,-\omega_{-n-1}) \qquad \text{(D.7)}$$

and thus

$$F(\boldsymbol{p}^2,\omega_n) = F(\boldsymbol{p}^2,-\omega_n).$$

Note that for numerical issues item (ii) is the relevant point. Because of the property shown in item (ii) the functions only have to be iterated for half plus one of the frequencies as follows. At each iteration step:

1. do the integration and summation (w.r.t. $\boldsymbol{l}$ and m) at $n = 0, \ldots, N$ and

2. set the values at the remaining points ($n = 0, \ldots, N-1$) according to

$$F_i(\boldsymbol{p}^2, \omega_{-n-1}) = F_i(\boldsymbol{p}^2, \omega_n).$$

Nevertheless, this procedure invokes a further approximation. In general, the numerical iteration only takes into account a finite number of Matsubara frequencies, say from $-N$ to N. Thus, the procedure presented above neglects the N'th contribution to $F(\boldsymbol{p}^2, \omega_{-n-1})$ and adds that of index $(-N-1)$. The difference can be eliminated by:

1. carrying out the integration and summation (w.r.t. $\boldsymbol{l}$ and m) at $n = 0, \ldots, N$ and
2. setting the values at the remaining points ($n = 0, \ldots, N-1$) according to

$$\begin{aligned} F_i(\boldsymbol{p}^2, \omega_{-n-1}) \;=\; & F_i(\boldsymbol{p}^2, \omega_n) \\ & - \int \mathrm{d}^3 l \, g(\{G_{i-1}(\boldsymbol{l}^2, \omega_{-N-1}), \ldots\}, {\omega_{-n-1}}^2, \omega_{-N-1}\omega_{-n-1}) \\ & + \int \mathrm{d}^3 l \, g(\{G_{i-1}(\boldsymbol{l}^2, \omega_N), \ldots\}, {\omega_{-n-1}}^2, \omega_N\omega_{-n-1}). \end{aligned}$$

E Phase dependent chiral condensate

E.1 Symmetry

The phase dependent quark condensate as introduced in Eq. (4.2.4) is an even function w.r.t. $\varphi = \pi$

$$\langle\bar{q}q\rangle_T(\pi+\vartheta) = \langle\bar{q}q\rangle_T(\pi-\vartheta) \tag{E.1}$$

with $\varphi \in (0,\, \pi)$. A proof consists of three main steps:

(i) $\omega_n(\pi+\vartheta) = -\omega_{-n-1}(\pi-\vartheta)$,

(ii) $F(\boldsymbol{p}^2, \omega_n(\pi+\vartheta)) = F(\boldsymbol{p}^2, \omega_{-n-1}(\pi-\vartheta)), F \in \{A, B, C\}$ by induction,

(iii) $\langle\bar{q}q\rangle_T(\pi+\vartheta) = \langle\bar{q}q\rangle_T(\pi-\vartheta)$.

The functions' argument $\boldsymbol{p}^2$ will be omitted.

Step (iii): Consider $\lim_{N\to\infty}$ for

$$\begin{aligned}
&-\frac{\langle\bar{q}q\rangle_T(\pi+\vartheta)}{4\,N_C\,T} \\
&= \sum_{n=-N}^{N}\int\frac{\mathrm{d}^3p}{(2\pi)^3}\,\frac{B(\omega_n(\pi+\vartheta))}{\boldsymbol{p}^2A^2(\omega_n(\pi+\vartheta)) + \omega_n^2(\pi+\vartheta)C^2(\omega_n(\pi+\vartheta)) + B^2(\omega_n(\pi+\vartheta))} \\
&\overset{(1.)}{=} \sum_{n=-N}^{N}\int\frac{\mathrm{d}^3p}{(2\pi)^3}\,\frac{B(\omega_n(\pi+\vartheta))}{\boldsymbol{p}^2A^2(\omega_n(\pi+\vartheta)) + (-\omega_{-n-1}^2(\pi-\vartheta))C^2(\omega_n(\pi+\vartheta)) + B^2(\omega_n(\pi+\vartheta))} \\
&\overset{(2.)}{=} \sum_{n=-N}^{N}\int\frac{\mathrm{d}^3p}{(2\pi)^3}\,\frac{B(\omega_{-n-1}(\pi-\vartheta))}{\boldsymbol{p}^2A^2(\omega_{-n-1}(\pi-\vartheta)) + \omega_{-n-1}^2(\pi-\vartheta)C^2(\omega_{-n-1}(\pi-\vartheta)) + B^2(\omega_{-n-1}(\pi-\vartheta))} \\
&\overset{(\mathrm{S.S.})}{=} \sum_{n=-N}^{N}\int\frac{\mathrm{d}^3p}{(2\pi)^3}\,\frac{B(\omega_{n-1}(\pi-\vartheta))}{\boldsymbol{p}^2A^2(\omega_{n-1}(\pi-\vartheta)) + \omega_{n-1}^2(\pi-\vartheta)C^2(\omega_{n-1}(\pi-\vartheta)) + B^2(\omega_{n-1}(\pi-\vartheta))} \\
&= \sum_{n=-N-1}^{N-1}\int\frac{\mathrm{d}^3p}{(2\pi)^3}\,\frac{B(\omega_n(\pi-\vartheta))}{\boldsymbol{p}^2A^2(\omega_n(\pi-\vartheta)) + \omega_n^2(\pi-\vartheta)C^2(\omega_n(\pi-\vartheta)) + B^2(\omega_n(\pi-\vartheta))} \\
&= -\frac{\langle\bar{q}q\rangle_T(\pi-\vartheta)}{4\,N_C\,T}.
\end{aligned} \tag{E.2}$$

Step (i):

$$\begin{aligned}\omega_n(\pi+\vartheta) &= \pi T\left(2n+\frac{(\pi+\vartheta)}{\pi}\right) \\ &= -\pi T\left(2(-n-1)+1-\frac{\vartheta}{\pi}\right) \\ &= -\omega_{-n-1}(\pi-\vartheta).\end{aligned} \tag{E.3}$$

Step (ii) resembles the induction of the non-shifted case (cf. App. D):

The equations are each of the following form:

$$\begin{aligned}&F(\boldsymbol{p}^2,\omega_n(\pi+\vartheta)) \\ &= k_F+\sum_{m=-\infty}^{\infty}\int_{l_3}\mathrm{d}^3 l_3 g\left(\left\{G(\boldsymbol{l}^2,\omega_n(\pi+\vartheta)), G\in\{A,B,C\}\right\},\right. \\ &\qquad\left.\omega_n(\pi+\vartheta)^2,\omega_m(\pi+\vartheta)\omega_n(\pi+\vartheta),\frac{\omega_m(\pi+\vartheta)}{\omega_n}(\pi+\vartheta)\right)\end{aligned} \tag{E.4}$$

with g being an integrable function and k_F is a constant. $\omega_n(\pi+\vartheta)$ only appears as $\omega_n^2(\pi+\vartheta)$, $\omega_m(\pi+\vartheta)\omega_n(\pi+\vartheta)$ and $\omega_m(\pi+\vartheta)\,/\,\omega_n(\pi+\vartheta)$. The fraction $\omega_m\,/\,\omega_n$ can be reduced to both the other cases by $\omega_m\,/\,\omega_n=\omega_m\omega_n\,/\,\omega_n^2$. This term will be omitted from now on. The induction basis is the symmetric choice of the iteration initial values w.r.t. $\omega_n(\pi+\vartheta)$ (cf. App. D for a justification of restricting the choice of initial values). Consider $\lim_{N\to\infty}$ for

$$\begin{aligned}&F_{i,N}(\boldsymbol{l}^2,\omega_n(\pi+\vartheta))-k_F \\ &= \sum_{m=-N}^{N} g(\{G_{i-1}(\boldsymbol{l}^2,\omega_n(\pi+\vartheta))\},\omega_n^2(\pi+\vartheta),\omega_m(\pi+\vartheta)\omega_n(\pi+\vartheta)) \\ &\overset{\text{(I.H.)}}{=} \sum_{m=-N}^{N} g(\{G_{i-1}(\boldsymbol{l}^2,\omega_{-n-1}(\pi-\vartheta))\},\omega_n^2(\pi+\vartheta),\omega_m(\pi+\vartheta)\omega_n(\pi+\vartheta)) \\ &\overset{\text{(S.M.)}}{=} \sum_{m=-N}^{N} g(\{G_{i-1}(\boldsymbol{l}^2,\omega_{-n-1}(\pi-\vartheta))\},(-\omega_{-n-1}^2(\pi-\vartheta)),(-\omega_{-m-1}(\pi-\vartheta))(-\omega_{-n-1}(\pi-\vartheta))) \\ &= \sum_{m=-N}^{N} g(\{G_{i-1}(\boldsymbol{l}^2,\omega_{-n-1}(\pi-\vartheta))\},(\omega_{-n-1}^2(\pi-\vartheta)),(\omega_{-m-1}(\pi-\vartheta))(\omega_{-n-1}(\pi-\vartheta))) \\ &\overset{\text{(S.S.)}}{=} \sum_{m=-N}^{N} g(\{G_{i-1}(\boldsymbol{l}^2,\omega_{-n-1}(\pi-\vartheta))\},(\omega_{-n-1}^2(\pi-\vartheta)),(\omega_{m-1}(\pi-\vartheta))(\omega_{-n-1}(\pi-\vartheta))) \\ &= \sum_{m=-N-1}^{N-1} g(\{G_{i-1}(\boldsymbol{l}^2,\omega_{-n-1}(\pi-\vartheta))\},(\omega_{-n-1}^2(\pi-\vartheta)),(\omega_{m}(\pi-\vartheta))(\omega_{-n-1}(\pi-\vartheta))) \\ &= F_{i,N}(\boldsymbol{l}^2,\omega_{-n-1}(\pi-\vartheta))-k_F.\end{aligned} \tag{E.5}$$

E.2 Periodicity

The phase dependent chiral condensate exhibits a 2π-symmetry

$$\langle\bar{q}q\rangle_T(\varphi+2\pi)=\langle\bar{q}q\rangle_T(\varphi). \tag{E.6}$$

This property originates from the infinite summation over the Matsubara frequencies. First, note

$$\omega_n(\varphi+2\pi)=\pi T\left(2n+\frac{\varphi+2\pi}{\pi}\right)=\pi T\left(2(n+1)+\frac{\varphi}{\pi}\right)=\omega_{n+1}(\varphi). \tag{E.7}$$

Consider $N\to\infty$ for

$$\begin{aligned}\langle\bar{q}q\rangle_T(\varphi+2\pi) &= N_C\,T\sum_{n=-N}^{N}\int\frac{\mathrm{d}^3p}{(2\pi)^3}\,\mathrm{tr}_D[S(\boldsymbol{p},\omega_n(\varphi+2\pi))] \\ &= N_C\,T\sum_{n=-N+1}^{N+1}\int\frac{\mathrm{d}^3p}{(2\pi)^3}\,\mathrm{tr}_D[S(\boldsymbol{p},\omega_n(\varphi))] \\ &= \langle\bar{q}q\rangle_T(\varphi).\end{aligned} \tag{E.8}$$

E.3 Center transformation

After discussing necessary properties of the phase dependent chiral condensate, the center-transformed dual condensate has the form:

$$\begin{aligned}{}^{z(k)}\Sigma_n &= \int_0^{2\pi}\frac{\mathrm{d}\varphi}{2\pi}e^{-i\varphi n}\langle\bar{q}q\rangle_T(\varphi+2\pi k/N_C) \\ &= \int_{0+2\pi k/N_C}^{2\pi+2\pi k/N_C}\frac{\mathrm{d}\varphi}{2\pi}e^{-i(\varphi-2\pi k/N_C)n}\langle\bar{q}q\rangle_T(\varphi) \\ &= e^{i\,2\pi k/N_C\cdot n}\int_{0+2\pi k/N_C}^{2\pi+2\pi k/N_C}\frac{\mathrm{d}\varphi}{2\pi}e^{-i\,\varphi n}\langle\bar{q}q\rangle_T(\varphi) \\ &= e^{i\,2\pi k/N_C\cdot n}\int_0^{2\pi}\frac{\mathrm{d}\varphi}{2\pi}e^{-i\,\varphi n}\langle\bar{q}q\rangle_T(\varphi) \\ &= z(k)^n\Sigma_n.\end{aligned} \tag{E.9}$$

In the last but one step, periodicity of $\langle\bar{q}q\rangle_T$ enters as follows:

$$\begin{aligned}&\int_{0+2\pi k/N_C}^{2\pi+2\pi k/N_C}\frac{\mathrm{d}\varphi}{2\pi}e^{-i\,\varphi n}\langle\bar{q}q\rangle_T(\varphi) \\ &= \int_{2\pi k/N_C}^{2\pi}\frac{\mathrm{d}\varphi}{2\pi}e^{-i\,\varphi n}\langle\bar{q}q\rangle_T(\varphi)+\int_{2\pi}^{2\pi+2\pi k/N_C}\frac{\mathrm{d}\varphi}{2\pi}e^{-i\,\varphi n}\langle\bar{q}q\rangle_T(\varphi) \\ &= \int_{2\pi k/N_C}^{2\pi}\frac{\mathrm{d}\varphi}{2\pi}e^{-i\,\varphi n}v(\varphi)+\int_0^{2\pi k/N_C}\frac{\mathrm{d}\varphi}{2\pi}e^{-i\,(\varphi+2\pi)n}\langle\bar{q}q\rangle_T(\varphi+2\pi)\end{aligned} \tag{E.10}$$

$$
\begin{aligned}
&= \int_{2\pi k/N_C}^{2\pi} \frac{\mathrm{d}\varphi}{2\pi} e^{-i\,\varphi n} \langle \bar{q}q \rangle_T(\varphi) + \int_0^{2\pi k/N_C} \frac{\mathrm{d}\varphi}{2\pi} e^{-i\,\varphi n} \langle \bar{q}q \rangle_T(\varphi) \\
&= \int_0^{2\pi} \frac{\mathrm{d}\varphi}{2\pi} e^{-i\,\varphi n} \langle \bar{q}q \rangle(\varphi).
\end{aligned}
$$

F Numerical approximations

For reasons of clarity this section presents the DSEs for the dressing functions in the numerical approximated form, i.e. with the infinite range of the momentum integration $p \in [0, \infty)$ mapped to the interval $[-1, 1)$ and with the integrals approximated by means of the Gaussian quadrature (Gauss-Legendre and Gauss-Chebychev). The discretised equations are implemented in a Fortran code using double precision arithmetic.

F.1 Vacuum

Using Eqs. (2.4.7, 3.1.2, 3.1.4) the integral measure in Eq. (2.4.6) is approximated by

$$\int \frac{\mathrm{d}^4 l}{(2\pi)^4} f(l) \approx \frac{{p_0}^4}{2\pi^3} \sum_{i=1}^{n^{\mathrm{le}}} \sum_{j=1}^{n^{\mathrm{ch}}} \frac{(1+x_i)^3}{(1-x_i)^5}\, \alpha_i^{\mathrm{le}}\, \alpha_j^{\mathrm{ch}}\, f(\lambda(x_i), t_j) \tag{F.1}$$

with x_i and t_j being the nodes of the Gauss-Legendre and Gauss-Chebychev quadrature, and α_i^{le} and α_j^{ch} denoting the corresponding weights. Defining $\kappa(x_i)$ in the manner of Eq. (3.1.3) and introducing the notations

$$\begin{aligned} &\lambda_i := \lambda(x_i), \quad \lambda_k := \kappa(x_k), \\ &A(\lambda_i) := A_i, \quad B(\lambda_i) := B_i \ {}^{1} \end{aligned} \tag{F.2}$$

the approximation of Eq. (2.4.6) reads

$$\begin{aligned} A_k &\approx 1 + \frac{2{p_0}^4}{3\pi^3} \sum_{i=1}^{n^{\mathrm{le}}} \sum_{j=1}^{n^{\mathrm{ch}}} \frac{(1+x_i)^3}{(1-x_i)^5}\, \alpha_i^{\mathrm{le}}\, \alpha_j^{\mathrm{ch}} \\ &\quad \times \frac{\Delta_D(\lambda_k, \lambda_i, t_j)}{\lambda_i^2 A_i^2 + B_i^2} \frac{\lambda_i}{\lambda_k} \left(t_j + 2 \frac{(\lambda_k - \lambda_i t_j)(\lambda_k t_j - \lambda_i)}{\lambda_k^2 + \lambda_i^2 - 2\lambda_k \lambda_i t_j} \right) A_i, \\ B_k &\approx m + \frac{2{p_0}^4}{\pi^3} \sum_{i=1}^{n^{\mathrm{le}}} \sum_{j=1}^{n^{\mathrm{ch}}} \frac{(1+x_i)^3}{(1-x_i)^5}\, \alpha_i^{\mathrm{le}}\, \alpha_j^{\mathrm{ch}}\, \frac{\Delta_D(\lambda_k, \lambda_i, t_j)}{\lambda_i^2 A_i^2 + B_i^2} B_i \end{aligned} \tag{F.3}$$

[1] The indices k and i of A and B denote the position in the (discretized) arrays of these functions. These indices are not to be confused with the iteration index which is introduced in the context of finding a solution to the quark DSE (cf. Eq. (3.1.6)).

with

$$\Delta_D(\lambda_k,\lambda_i,t_j) = 4\pi^2 D \frac{\lambda_k^2+\lambda_i^2-2\lambda_k\lambda_l t_j}{\omega^6} e^{-\frac{\lambda_k^2+\lambda_i^2-2\lambda_k\lambda_l t_j}{\omega^2}}. \tag{F.4}$$

Writing the quark DSEs in this form reveals the scaling of computing time $t^{\mathrm{comp},1}$ w.r.t. the discretisation parameters for one iteration step:

$$t^{\mathrm{comp},1} = \mathcal{O}(n^{\mathrm{le}^2} n^{\mathrm{ch}}). \tag{F.5}$$

F.2 Non-zero temperatures

With regard to Eqs. (2.5.15) and (3.2.1) and taking into account the truncation of the infinite summation over the Matsubara frequencies symmetrically at $\hat{n}$ as discussed in Sec. 3.2.1 the integration and summation of Eq. (2.5.13) is approximated by

$$\sum_{m=-\infty}^{\infty} \int \frac{\mathrm{d}^3 l}{(2\pi)^3} f(l,\omega_m) \approx \frac{2\,{p_0}^3}{(2\pi)^2} \sum_{m=-\hat{n}}^{\hat{n}} \sum_{i=1}^{n_\lambda} \sum_{j=1}^{n_t} \frac{(1+x_i)^2}{(1-x_i)^4}\,\alpha_i\,\alpha_j\, f(\lambda(x_i),t_j,\omega_m) \tag{F.6}$$

with x_i and t_j being nodes of the Gauss-Legendre quadrature and α_i as well as α_j denoting the corresponding weights. Using $\sqrt{\boldsymbol{p}^2}(x_i) = \kappa(x_i)$ and introducing

$$\begin{aligned} &\lambda_i := \lambda(x_i), \quad \lambda_k := \kappa(x_k), \\ &A(\lambda_i,\omega_m) := A_{im}, \quad B(\lambda_i,\omega_m) := B_{im} \end{aligned} \tag{F.7}$$

Eq. (2.5.17) is approximated by

$$\begin{aligned} A_{kn} &= 1 + \frac{T}{3\pi^2} 2\,{p_0}^3 \sum_{m=-\hat{n}}^{\hat{n}} \sum_{i=1}^{n_\lambda} \sum_{j=1}^{n_t} \frac{(1+x_i)^2}{(1-x_i)^4}\,\alpha_i\,\alpha_j \Delta_H(\lambda_k,\lambda_i,t_j,\Omega_{nm}) \\ &\quad \times \left[\left(\frac{t_j\lambda_i}{\lambda_k} + \frac{2\left(\lambda_k\lambda_i t_j - \lambda_i^2\right)\left(1-\frac{t_j\lambda_i}{\lambda_k}\right)}{\lambda_k^2+\lambda_i^2-2\lambda_k\lambda_i t_j+\Omega_{nm}} \right) \frac{A_{im}}{\lambda_i^2 A_{im}^2 + {\omega_m}^2 C_{im}^2 + B_{im}^2} \right. \\ &\quad \left. + \frac{\Omega_{nm} 2\left(1-\frac{t_j\lambda_i}{\lambda_k}\right)\omega_m}{\lambda_k^2+\lambda_i^2-2\lambda_k\lambda_i t_j+\Omega_{nm}} \frac{C_{im}}{\lambda_i^2 A_{im}^2 + {\omega_m}^2 C_{im}^2 + B_{im}^2} \right], \\ C_{kn} &= 1 + \frac{1}{\omega_n}\frac{T}{3\pi^2} 2\,{p_0}^3 \sum_{m=-\hat{n}}^{\hat{n}} \sum_{i=1}^{n_\lambda} \sum_{j=1}^{n_t} \frac{(1+x_i)^2}{(1-x_i)^4}\,\alpha_i\,\alpha_j \Delta_H(\lambda_k,\lambda_i,t_j,\Omega_{nm}) \\ &\quad \times \left[\frac{\Omega_{nm} 2\left(\lambda_k\lambda_i t_j - \lambda_i^2\right)}{\lambda_k^2+\lambda_i^2-2\lambda_k\lambda_i t_j+\Omega_{nm}} \frac{A_{im}}{\lambda_i^2 A_{im}^2 + {\omega_m}^2 C_{im}^2 + B_{im}^2} \right. \\ &\quad \left. + \left(\omega_m + \frac{2\Omega_{nm}^2\omega_m}{\lambda_k^2+\lambda_i^2-2\lambda_k\lambda_i t_j+\Omega_{nm}} \right) \frac{C_{im}}{\lambda_i^2 A_{im}^2 + {\omega_m}^2 C_{im}^2 + B_{im}^2} \right], \end{aligned} \tag{F.8}$$

$$B_{kn} = m + \frac{T}{\pi^2} 2\,{p_0}^3 \sum_{m=-\hat{n}}^{\hat{n}} \sum_{i=1}^{n_\lambda} \sum_{j=1}^{n_t} \frac{(1+x_i)^2}{(1-x_i)^4}\,\alpha_i\,\alpha_j\,\Delta_H(\lambda_k,\lambda_i,t_j,\Omega_{nm}) \times \left[\frac{B_{im}}{\lambda_i^2 A_{im}^2 + {\omega_m}^2 C_{im}^2 + B_{im}^2}\right]$$

with

$$\Delta_H(\lambda_k,\lambda_i,t_j,\Omega_{nm}) = 4\pi^2 D \frac{\lambda_k^2+\lambda_i^2-2\lambda_k\lambda_i t_j+\Omega_{nm}}{\omega^6} e^{-\frac{\lambda_k^2+\lambda_i^2-2\lambda_k\lambda_i t_j+\Omega_{nm}}{\omega^2}}. \tag{F.9}$$

This representation of the quark DSE at finite temperatures simplifies the determination of the computing time for one iteration $t_T^{\mathrm{comp},1}$ w.r.t. the grid parameters. Using equal numbers of Gauss-Legendre nodes for both the integrations over the angle the absolute value of the momentum, $n^{\mathrm{le}} = n^\lambda = n^t$, the computing time scales like:

$$t_T^{\mathrm{comp},1} = \mathcal{O}({n^\lambda}^2 n^t \hat{n}^2) = \mathcal{O}({n^{\mathrm{le}}}^3 \hat{n}^2). \tag{F.10}$$

G Spectral representation

This appendix explicitly carries out the decomposition of the quark propagator in the chiral limit at temperatures higher than the critical temperature of chiral symmetry restoration. Subsequently, the two-pole ansatz given in Sec. 4.3 is used to establish an expression d_+ to be minimized by the fitting routine *fmin* of the *scipy.optimize* package.

Taking into account the discussion of Sec. 4.1 the inverse quark propagator in the chiral symmetric phase has the form

$$S^{-1}(\boldsymbol{p},\omega_n) \;= i\boldsymbol{\gamma}\cdot\boldsymbol{p}A(\boldsymbol{p},\omega_n) + i\gamma_4\omega_n C(\boldsymbol{p},\omega_n). \tag{G.1}$$

It can be decomposed to achieve two symmetric parts (arguments of the quark propagator and the dressing functions suppressed)

$$\begin{aligned}
S^{-1} &= \quad i\boldsymbol{\gamma}\cdot\boldsymbol{p}A + i\gamma_4\omega_n C, \qquad (G.2)\\
S &= -i\,\frac{\boldsymbol{\gamma}\cdot\boldsymbol{p}A + \gamma_4\omega_n C}{\boldsymbol{p}^2A^2+\omega_n^2C^2}\\
&= -i\,\frac{\boldsymbol{\gamma}\cdot\boldsymbol{p}A + \gamma_4\omega_n C + \frac{1}{2}i\,\gamma_4|\boldsymbol{p}|A - \frac{1}{2}i\,\gamma_4|\boldsymbol{p}|A + \frac{1}{2}\frac{\boldsymbol{\gamma p}}{i|\boldsymbol{p}|}\omega_n C - \frac{1}{2}\frac{\boldsymbol{\gamma p}}{i|\boldsymbol{p}|}\omega_n C}{(i\,|\boldsymbol{p}|A+\omega_n C)(-i\,|\boldsymbol{p}|A+\omega_n C)}\\
&= -i\,\frac{\frac{1}{2}\gamma_4(\omega_n C + i\,|\boldsymbol{p}|A) + \frac{1}{2}\gamma_4(\omega_n C - i\,|\boldsymbol{p}|A)}{(i\,|\boldsymbol{p}|A+\omega_n C)(-i\,|\boldsymbol{p}|A+\omega_n C)}\\
&\quad -i\,\frac{\frac{1}{2}\frac{\boldsymbol{\gamma p}}{i|\boldsymbol{p}|}(i\,|\boldsymbol{p}|A+\omega_n C) + \frac{1}{2}\frac{\boldsymbol{\gamma p}}{i|\boldsymbol{p}|}(i\,|\boldsymbol{p}|A-\omega_n C)}{(i\,|\boldsymbol{p}|A+\omega_n C)(-i\,|\boldsymbol{p}|A+\omega_n C)}\\
&= -i\,\frac{\frac{1}{2}\gamma_4(\omega_n C + i\,|\boldsymbol{p}|A) + \frac{1}{2}\frac{\boldsymbol{\gamma p}}{i|\boldsymbol{p}|}(i\,|\boldsymbol{p}|A+\omega_n C)}{(i\,|\boldsymbol{p}|A+\omega_n C)(-i\,|\boldsymbol{p}|A+\omega_n C)}\\
&\quad -i\,\frac{\frac{1}{2}\gamma_4(\omega_n C - i\,|\boldsymbol{p}|A) + \frac{1}{2}\frac{\boldsymbol{\gamma p}}{i|\boldsymbol{p}|}(i\,|\boldsymbol{p}|A-\omega_n C)}{(i\,|\boldsymbol{p}|A+\omega_n C)(-i\,|\boldsymbol{p}|A+\omega_n C)}\\
&= -i\,\frac{\frac{1}{2}\gamma_4 + \frac{1}{2}\frac{\boldsymbol{\gamma p}}{i|\boldsymbol{p}|}}{(-i\,|\boldsymbol{p}|A+\omega_n C)} - i\,\frac{\frac{1}{2}\gamma_4 - \frac{1}{2}\frac{\boldsymbol{\gamma p}}{i|\boldsymbol{p}|}}{(i\,|\boldsymbol{p}|A+\omega_n C)}\\
&= \frac{1}{|\boldsymbol{p}|A+i\,\omega_n C}\frac{\gamma_4 - \frac{i\,\boldsymbol{\gamma p}}{|\boldsymbol{p}|}}{2} + \frac{1}{-|\boldsymbol{p}|A+i\,\omega_n C}\frac{\gamma_4 + \frac{i\,\boldsymbol{\gamma p}}{|\boldsymbol{p}|}}{2}.
\end{aligned}$$

Extraction of γ_4 leads to the expression

$$\begin{aligned} S &= \frac{1}{|\boldsymbol{p}|A + i\,\omega_n C}\frac{1+\frac{i\,\gamma_4\boldsymbol{\gamma}\boldsymbol{p}}{|\boldsymbol{p}|}}{2}\gamma_4 + \frac{1}{-|\boldsymbol{p}|A + i\,\omega_n C}\frac{1-\frac{i\,\gamma_4\boldsymbol{\gamma}\boldsymbol{p}}{|\boldsymbol{p}|}}{2}\gamma_4 \\ &= S_-(\boldsymbol{p},\omega_n)P_-(\boldsymbol{p})\gamma_4 + S_+(\boldsymbol{p},\omega_n)P_+(\boldsymbol{p})\gamma_4 \end{aligned} \tag{G.3}$$

involving the projectors

$$\begin{aligned} P_-(\boldsymbol{p}) &:= \frac{1}{2}\left(1 + i\,\frac{\gamma_4\boldsymbol{\gamma}\boldsymbol{p}}{|\boldsymbol{p}|}\right), \\ P_+(\boldsymbol{p}) &:= \frac{1}{2}\left(1 - i\,\frac{\gamma_4\boldsymbol{\gamma}\boldsymbol{p}}{|\boldsymbol{p}|}\right) \end{aligned} \tag{G.4}$$

and the two dressings

$$\begin{aligned} S_-(\boldsymbol{p},\omega_n) &:= \frac{1}{|\boldsymbol{p}|A + i\,\omega_n C} = -\frac{i\,\omega_n C - |\boldsymbol{p}|A}{|\boldsymbol{p}|^2A^2 + \omega_n^2 C^2}, \\ S_+(\boldsymbol{p},\omega_n) &:= \frac{1}{-|\boldsymbol{p}|A + i\,\omega_n C} = -\frac{i\,\omega_n C + |\boldsymbol{p}|A}{|\boldsymbol{p}|^2A^2 + \omega_n^2 C^2}. \end{aligned} \tag{G.5}$$

Their spectral representations read:

$$\begin{aligned} S_-(\boldsymbol{p},\omega_n) &=: \int_{-\infty}^{\infty}\frac{\mathrm{d}\omega'}{2\pi}\frac{\rho_-(\boldsymbol{p},\omega')}{i\omega_n - \omega'}, \\ S_+(\boldsymbol{p},\omega_n) &=: \int_{-\infty}^{\infty}\frac{\mathrm{d}\omega'}{2\pi}\frac{\rho_+(\boldsymbol{p},\omega')}{i\omega_n - \omega'} \end{aligned} \tag{G.6}$$

with $\rho_-(\boldsymbol{p},\omega')$ and $\rho_+(\boldsymbol{p},\omega')$ denoting the respective spectral densities. Using the two-pole ansatz

$$\rho_+(\boldsymbol{p},\omega) = 2\pi[Z_1\delta(\omega - E_1) + Z_2\delta(\omega + E_2)] \tag{G.7}$$

the respective dressing S_+^{tp} has the form

$$\begin{aligned} S_+^{\mathrm{tp}}(\boldsymbol{p},\omega_n) &:= \int_{-\infty}^{\infty}\frac{\mathrm{d}\omega'}{2\pi}\frac{2\pi[Z_1\delta(\omega' - E_1) + Z_2\delta(\omega' + E_2)]}{i\omega_n - \omega'} \\ &= \int_{-\infty}^{\infty}\mathrm{d}\omega'\frac{Z_1\delta(\omega' - E_1)}{i\omega_n - \omega'} + \int_{-\infty}^{\infty}\mathrm{d}\omega'\frac{Z_2\delta(\omega' + E_2)}{i\omega_n - \omega'} \\ &= \frac{Z_1}{i\omega_n - E_1} + \frac{Z_2}{i\omega_n + E_2} \\ &= \frac{Z_1(-i\omega_n - E_1)}{{\omega_n}^2 + {E_1}^2} + \frac{Z_2(-i\omega_n + E_2)}{{\omega_n}^2 + {E_2}^2} \end{aligned} \tag{G.8}$$

$$= -i\omega_n \left(\frac{Z_1}{{\omega_n}^2 + {E_1}^2} + \frac{Z_2}{{\omega_n}^2 + {E_2}^2} \right) + \frac{-Z_1 E_1}{{\omega_n}^2 + {E_1}^2} + \frac{Z_2 E_2}{{\omega_n}^2 + {E_2}^2}.$$

The superscript tp stands for "two-pole". One possibility to approximate the quark propagator extracted from the Dyson-Schwinger equations by the propagator resulting from the two pole ansatz is to minimize the mean squared deviation d_+, i.e.

$$\begin{aligned}
d_+(\boldsymbol{p}) &:= \frac{1}{N+1} \sum_{n=0}^{N} \left| S_+^{\mathrm{tp}}(\boldsymbol{p}, \omega_n) - S_+(\boldsymbol{p}, \omega_n) \right|^2 \qquad \text{(G.9)} \\
&= \frac{1}{N+1} \sum_{n=0}^{N} \left| \frac{Z_1}{i\omega_n - E_1} + \frac{Z_2}{i\omega_n + E_2} - \left(\frac{1}{-|\boldsymbol{p}|A + i\,\omega_n C} \right) \right|^2 \\
&= \frac{1}{N+1} \sum_{n=0}^{N} \left| -i\omega_n \left(\frac{Z_1}{{\omega_n}^2 + {E_1}^2} + \frac{Z_2}{{\omega_n}^2 + {E_2}^2} \right) + i\,\omega_n \frac{C}{|\boldsymbol{p}|^2 A^2 + \omega_n^2 C^2} \right. \\
&\qquad \left. + \frac{-Z_1 E_1}{{\omega_n}^2 + {E_1}^2} + \frac{Z_2 E_2}{{\omega_n}^2 + {E_2}^2} + \frac{|\boldsymbol{p}|A}{|\boldsymbol{p}|^2 A^2 + \omega_n^2 C^2} \right|^2 \\
&= \frac{1}{N+1} \sum_{n=0}^{N} {\omega_n}^2 \left(-\frac{Z_1}{{\omega_n}^2 + {E_1}^2} - \frac{Z_2}{{\omega_n}^2 + {E_2}^2} + \frac{C}{|\boldsymbol{p}|^2 A^2 + \omega_n^2 C^2} \right)^2 \\
&\qquad + \left(\frac{-Z_1 E_1}{{\omega_n}^2 + {E_1}^2} + \frac{Z_2 E_2}{{\omega_n}^2 + {E_2}^2} + \frac{|\boldsymbol{p}|A}{|\boldsymbol{p}|^2 A^2 + \omega_n^2 C^2} \right)^2 .
\end{aligned}$$

The index n runs only over positive values and zero. The summation is truncated at N [1]. Since the dressing functions are symmetric w.r.t. the frequencies (cf. App. D), summing symmetrically, i.e. taking into account also the negative indices, gives the same measure d_+ [2].

G.1 Fit quality

In order to create confidence in the applied fit function this section compares the data obtained from the DSE with the results of the fit. Figure G.1 shows the minimized quantity d_+ normalized to the data obtained from the quark DSE, i.e. normalized to $|S_+^{\mathrm{DSE}}|^2/(N+1)$. Figure G.2 provides a qualitative picture of the fit quality.

[1] The contribution of frequencies with large indices vanishes in the limit $N \to \infty$ (cf. generalized harmonic series).

[2] For the summation starting at $n_{min} = -N-1$ one has

$$\frac{1}{2(N+1)} \sum_{n=-N-1}^{N} \left| S_+^{\mathrm{tp}}(\boldsymbol{p}, \omega_n) - S_+(\boldsymbol{p}, \omega_n) \right|^2 = \frac{2}{2(N+1)} \sum_{n=0}^{N} \left| S_+^{\mathrm{tp}}(\boldsymbol{p}, \omega_n) - S_+(\boldsymbol{p}, \omega_n) \right|^2 = d_+.$$

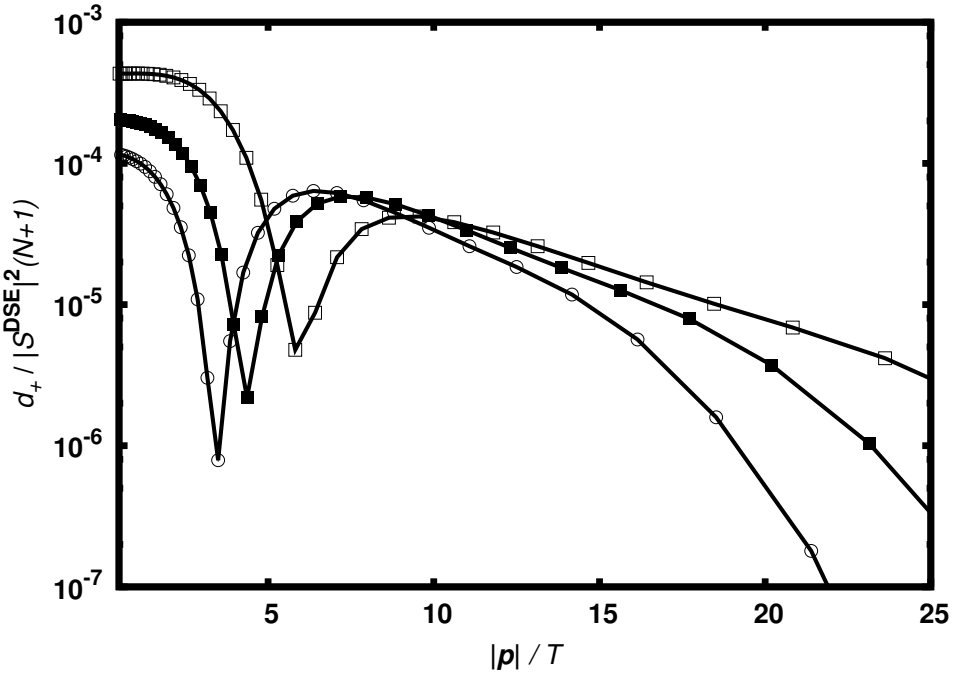

Figure G.1: Minimized d_+ normalized to $|S_+^{\mathrm{DSE}}|^2/(N+1)$ for the temperatures $T = 1.5\,T_c$ (empty squares), $T = 2.0\,T_c$ (filled squares), $T = 2.5\,T_c$ (circles).

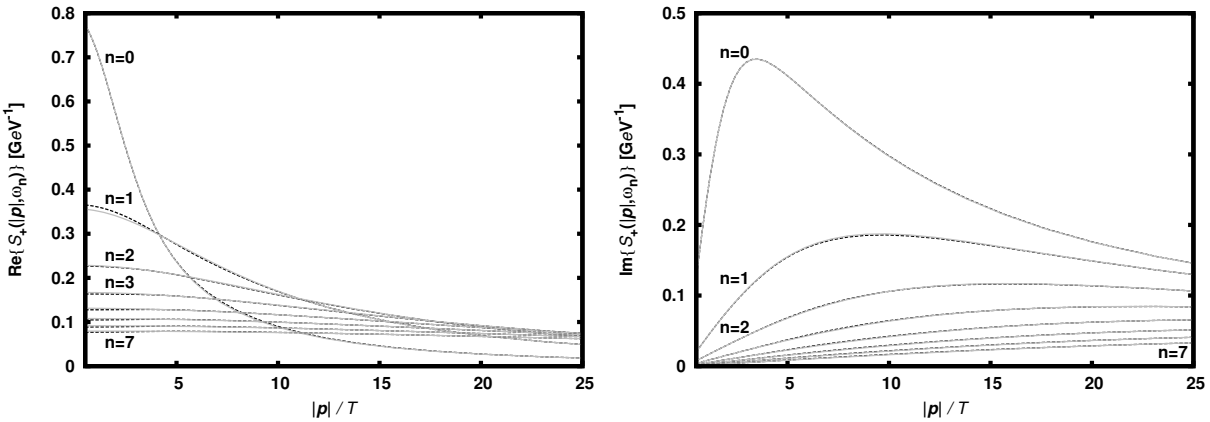

(a) Real part of S_+. **(b)** Imaginary part of S_+.

Figure G.2: Comparison of the fit (dashed black lines) with the data obtained from the quark DSE (solid grey lines) at $T = 2.0\,T_c$ for the first eight Matsubara frequencies.

H Truncation of the summation over the Matsubara frequencies

This appendix compares the solutions of the quark DSE, Eq. (2.5.17), obtained by taking into account two different numbers of Matsubara frequencies. In Fig. H.1 the dressing functions at $T = 30\,\mathrm{M}e\mathrm{V}$ are displayed for zero momentum and various frequencies. Omitting higher

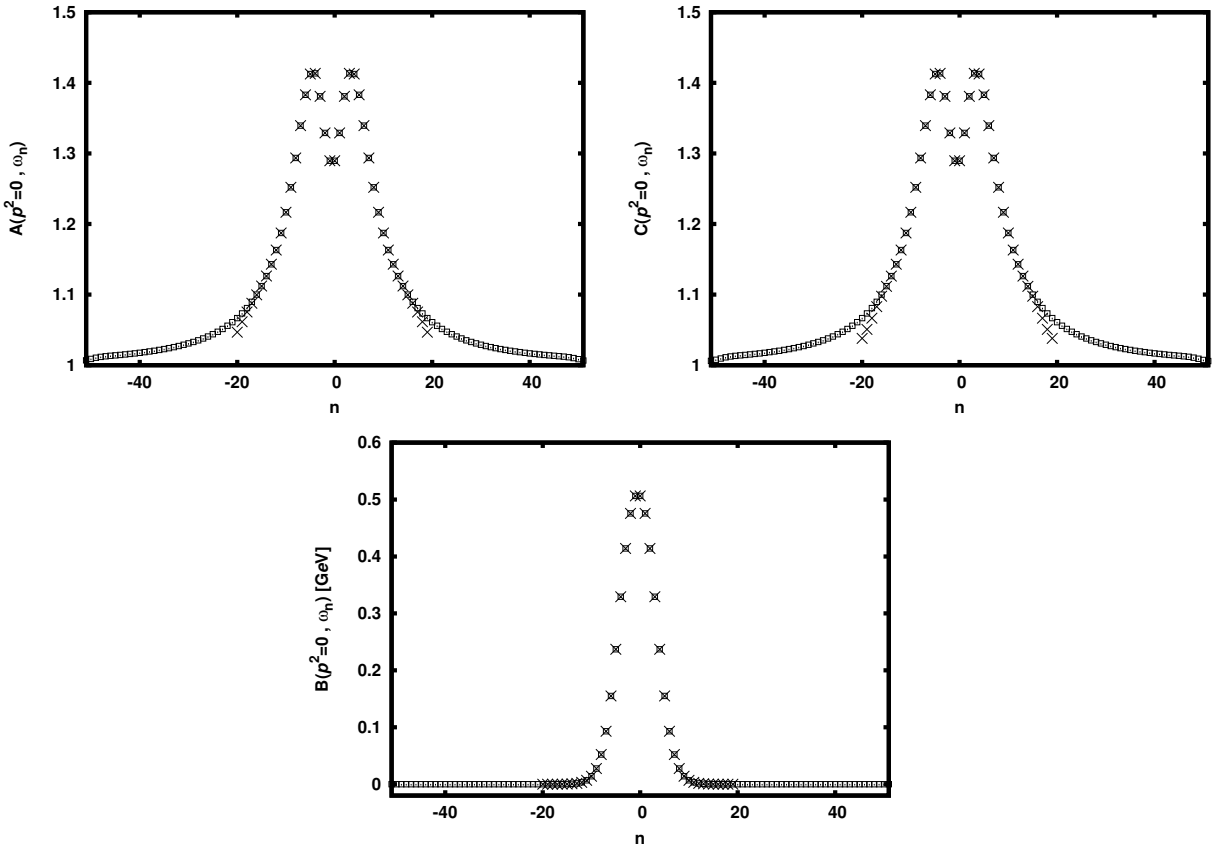

Figure H.1: Quark dressing functions at $T = 30\,\mathrm{M}e\mathrm{V}$ as a solution of Eq. (2.5.17) shown for various Matsubara frequencies ω_n. Dotted squares indicate the solution obtained with $\hat{n} = 51$, and crosses correspond to the solution with $\hat{n} = 20$ and the omission of ω_{20}.

frequencies has minor effect on the solutions at low frequencies. The dressing functions

A and C are underestimated at the remotest frequencies for taking less frequencies into account.

I T_C in dependence on the model parameters

Figure I.1 presents the critical temperature T_c of chiral symmetry restoration in dependence on the interaction strength D and the interaction range ω. The given contour lines are approximated in order to achieve smooth curves [1], because the used temperature resolution of $\Delta T = 1\,\mathrm{MeV}$ does not cope with the weak dependency of T_c observed in the center of the shown section.

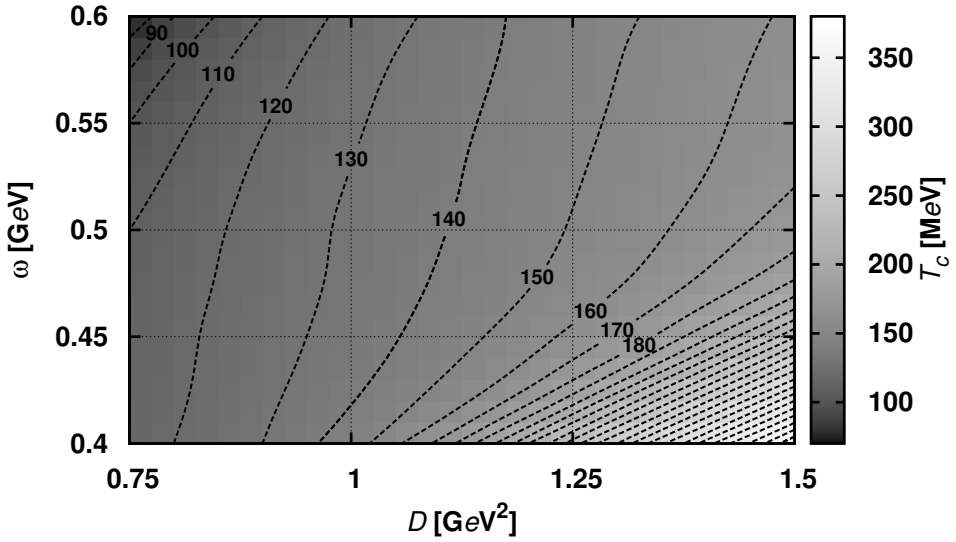

Figure I.1: The critical temperature T_c of the chiral symmetry restoration in dependency on the model parameters D and ω. Dashed lines represent isotherms, all separated by 10 MeV; the labels are given in [MeV].

[1] In gnuplot 4.6, the *contour* command was used with the parameters *points* = 3 and *order* = 10. Afterwards, the contour lines were plotted using the *smooth bezier* option.

Bibliography

[Abr64] M. Abramowitz and I. Stegun: *Handbook of Mathematical Functions*, Applied mathematics series, Dover Publications, 1964.

[Alk01] R. Alkofer and L. von Smekal: *The infrared behaviour of QCD Green's functions: Confinement, dynamical symmetry breaking, and hadrons as relativistic bound states*, Phys. Rep. **353**, 281 (2001).

[Alk02] R. Alkofer, P. Watson and H. Weigel: *Mesons in a Poincaré covariant Bethe-Salpeter approach*, Phys. Rev. D **65**, 094026 (2002).

[Alk04] R. Alkofer, W. Detmold, C. S. Fischer and P. Maris: *Analytic properties of the Landau gauge gluon and quark propagators*, Phys. Rev. D **70**, 014014 (2004).

[Baz12] A. Bazavov et al.: *Chiral and deconfinement aspects of the QCD transition*, Phys. Rev. D **85**, 054503 (2012).

[Bel00] M. Bellac: *Thermal Field Theory*, Cambridge Monographs on Mathematical Physics, Cambridge University Press, 2000.

[Ben96] A. Bender, D. Blaschke, Y. Kalinovsky and C. D. Roberts: *Continuum Study of Deconfinement at Finite Temperature*, Phys. Rev. Lett. **77**, 3724 (1996).

[Ber12] J. Beringer et al.: *Review of Particle Physics*, Phys. Rev. D **86**, 010001 (2012).

[Bil08] E. Bilgici, F. Bruckmann, C. Gattringer and C. Hagen: *Dual quark condensate and dressed Polyakov loops*, Phys. Rev. D **77**, 094007 (2008).

[Bla07] D. Blaschke, D. Horvatic, D. Klabucar and A. Radzhabov: *Separable Dyson-Schwinger model at zero and finite T* (2007), arXiv:0703188 [hep-ph].

[Bla10] M. Blank and A. Krassnigg: *QCD chiral transition temperature in a Dyson-Schwinger-equation context*, Phys. Rev. D **82**, 034006 (2010).

[Blo69] E. D. Bloom et al.: *High-Energy Inelastic $e-p$ Scattering at* 6° *and* 10°, Phys. Rev. Lett. **23**, 930 (1969).

[Bro89] N. Brown and M. R. Pennington: *Studies of confinement: How the gluon propagates*, Phys. Rev. D **39**, 2723 (1989).

[Bro99] I. N. Bronstein, K. A. Semendjajew, G. Musiol and H. Muehlig: *Taschenbuch der Mathematik*, Thun, Frankfurt am Main: Verlag Harri Deutsch, 1999, 4 edition.

[Bur98] C. J. Burden: *Analytic structure of heavy quark propagators*, Phys. Rev. D **57**, 276 (1998).

[Cha07] L. Chang, H. Chen, B. Wang, W. Yuan and Y. xin Liu: *Chemical potential dependence of chiral quark condensate in Dyson–Schwinger equation approach of QCD*, Physics Letters B **644**, 315 (2007).

[Che08] M. Cheng et al.: *QCD equation of state with almost physical quark masses*, Phys. Rev. D **77**, 014511 (2008).

[Cuc07] A. Cucchieri, A. Maas and T. Mendes: *Infrared properties of propagators in Landau-gauge pure Yang-Mills theory at finite temperature*, Phys. Rev. D **75**, 076003 (2007).

[Das06] A. Das: *Field Theory: A Path Integral Approach*, World Scientific Lecture Notes in Physics, World Scientific, 2006.

[Fis05] C. S. Fischer, P. Watson and W. Cassing: *Probing unquenching effects in the gluon polarization in light mesons*, Phys. Rev. D **72**, 094025 (2005).

[Fis09a] C. S. Fischer: *Deconfinement Phase Transition and the Quark Condensate*, Phys. Rev. Lett. **103**, 052003 (2009).

[Fis09b] C. S. Fischer and J. A. Mueller: *Chiral and deconfinement transition from Dyson-Schwinger equations*, Phys. Rev. D **80**, 074029 (2009).

[Fis13] C. S. Fischer and J. Luecker: *Propagators and phase structure of and QCD*, Phys. Lett. B **718**, 1036 (2013).

[Fra96] M. R. Frank and C. D. Roberts: *Model gluon propagator and pion and ρ-meson observables*, Phys. Rev. C **53**, 390 (1996).

[Gau11] W. Gautschi: *Numerical Analysis*, Birkhäuser Boston, 2011.

[GM68] M. Gell-Mann, R. Oakes and B. Renner: *Behavior of current divergences under SU(3) × SU(3)*, Phys.Rev. **175**, 2195 (1968).

[Gon00] S. Gong: *Concise Complex Analysis*, World Scientific, 2000.

[Gri08] D. Griffiths: *Introduction to Elementary Particles*, Physics Textbook, Wiley, 2008.

[Hil12] T. Hilger: *Medium Modifications of Mesons Chiral Symmetry Restoration in-medium QCD Sum Rules for D and rho Mesons, and Bethe-Salpeter Equations*, Ph.D. thesis, TU Dresden (2012).

[Hop13] M. Hopfer, A. Windisch and R. Alkofer: *The Quark-Gluon Vertex in Landau gauge QCD*, PoS **CONFINEMENTX**, 073 (2013).

[Itz05] C. Itzykson and J. Zuber: *Quantum Field Theory*, Dover Books on Physics, Dover Publications, 2005.

[Kap06] J. Kapusta and C. Gale: *Finite-Temperature Field Theory: Principles and Applications*, Cambridge monographs on mechanics and applied mathematics, Cambridge University Press, 2006.

[Kar07] F. Karsch and M. Kitazawa: *Spectral properties of quarks above in quenched lattice QCD*, Phys. Lett. B **658**, 45 (2007).

[Kar09] F. Karsch and M. Kitazawa: *Quark propagator at finite temperature and finite momentum in quenched lattice QCD*, Phys. Rev. D **80**, 056001 (2009).

[Mar92] P. Maris and H. Holties: *Dermination of the singularities of the Dyson-Schwinger equation for the quark propagator*, Int. J. Mod. Phys. A **07**, 5369 (1992).

[Mar97] P. Maris and C. D. Roberts: *π- and K-meson Bethe-Salpeter amplitudes*, Phys. Rev. C **56**, 3369 (1997).

[Mar98] P. Maris, C. D. Roberts and P. C. Tandy: *Pion mass and decay constant*, Phys. Lett. B **420**, 267 (1998).

[Mar99] P. Maris and P. C. Tandy: *Bethe-Salpeter study of vector meson masses and decay constants*, Phys. Rev. C **60**, 055214 (1999).

[McL81] L. D. McLerran and B. Svetitsky: *Quark liberation at high temperature: A Monte Carlo study of SU(2) gauge theory*, Phys. Rev. D **24**, 450 (1981).

[Mo10] Y. Mo, S.-x. Qin and Y.-x. Liu: *Temperature dependence of the effective bag constant and the radius of a nucleon in the global color symmetry model of QCD*, Phys. Rev. C **82**, 025206 (2010).

[Mue10] J. Mueller, C. Fischer and D. Nickel: *Quark spectral properties above T_c from Dyson–Schwinger equations*, The European Physical Journal C **70**, 1037 (2010).

[Mül11] J. A. Müller: *A Dyson-Schwinger Approach to Finite Temperature QCD*, Ph.D. thesis, TU Darmstadt (2011).

[Mun83] H. J. Munczek and A. M. Nemirovsky: *Ground-state $q\bar{q}$ mass spectrum in quantum chromodynamics*, Phys. Rev. D **28**, 181 (1983).

[Mus03] M. Mustafa and M. Thoma: *Can van Hove singularities be observed in relativistic heavy-ion collisions?*, Pramana **60**, 711 (2003).

[Pas79] G. Passarino and M. Veltman: *One-loop corrections for e+e- annihilation into mu+mu- in the Weinberg model*, Nucl. Phys. B **160**, 151 (1979).

[Pes95] M. Peskin and D. Schroeder: *An Introduction To Quantum Field Theory*, Addison-Wesley Publishing Company, 1995.

[Pre92] W. Press, B. Flannery, S. Teukolsky and W. Vetterling: *Numerical Recipes in FORTRAN 77: Volume 1*, Cambridge University Press, 1992.

[Rob90] C. D. Roberts and B. H. J. McKellar: *Critical coupling for dynamical chiral-symmetry breaking*, Phys. Rev. D **41**, 672 (1990).

[Rob94] C. D. Roberts and A. G. Williams: *Dyson-Schwinger equations and their application to hadronic physics*, Progr. Part. Nucl. Phys. **33**, 477 (1994).

[Rob00] C. Roberts and S. Schmidt: *Dyson-Schwinger equations: Density, temperature and continuum strong QCD*, Progr. Part. Nucl. Phys. **45, Supplement 1**, S1 (2000).

[Rob12] C. D. Roberts: *Strong QCD and Dyson-Schwinger Equations* (2012), arXiv:1203.5341 [nucl-th].

[Sou10] N. Souchlas: *A dressed quark propagator representation in the Bethe–Salpeter description of mesons*, J. Phys. G: Nuclear and Particle Physics **37**, 115001 (2010).

[Sta92] S. J. Stainsby and R. T. Cahill: *The analytic structure of quark propagators*, Int. J. Mod. Phys. A **07**, 7541 (1992).

[Sto80] J. Stoer and R. Bulirsch: *Introduction to numerical analysis*, Springer-Verlag, 1980.

[Web04] H. Weber and G. Arfken: *Essential Mathematical Methods for Physicists*, Academic Press, 2004.

[Wei12] W. Weise: *Nuclear chiral dynamics and phases of QCD*, Progr. Part. Nucl. Phys. **67**, 299 (2012).

[Wil07] R. Williams: *Schwinger-Dyson equations in QED and QCD the calculation of fermion-antifermion condensates*, Ph.D. thesis, Durham University (2007).

[Yag05] K. Yagi, T. Hatsuda and Y. Miake: *Quark-Gluon Plasma*, Cambridge Monographs on Particle Physics, Nuclear Physics and Cosmology Series, Cambridge University Press, 2005.

[Ynd07] F. Ynduráin: *The Theory of Quark and Gluon Interactions*, Theoretical and Mathematical Physics, Springer, 2007.

[ZJ93] J. Zinn-Justin: *Quantum field theory and critical phenomena*, International series of monographs on physics, Clarendon Press, 1993.

Erklärung

Hiermit versichere ich, dass ich die vorliegende Arbeit ohne unzulässige Hilfe Dritter und ohne Benutzung anderer als der angegebenen Hilfsmittel angefertigt habe. Die aus fremden Quellen direkt oder indirekt übernommenen Gedanken sind als solche kenntlich gemacht. Die Arbeit wurde bisher weder im Inland noch im Ausland in gleicher oder ähnlicher Form einer anderen Prüfungsbehörde vorgelegt.

Marco Viebach
Dresden, den 25. April 2013

Danksagung

Bedanken möchte ich mich bei Prof. Dr. R. Schmidt für die Aufnahme in das Institut für Theoretische Physik der TU Dresden sowie bei Prof. Dr. T. B. Cowan für die Aufnahme in das Institut für Strahlenphysik des Helmholtz-Zentrums Dresden-Rossendorf, wodurch ich Zugang zu hervorragenden Arbeitsbedingungen erhielt.

Besonders bedanken möchte ich mich bei Prof. Dr. B. Kämpfer für die Möglichkeit zu dieser interessanten Arbeit und die vielen hilfreichen Hinweise und Fragen im Rahmen der Betreuung. Außerdem bedanke ich mich für die Vermittlung eines Gastaufenthalts am Bogoljubov-Institut und die Möglichkeit, einen Vortrag auf der DPG-Frühjahrstagung 2013 zu halten. Während der gesamten Zeit konnte ich sehr viel lernen und sehr viele Erfahrungen sammeln.

Dazu trug das wunderbare Arbeitsklima in unserer Gruppe in entscheidendem Maße bei. Dank gilt allen Kollegen, insbesondere aber Dr. Thomas Hilger für fortlaufende Diskussion der Thematik und Interesse an meiner Arbeit und Falk Wunderlich für unzählige Besprechungen und die kritische Durchsicht meines Manuskripts.

Sergey Dorkin danke ich vielmals für die herzliche Aufnahme am Bogoljubov-Institut sowie für die Einführung in die Thematik und Betreuung während meines Gastaufenthalts.

Für die Durchführung der Zweitkorrektur der vorliegenden Diplomarbeit danke ich sehr Prof. Dr. D. Stöckinger.

Meinen Freunden danke ich für jegliche Interaktion in den letzten Jahren, besonders Aurimas, Julius, Stefan und Tim, die beim Physikstudium an meiner Seite standen.

Ich möchte mich bei meinen Eltern für die jahrelange moralische und finanzielle Unterstützung und außerdem für den Respekt und das Vertrauen gegenüber meinem Tun bedanken.

Meiner Frau, Franziska, danke ich für den moralischen Beistand und den steten Rückhalt, besonders während der Diplomarbeit.